

UC Berkeley

UC Berkeley Electronic Theses and Dissertations

Title

Circuit-QED and Quantum Feedback Control

Permalink

<https://escholarship.org/uc/item/2bm1q8xb>

Author

Li, Hanhan

Publication Date

2014

Peer reviewed|Thesis/dissertation

Circuit-QED and Quantum Feedback Control

by

Hanhan Li

A dissertation submitted in partial satisfaction of the

requirements for the degree of

Doctor of Philosophy

in

Physics

in the

Graduate Division

of the

University of California, Berkeley

Committee in charge:

Professor Birgitta Whaley, Co-chair
Associate Professor Irfan Siddiqi, Co-chair
Assistant Professor Hartmut Haefner
Professor Eli Yablonovitch

Fall 2014

Circuit-QED and Quantum Feedback Control

Copyright 2014
by
Hanhan Li

Abstract

Circuit-QED and Quantum Feedback Control

by

Hanhan Li

Doctor of Philosophy in Physics

University of California, Berkeley

Professor Birgitta Whaley, Co-chair

Associate Professor Irfan Siddiqi, Co-chair

Quantum computation and quantum information are an emerging research field that involves both physics, computer science, and engineering. The quantum nature of our world can be harnessed to dramatically improve the way we store, transmit, and process information. The first part (Chap. 1) of this thesis presents the theory behind quantum information science and gives a survey of some fascinating topics in this area. The second part (Chap. 2 and 3) studies dissipative quantum systems, which helps us understand the challenges facing all real quantum information processors. The third part (Chap. 4 and 5) discusses how we may use control strategies to fight dissipation and protect quantum information. The last part (Chap. 6 and 7) of this thesis describes circuit-QED systems, a solid state implementation of quantum computers that has become increasingly popular over the years due to great controllability and scalability. Most of my independent contributions are contained in Chap. 3, 4, 5, and Sec. 6.3.1, 7.3.

I dedicate this dissertation to my parents for nursing me with affections and love and their dedicated partnership for success in my life.

Contents

Contents	ii
List of Figures	iv
List of Tables	ix
1 Introduction	1
1.1 Prologue	1
1.2 Density Operators	1
1.3 Quantum Operations	5
1.4 Quantum Algorithms	9
1.5 Quantum Cryptography	15
2 Open Quantum Systems	27
2.1 Introduction	27
2.2 The Lindblad Master Equation	27
2.3 Open Quantum Systems and Born-Markov Approximation	28
2.4 Weak Measurements	31
2.5 Photodetection and Homodyne Detection	35
3 Hierarchical Equations of Motion	39
3.1 Formalism	39
3.2 Qubit Relaxation	43
3.3 Unravelling HEOs	47
4 PI Control	51
4.1 Formalism	51
4.2 Two-qubit Entanglement Generation	54
4.3 Harmonic Oscillator State Stabilization	57
5 Optimal Control Protocol Analysis: an Example with Qubit Purification	67
5.1 Introduction	67
5.2 Dynamics	69

5.3	The Locally Optimal Strategy	71
5.4	Global Optimality for the max purity goal	76
5.5	Global optimality for the min time goal	81
5.6	Conclusions	83
5.A	The Verification Theorem	85
5.B	The Coefficient of the u^2 Term	86
5.C	Explicit Solution of Eq. (5.11)	87
6	Circuit QED	89
6.1	Measurement and Control in Circuit-QED	90
6.2	Superconducting Qubits	96
6.3	Quantum Dot Qubits	102
7	A Prototype Circuit QED with Double Quantum Dot	106
7.1	Introduction	106
7.2	Device Layout and Fabrication Process	107
7.3	Numerical Simulations	111
7.4	Experimental Characterization	112
7.5	Summary	114
8	Conclusions	118
	Bibliography	120

List of Figures

1.1	The Bloch sphere	2
1.2	Circuit representations of the CNOT gate (controlled by one qubit) and a general unitary gate (controlled by two qubits).	11
1.3	Geometric visualization of Grover's iteration [3].	13
1.4	A circuit implementing the quantum Fourier transform [3]. The input bits are laid out with the most significant one on the top and output bits with the most significant one on the bottom.	14
1.5	Schematic representation of entanglement purification protocols	19
1.6	Poincare sphere representation of BB84 state in the event of a symmetric attack [36].	20
1.7	Eve's and Bob's information vs the QBER for individual attack against BB84 protocol [36].	21
2.1	A scheme for simple homodyne detection. A low-reflectivity beam-splitter (LRBS) transmits almost all of the system output, and adds only a small amount of the local oscillator through reflection. Nevertheless, the local oscillator is so strong that this reflected field dominates the intensity at the single photoreceiver. This is a detector that does not resolve single photons but rather produces a photocurrent proportional to $J(t)$ plus a constant [130].	36
3.1	This figure compares the relaxation process of a qubit predicted by the Lindblad master equation (Eq. 3.29) and the 2nd order HEOm (Eq. 3.26). $x = y = 0$ is satisfied throughout the process, and only the evolution of z is shown. $\omega_0 = 95$, $\Omega = 100$, $\lambda = 10$, and two different values of bath correlation rate γ are chosen.	45
3.2	This figures shows the relaxation process of the qubit subject to different control protocols. For 'Off resonance' protocol, there is no control Hamiltonian added. For 'On resonance' protocol, $H_c = 5\sigma_z$ is on all the way through. For 'On+Off' resonance protocol, H_c is on until $t \approx 0.6$. Parameters chosen are $\omega_0 = 90$, $\Omega = 100$, $\lambda = 10$, $\gamma = 2$	46

- 3.3 The Bloch vector components X , Y , Z (in the rotating frame defined by ω_0) associated with (a) one typical unravelling (b) the HEoM, Eq. 3.32 with $V = \sigma_z$, solution (labeled with ‘Solution’) vs. stochastic trajectory average (labeled with ‘STA’) of the unravellings. The average is done with 20000 simulation runs. Parameters chosen are $T = 40$, $\lambda = 1$, $\gamma = 10$. (ω_0 is irrelevant here.) 50
- 4.1 The average evolution of a two-qubit system under feedback control. (a) shows the proportional feedback with $\tau_P = 0$ and $f_P = 0.2$ calculated according to the unconditional Wiseman-Milburn equation; (b) shows the proportional feedback with $\tau_P = 1.5$ and $f_P = 0.2$ calculated by averaging over trajectories simulated with Eq. 4.8; (c) shows the integral feedback with $\tau_I = 3$ and $f_I = 0.2$ calculated by averaging over trajectories simulated with Eq. 4.9. $\eta = 0.4$ is chosen for both. The initial state is taken to be the unentangled state T_1 56
- 4.2 The steady state concurrence vs. integration time for the integral control. The relation is plotted with $\eta = 0.4$ and three different f_I values. 57
- 4.3 The evolution of X and P quadratures in the rotating frame of an oscillator subject to an x and p control Hamiltonian. The parameters of the oscillator are as follows: $m = 1$, $\omega = 1$, $\eta = 0.1$, $k = 0.02$, $\gamma = 0$. The initial state is set to $X_g = 10$, $P_g/(m\omega) = 10$ and the target state is set to $X_g = 6$, $P_g/(m\omega) = 4$. For the integral control, the characteristic time τ_I for the exponential filter is set to $0.04T$. The chosen feedback strengths are very optimal. 60
- 4.4 The evolution of X and P quadratures in the rotating frame of an oscillator subject to an x feedback Hamiltonian. The plots show typical simulation trajectories of Eq. 4.31, the dynamics the under rotating wave approximation. The parameters of the oscillator are as follows: $\eta = 0.4$, $k = 0.01$, $\gamma = 0$. Feedback strengths are $u_X = u_P = -2\sqrt{m\omega\eta k/\hbar}V_x$. The initial state is set to $X_g = 10$, $P_g/(m\omega) = 10$ and the target state is set to $X_g = 6$, $P_g/(m\omega) = 4$. For the proportional control, $\tau_P = 0$, and for the integral control, $\tau_I = 4T$ 63
- 4.5 This plot shows the long time control error, e , vs. the integration time, τ_I . $\tau_I = 0$ means proportional control without delay. The parameters of the oscillator are as follows: $\eta = 0.4$, $k = 0.01$, $\gamma = 0$. Feedback strengths are $u_X = u_P = -2\sqrt{m\omega\eta k/\hbar}V_x$. e is calculated by averaging over 20000 runs. 64
- 4.6 The evolution of X and P quadratures in the rotating frame of an oscillator subject to an x feedback Hamiltonian without invoking the rotating wave approximation. The parameters of the oscillator are as follows: $m = 1$, $\omega = 1$, $\eta = 0.4$, $k = 0.01$, $\gamma = 0$. The initial state is set to $X_g = 10$, $P_g/(m\omega) = 10$ and the target state is set to $X_g = 6$, $P_g/(m\omega) = 4$. For the physically proportional control, $\tau_P = T/4$, and for the integral control, $\tau_I' = T/2$. The chosen feedback strengths are very optimal for both. 65

4.7	This plot shows the long time control error, e , vs. the measurement efficiency, η , for both the physically proportional feedback and the integral feedback without invoking the rotating wave approximation. The parameters of the oscillator are as follows: $m = 1$, $\omega = 1$, $k = 0.02$, $\gamma = 0$ and the target state is set to $X_g = 6$, $P_g/(m\omega) = 4$. For the physically proportional control, $\tau_P = T/4$, and for the integral control, $\tau_I = T/2$. The error e is calculated by averaging over 20000 runs.	66
5.1	Average rate of change of purity as a function of instantaneous purity in the presence of measurement inefficiency, for the diagonal measurement protocol ($ u(r, t) = 1$) and the unbiased measurement protocol ($u(r, t) = 0$). The point where the locally optimal strategy switched between these protocols is indicated as P^* . Parameters used for this plot are $k = 1$, $\eta = 0.8$, and $\gamma_1 = \gamma_\phi = 0$.	74
5.2	Average purity vs. time in the case of no decoherence for the unbiased measurement protocol, the locally optimal strategy, and the diagonal measurement protocol for two different initial purities. The parameters used here are $k = 1$, $\eta = 0.84$ ($r^* = 0.9$), and $\gamma_1 = \gamma_\phi = 0$.	79
5.3	Behavior of the solution to the Fokker-Planck equation, Eqn. (5.9) at three different times t , visualized by the distribution of $s(t) = \text{arctanh}(r(t))$ as the qubit evolves under the locally optimal and the diagonal measurement protocols. Both protocols operate on a qubit initially at the same purity, with $r_0 = 0.95$. Parameters used are the same as in Fig. 5.2, namely $k = 1$, $\eta = 0.84$ ($r^* = 0.9$), and $\gamma_1 = \gamma_\phi = 0$.	80
5.4	Performance comparison of the free evolution, the locally optimal strategy, the no-feedback diagonal measurement, the unbiased measurement, and the negative diagonal measurement protocols in the presence of decoherence for initial condition $\rho_0 = \mathbf{I}/2$ ($r_0 = 0$). The chosen parameters are $k = 1$, $\eta = 0.91$, $\gamma_1 = 0.2$, $\gamma_2 = 0.3$. 5.4a plots the locally optimal strategy for this chosen set of parameters. Notice the switch from the preferred negative diagonal measurement control at small and large r values ($u_{lo}(r, t) = -1$) to a more complex preferred control ($u_{lo}(r, t) > -1$) for intermediate values of r . 5.4b shows the average purity (over 40,000 runs) vs. time and 5.4c shows the average purification time (over 20,000 runs) as a function of the target Bloch vector length for the five protocols. The statistical variation in the simulations is comparable to the line-width of the plots, so error bars are not explicitly shown.	82
6.1	Schematics of a circuit QED setup with a quarter wave length transmission line resonator. The right end of the resonator, where measurement and control pulses are sent in and reflected, is coupled to a quantum dot. The left end of the resonator is terminated with a large capacitor which is effectively a short circuit under AC. (Courtesy of Thorsten Last.)	91
6.2	Lumped LC model of a resonator coupled to an atom near a high impedance resonance.	92

6.3	Energy spectrum of the Jaynes-Cummings Hamiltonian in (a) zero detuning and (b) large detuning [6].	94
6.4	State dependent reflected phase of a resonator measurement pulse vs. its angular frequency ($\omega_d - \omega_r$) in the qubit ground (blue) and excited (red) states, as well as the bare resonator spectrum (dashed) [102].	95
6.5	Circuit diagram for a charge qubit.	97
6.6	(a) Circuit diagram and (b) washboard potential for a phase qubit [136].	99
6.7	(a) Circuit diagram and (b) double well potential for a flux qubit [136].	100
6.8	Eigenenergies E_m (first three levels, $m=0,1,2$) of the qubit Hamiltonian Eq. 6.26 as a function of the effective offset charge n_g for different ratios E_J/E_C [61].	101
6.9	A double well potential and its lowest energy states.	103
6.10	Top and cross-sectional views of a lateral quantum dot device consisting of four metallic gates (yellow, labeled L, P, R and T) and two ferromagnetic strips (blue) patterned at the surface of a semiconductor heterostructure developed at Tarucha's group. The thick arrows indicate the direction of the external magnetic field B_0 and magnetization M . The origin is fixed to the quantum dot position. [88]	104
7.1	(color online) Large scale view of the device. The electron confinement gates are located within the red solid box and are not visible on this scale. The 'X' within this box are the two accumulation gates creating the 2DEG. Inside the short dashed blue box lies the CPS resonator and the coupling capacitors for the microwave wire bond feed. Within the long dashed green box lies the ~ 50 pF shorting capacitor that is the bias tee combining the DC P_L and P_R bias voltage with the microwave carrier.	108
7.2	(color online) (a) SEM of the electron confinement gates and the 2DEG accumulation gates, which are false colored red. The plunger gates P_R and P_L are false colored blue, and emphasize the spatial decoupling of the microwave resonator from the 2DEG. The inset SEM details the electron confinement gates. (b) A schematic cross section of the MOS accumulation structure in this device. (not to scale)	109
7.3	(color online) Numerical simulations (see text for details) (a) 2DEG induced at the Si-SiO ₂ interface (b) Interface electrostatic potential. (c) Applied gate bias voltages setting boundary conditions. (d) Ground state wave function envelope for the region in the black dashed box in (b). (e) First excited state wave function envelope.	110
7.4	(color online) Transport characterization of electron confinement. (a) Current resonances as function of plunger gate bias forming honeycomb charge stability regions. (b) QPC conductance as a function of left plunger gate bias showing single electron charging events (arrows). (c) Inconsistent honeycombs over large plunger gate bias ranges.	112

7.5	(color online) Microwave resonator reflection coefficient data (a) Magnitude, including overall gain of the measurement chain. (b) Phase (c) Real part, with time delay adjusted to adjust reference to input plane of resonator. The fit is to a Lorentzian. (d) Power dependence of the internal quality factor, characterizing resonator internal losses.	116
7.6	(color online) Schematic representation for the failure to achieve consistent long range honey combs with sweeps of plunger gate bias. (a) Cartoon of the double quantum dot honeycomb current peaks as a function of gate bias. (b) Cartoon of the sub two- dimensional conductance in the region marked by arrows in (d), giving regions of allowed conductance, marked in yellow, surrounded by regions of forbidden conductance. (c) Cartoon of what transport measurements of (a) and (b) in series would look like. (d) The region of the accumulation gate marked with the yellow arrows is where the 2DEG becomes sub two-dimensional. . . .	117

List of Tables

1.1	Security bounds of QBER on the BB84 and the six-state protocols	26
5.1	The strategy that maximizes the instantaneous rate of increase of average purity (the locally optimal strategy) when $\gamma_1 = \gamma_\phi = 0$. $r^* = \sqrt{2 - 1/\eta}$ is the critical Bloch vector length at which there is a discontinuous change in protocols when $1/2 < \eta < 1$	73

Acknowledgments

The past five years as a PhD student in physics department at UC Berkeley has been a very intellectually stimulating experience for me. The work of this thesis is done over the past four years in Berkeley Quantum information and Computation Center under the guidance of Prof. Birgitta Whaley. I am very grateful to her as she sponsored me and gave me numerous insightful advice and comments all the way through. In addition, she was always able to point me to the most relevant literature and recommend the most appropriate researchers to discuss with. I would also like to thank Prof. Irfan Siddiqi, Prof. Hartmut Haefner, Prof. Eli Yablonovitch, Prof. Steve Louie at UC Berkeley for their guidance as well.

I would like to thank Prof. Whaley's entire group member for this rewarding PhD experience. I am especially grateful to two Former postdocs here, Mohan Sarovar and Alireza Shabani as they patiently taught me a lot of background knowledge when I was stepping into the field of quantum information and provided me many useful suggestions during my research. Felix Motzoi and Jan Roden in our group also deserves my especial thanks.

2011 International Workshop On Silicon Quantum Electronics, 2012 NASA Quantum Future Technologies Conference, and 2013 Control of Complex Quantum Systems Workshop at KITP (sponsored by NSF) inspired many of my ideas. I would like to thank the organizers as well as Prof. Hong-Wen Jiang, Matthew House, Joshua Combs, and Prof. Howard Wiseman whom I met during the conferences.

Chapter 1

Introduction

1.1 Prologue

Quantum information science studies how quantum mechanical effects influences computer science and information theory. The birth of this field dates back to the 1980s when pioneers like Manin [70] and Feynman [28] realized that a quantum computer allows us to perform certain simulations much more efficiently than a classical one, and that its reversibility naturally avoids the heat dissipation problem. Quantum information science took an explosive growth afterward, characterized by the milestone events such as Charles Bennett and Gilles Brassard's secure cryptographic key distribution protocol in 1984 [5], Peter Shor's factoring algorithm in 1994 [106], Lov Grover's database search algorithm in 1996, the Loss-DiVincenzo quantum computer proposal in 1997 [67]. It is nowadays a major research field that encompasses quantum computing, quantum complexity theory, quantum communication, quantum communication complexity, quantum error correction, entanglement information, superdense coding, teleportation, etc.

In this chapter, we will walk through some preliminary concepts about density operators and quantum operations. We will then take a glimpse of two fascinating subjects in the field, quantum algorithms and quantum cryptography.

1.2 Density Operators

The state of a quantum system can be represented by a vector in a Hilbert space if we have complete information about it. Such a state is called a pure state. In practice, we often know a collection of states $\{|\psi_k\rangle\}$ the system might be in, and the probability p_k associated with each one of them. Obviously $\sum_k p_k = 1$. States like this which we lack perfect knowledge about are called mixed states. The mathematical quantity we use to represent a mixed state is the following density operator:

$$\rho = \sum_k p_k |\psi_k\rangle \langle \psi_k|. \quad (1.1)$$

For a given basis, we can write down the density operator as a density matrix. It's easy to see that a density operator is Hermitian, positive semi-definite, and has unit trace. The unit trace property follows directly from probabilities adding up to one.

The Density Operator for a Qubit

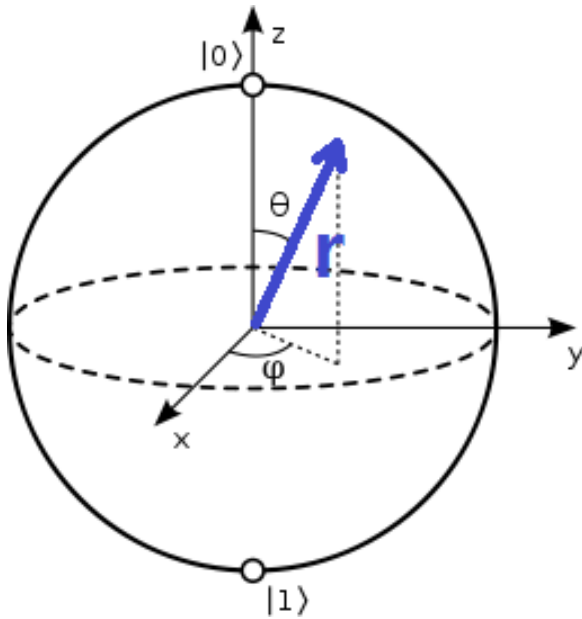


Figure 1.1: The Bloch sphere

The density matrix for a qubit can be expressed as

$$\rho = \frac{1}{2}(I + x\sigma_x + y\sigma_y + z\sigma_z), \quad (1.2)$$

with the real coefficients x , y , and z satisfying $x^2 + y^2 + z^2 \leq 1$. It turns out x , y , and z are the expectation values of the corresponding Pauli operators. For example, $x = \langle \sigma_x \rangle$. One can geometrically represent a qubit state by a point with coordinates (x, y, z) in 3D, and it is located within a unit sphere called the Bloch sphere as shown on the left. Also, when you mix two states with some weights, you just need to take the arithmetic average of the representing points with these weights to compute the resulting state. The Bloch vector (the vector from the origin to the representing point) has a nice property: it transforms just like an ordinary vector under $SO(3)$ rotations! One can check that pure states reside on the surface of the sphere and mixed states reside inside the sphere. A pure state labeled by θ and ϕ in the spherical coordinates corresponds to the state

$$|\psi\rangle = \cos\left(\frac{\theta}{2}\right) |0\rangle + \exp(i\phi) \sin\left(\frac{\theta}{2}\right) |1\rangle. \quad (1.3)$$

It might sound a bit strange that we use the density operator instead of $\{p_k\}$ and $\{|\psi_k\rangle\}$ to describe a mixed state. Indeed, different statistical mixtures of pure states may correspond to the same density operator. For a spin- $\frac{1}{2}$ system, equal mixture of the two σ_z eigenstates and

equal mixture of the two σ_x eigenstates both give rise to the density operator $\frac{1}{2}I$. Therefore, it seems that we throw away some information about the system by inventing the density operator, but we will soon see that what we throw away is exactly the irrelevant information. Let us first follow the line of logic in Ref. [3] and derive some properties of density operators.

How does the density operator change when we evolve the system from time t_i to t_f ? Let the unitary time evolution operator be U , then

$$\begin{aligned}\rho(t_f) &= \sum_i p_k |\psi_k(t_f)\rangle \langle \psi_k(t_f)| \\ &= \sum_i p_k U |\psi_k(t_i)\rangle \langle \psi_k(t_i)| U^\dagger \\ &= U \left(\sum_i p_k |\psi_k(t_i)\rangle \langle \psi_k(t_i)| \right) U^\dagger \\ &= U \rho(t_i) U^\dagger.\end{aligned}\tag{1.4}$$

Next, how does the density operator change when we make a quantum measurement? let $\{V_i\}$ be the eigenspaces of a measurement operator O , and P_i be the projection operation onto V_i . (The projections obey the rules $P_i = P_i^\dagger$, $P_i P_j = \delta_{ij} P_i$, and $\sum_i P_i = 1$.) The probability of getting measurement result i , i.e. collapsing into the space V_i , is given by:

$$\begin{aligned}p(i) &= \sum_k p_k \langle \psi_k | P_i | \psi_k \rangle \\ &= \sum_k p_k \langle \psi_k | P_i \sum_j |j\rangle \langle j| \psi_k \rangle \\ &= \sum_j \langle j | \sum_k p_k |\psi_k\rangle \langle \psi_k | P_i | j \rangle \\ &= \text{Tr}(\rho P_i).\end{aligned}\tag{1.5}$$

Suppose we obtain result i , what would be the density operator immediately after the measurement? We know that if the system is initially in the pure state ψ_k , the post-measurement state would be

$$|\psi'_{k|i}\rangle = \frac{P_i |\psi_k\rangle}{\sqrt{\langle \psi_k | P_i | \psi_k \rangle}}.\tag{1.6}$$

We also need to know the probability of being in such a state to calculate the density operator. The prior probability for the pre-measurement state to be $|\psi_k\rangle$ is p_k , but the proper probability to use is the posterior probability $p(k|i)$ given that the measurement result is i . They are related by the Bayes rule, $p(k|i) = p(i|k)p_k/p(i)$, where $p(i|k) = \langle \psi_k | P_i | \psi_k \rangle$. Therefore, the post-measurement density operator conditioned on result i is:

$$\rho'_i = \sum_k p(k|i) |\psi'_{k|i}\rangle \langle \psi'_{k|i}| = \frac{P_i \rho P_i}{\text{Tr}(\rho P_i)}.\tag{1.7}$$

Also, it's easy to check that the expectation value of the observable O is

$$\langle O \rangle = \text{Tr}(\rho O). \quad (1.8)$$

The above equations are basic quantum mechanical laws written in the density operator picture. Let us then come back to the question raised earlier in this section. Does the density operator fail to capture everything because different statistical mixtures may yield the same density operator? We see from Eq. 1.5 that the measurement statistics depends solely on the density matrix ρ instead of specific ways of mixtures. Also we see from Eq. 1.4 and 1.7 that post-evolution and post-measurement density operators can be written in terms the pre-evolution and pre-measurement density operators. Hence, there is no way to distinguish two mixed states that have the same density operator, no matter what kinds of evolution and measurement we perform. Conversely, it's easy to show that mixed states described by different density operators are distinguishable by performing projective measurements. Therefore, the density operator provides the most precise way to describe a mixed state.

Quantum Smoothing

Does a density operator always suffice to describe the state of a system? Not for quantum smoothing [134]. Consider again two states of the spin- $\frac{1}{2}$ system that have the same density operator $\frac{1}{2}I$: 1. Equal mixture of the two σ_z eigenstates $|0\rangle$ and $|1\rangle$; 2. Equal mixture of the two σ_x eigenstates $|+\rangle$ and $|-\rangle$. ($|\pm\rangle \equiv (|0\rangle \pm |1\rangle)/\sqrt{2}$.) Suppose we make a σ_z measurement and the result comes out to be $+1$. Then we ask the following question: what was the state of the system before the measurement given the measurement outcome? For case 1, we know $|1\rangle$ cannot yield outcome $+1$, so the pre-measurement state should be the pure state $|0\rangle$, $\text{diag}\{1, 0\}$ in the density matrix notation. For case 2, both $|+\rangle$ and $|-\rangle$ will yield outcome $+1$ with the same probability 50%, so the pre-measurement state is still equally likely to be $|+\rangle$ and $|-\rangle$, $\frac{1}{2}I$ in the density matrix notation. Therefore, we get completely different answers for different mixtures that have the same density operator. These kinds of problems where we try to estimate the state in the past are called smoothing problems. A hybrid classical-quantum density operator is needed to properly describe a state [22]. As long as we do not backtracking states conditioned on measurement outcomes, the standard density operator formalism suffices.

Real quantum systems are often composite systems. For example, a cavity-QED setup has an atom and photons as its subsystems. When we consider a composite system of two subsystem 1 and 2, the Hilbert space is the tensor product of the Hilbert spaces associated with each one of them, i.e., $\mathcal{H} = \mathcal{H}_1 \otimes \mathcal{H}_2$. A generic state (which may be entangled) for the bipartite system can be written as:

$$\rho = \sum_{ij} \sum_{i'j'} \rho_{ij;i'j'} |i\rangle_1 |j\rangle_2 {}_1\langle i'| {}_2\langle j'|. \quad (1.9)$$

If we want to focus our study on one subsystem, we can get its state by tracing over the other subsystem. For example, the reduced density operator for the first system is

$$\rho_1 \equiv \text{Tr}_2 \rho, \quad (1.10)$$

where Tr_2 denotes the partial trace:

$$\text{Tr}_2 \rho \equiv \sum_j {}_2 \langle j | \rho | j \rangle_2, \quad (1.11)$$

Let us explore some properties of the partial trace. Suppose the composite system evolves under some separable operator $U_1 \otimes U_2$. If at the end we just care about system 1, we can trace over system 2 at the very beginning and consider system 1 all the way. Mathematically,

$$\text{Tr}_2(U_1 \otimes U_2 \rho U_1^\dagger \otimes U_2^\dagger) = U_1(\text{Tr}_2 \rho) U_1^\dagger. \quad (1.12)$$

Suppose we measure system 1 with some observable O_1 , whose eigenspace projection operators are $\{P_{1i}\}$. For the composite system, the projection operators are $\{P_i\}$, where $P_i = P_{1i} \otimes I_2$. We can again trace over system 2 even before the measurement because the probability of collapsing onto the i th eigenspace is

$$\text{Tr}(\rho P_i) = \text{Tr}((\text{Tr}_2 \rho) P_{1i}), \quad (1.13)$$

and the reduced density operator of system 1 after measurement is

$$\text{Tr}_2 \frac{P_i \rho P_i}{\text{Tr}(\rho P_i)} = \frac{P_{1i}(\text{Tr}_2 \rho) P_{1i}}{\text{Tr}((\text{Tr}_2 \rho) P_{1i})}. \quad (1.14)$$

One can similarly prove that a projective measurement on system 2 does not affect the reduced density operator of system 1 at all.

Therefore, we can isolate a system by tracing over its environment if the system and environment are evolved and measured separately in the future.

1.3 Quantum Operations

In this section, we will develop the formalism of quantum operations, which describe generically the dynamics of a quantum system. We will again follow the presentation of Ref. [4].

First consider the so called system-bath model for a quantum operation. Let us use the subscript 1 to denote the system and 2 to denote the bath. Consider the following initial product state for the system and bath:

$$\rho = \rho_1 \otimes |0\rangle_2 {}_2 \langle 0|. \quad (1.15)$$

We apply some unitary evolution operator U on the composite space and extract the reduced density operator of the system:

$$\rho'_1 = \text{Tr}_2(U \rho U^\dagger) = \sum_j {}_2\langle j|U|0\rangle_2 \rho_1 {}_2\langle 0|U^\dagger|j\rangle_2. \quad (1.16)$$

where $\{|j\rangle_2\}$ is an orthonormal basis set for the bath. If we define the Kraus operators

$$E_j \equiv {}_2\langle j|U|0\rangle_2, \quad (1.17)$$

we can rewrite Eq. 1.16 as

$$\rho'_1 = \sum_j E_j \rho_1 E_j^\dagger. \quad (1.18)$$

It's easy to check that Kraus operators satisfy the following completeness relation:

$$\sum_j E_j^\dagger E_j = I. \quad (1.19)$$

Eq. 1.18 together with Eq. 1.19 defines a linear map $S : \rho_1 \rightarrow \rho'_1$ from linear operators to linear operators, and this map S is called a quantum operation. Eq. 1.18 is known as the Kraus representation of a quantum operation. Please be aware that the same quantum operation can have many different Kraus representations, and for an N dimensional Hilbert space, we can always choose a representation where the number of Kraus operators is less than equal to N^2 .

What we have shown so far is that the system-bath representation naturally produces the Kraus representation. It's not hard to reverse the procedure and show that any quantum operation can be lifted to a unitary operator on a larger space. We first add an auxiliary bath whose dimension matches the number of Kraus operators. A unitary operator U that satisfies the following relation is a desired lift [4].

$$U |\psi\rangle_1 |0\rangle_2 = \sum_j E_j |\psi\rangle_1 |j\rangle_2. \quad (1.20)$$

The completeness relation of $\{E_i\}$ guarantees that U preserves inner products,

$${}_1\langle\psi|{}_2\langle 0|U^\dagger U|\psi\rangle_1|0\rangle_2 = \sum_k {}_1\langle\psi|E_k^\dagger E_k|\psi\rangle_1 = {}_1\langle\psi|\psi\rangle_1, \quad (1.21)$$

and can always be constructed. Therefore, the system-bath representation and the Kraus representation of quantum operations are equivalent.

Now let us have a third definition of a quantum operation, which is more mathematically abstract. A map $S : \rho \rightarrow \rho'$ is a quantum operation if and only if the following four criteria are satisfied:

1. S is linear,

2. S preserves hermiticity,
3. S preserves trace,
4. S is completely positive.

This definition of quantum operations is completely equivalent to the previous two, the proof of which is a bit lengthy and is provided in Ref. [80].

The notion of quantum operations captures a wide range of dynamics like unitary evolution, quantum measurement and stochastic changes. It is particularly useful for describing open quantum systems, as we see from the system-bath model. We can also generalize the concept of a quantum operation to include non-trace-preserving operations where $\text{Tr}(S(\rho)) \leq 1$ is allowed, which can describe processes like post-selection by measurement. However, for the purpose of this thesis, we will stick with the trace-preserving definition of quantum operations.

1.3.1 Generalized measurements

Let us move on and define what is called a generalized measurement. This is described by a set $\{M_i\}$ of measurement operators that satisfy the completeness relation

$$\sum_i M_i^\dagger M_i = I. \quad (1.22)$$

If the pre-measurement state is given by the density operator ρ , then with probability

$$p_i = \text{Tr}(M_i^\dagger M_i \rho) \quad (1.23)$$

the measurement gives outcome i and the post-measurement state becomes

$$\rho'_i = \frac{M_i \rho M_i^\dagger}{\text{Tr}(M_i^\dagger M_i \rho)}. \quad (1.24)$$

Hence, the unconditioned post-measurement state is

$$\rho' = \sum_i M_i \rho M_i^\dagger. \quad (1.25)$$

As its name suggests, a generalized measurement generalizes the concept of a projective measurement, where $\{M_i\}$ are orthogonal projectors. Please be aware if we identify M_i with the Kraus operators, Eq. 1.25 takes exactly the form of a Kraus representation of a quantum operation. Therefore, the overall effect of a generalized measurement is also a quantum operation.

How does a generalized measurement come about? Not surprisingly, we can model an arbitrary generalized measurement on the system by adding an auxiliary bath. As before,

we will consider an initial product state $\rho = \rho_1 \otimes |0\rangle_2 \langle 0|$ and a unitary evolution U on the combined space. U is defined by its following action:

$$U |\psi\rangle_1 |0\rangle = \sum_j M_j |\psi\rangle_1 |j\rangle_2, \quad (1.26)$$

We then make a projective measurement $\{P_i\}$ on the bath in the standard basis, namely $P_i = I_1 \otimes |i\rangle_2 \langle i|$. One can check that the measurement gives outcome i with probability

$$p_i = \text{Tr}(U \rho U^\dagger P_i) = \text{Tr}(M_i^\dagger M_i \rho), \quad (1.27)$$

and the post-measurement state would be

$$\rho'_i = \frac{P_i U \rho U^\dagger P_i}{\text{Tr}(U \rho U^\dagger P_i)} = \frac{M_i \rho M_i^\dagger}{\text{Tr}(M_i^\dagger M_i \rho)}. \quad (1.28)$$

Hence, the generalized measurement on a system naturally arises from a unitary evolution of system and bath followed by a non-degenerate projective measurement on the bath, which is a manifestation of Neumark's theorem discussed in Ref. [84].

1.3.2 POVM's

A positive operator-valued measurement (POVM) we often encounter is very similar to a generalized measurement. It is characterized by a set of positive semi-definite operators $\{F_i\}$ (POVM elements) such that

$$\sum_i F_i = I. \quad (1.29)$$

The above partition of unity with operators is called an operator-valued measure, and hence the name POVM. Measuring the state ρ gives outcome i with probability

$$\text{Tr}(F_i \rho), \quad (1.30)$$

and a POVM does not make any assumption about the post-measurement states. Because $M_i^\dagger M_i$ is automatically positive semi-definite, and a positive semi-definite matrix can always be written as $M_i^\dagger M_i$, the definition of measurement statistics in a POVM is equivalent to that in a generalized measurement, and a generalized measurement is a POVM. The following is an example of dynamics captured by POVM's. A system and bath initially start with a product state, and a generic projective measurement is performed on the combined space. The conditioned post-measurement state cannot be written in a simple form as Eq. 1.24 in general, but the outcome probabilities are given by Eq. 1.30 with appropriately chosen $\{F_i\}$ as in a POVM.

1.4 Quantum Algorithms

Quantum computing is a fascinating application of quantum mechanics in computer science. Because a quantum system can provide a much larger space for states and operations than a classical system can, and a sort of parallelism is intrinsic to quantum superposition, quantum computers are potentially more powerful than a classical computer. In this thesis, we will use exclusively the circuit model of quantum computation. In this model, a collection of two-level systems (called quantum bits or qubits) is served as a quantum register. We apply quantum operations called gates (which are analogous to classical gates like NOT and AND) on them and make measurement to obtain the results. This model is easy to understand and close to experiment implementations. There are other models like one-way quantum computers, adiabatic quantum computers, and topological quantum computers. The above four models are all shown to be equivalent to the more abstract model, the quantum Turing machine.

For a qubit, we always choose some orthonormal basis states $|0\rangle$, $|1\rangle$ to represent value 0 and 1 of a bit. This basis is called computational basis or standard basis. For a n -qubit register, we follow the usual rule of a digital representation of a number (i.e. the most significant digit at the left) and use a single number to denote a basis state. For example, $|4\rangle = |1\rangle|0\rangle|0\rangle$.

To get an idea of the huge power of quantum computers, consider a n -qubit register. The Hilbert space is 2^n dimensional, so a general state will be a superposition of the 2^n basis states as follows:

$$|\psi\rangle = \sum_{i=1}^{2^n} c_i |i\rangle. \quad (1.31)$$

If we apply a unitary gate U on it, output gate would be

$$U|\psi\rangle = \sum_{i=1}^{2^n} c_i U|i\rangle. \quad (1.32)$$

Classically a gate acts on one state at a time, but the quantum gate U seems to act simultaneously on all 2^n basis states, and the results of all of them are encoded in the output state to some extent. This is why there is some intrinsic parallelism at work in a quantum operation. However, extracting useful information out of the output states is extremely difficult. A simple measurement collapses a quantum states, destroys most of the information, and the outcome gives little knowledge about the state. One typically needs to engineer the initial state, the quantum gates, as well as the measurement procedure in order to utilize the power of a quantum operation, which is quantum algorithms all about. The most famous algorithm classes so far are quantum search based algorithms and quantum Fourier transform based algorithms, and we will talk about how these two basic algorithms work.

Before we dive into quantum algorithms, let us walk through some elementary gates we will often encounter in quantum computing. Two useful single qubit gates are the Hadamard

gate and the phase shift gate. The Hadamard gate is defined as

$$H = \frac{1}{\sqrt{2}} \begin{bmatrix} 1 & 1 \\ 1 & -1 \end{bmatrix}. \quad (1.33)$$

This gate transforms the computational basis $\{|0\rangle, |1\rangle\}$ into the so called Hadamard basis $\{|+\rangle, |-\rangle\}$, which correspond to the two poles on the x axis in the Bloch sphere. The phase shift gate is defined as

$$R_z(\delta) = \begin{bmatrix} 1 & 0 \\ 0 & \exp(i\delta) \end{bmatrix}. \quad (1.34)$$

This gate shifts the relative phase of $|1\rangle$ to $|0\rangle$, and it is basically a rotation of angle θ about the z axis.

The controlled-NOT (CNOT) gate is a two-qubit gate that is very important for quantum computation. It is defined by its action on the basis states, i.e. $\text{CNOT}(|x\rangle|y\rangle) = |x\rangle|x \oplus y\rangle$ with $x, y=0, 1$, and \oplus means XOR operation. The gate applies a NOT operation on the second (target) qubit conditioned on the first (control) qubit being 1. The matrix representation of a CNOT gate is

$$\begin{bmatrix} 1 & 0 & 0 & 0 \\ 0 & 1 & 0 & 0 \\ 0 & 0 & 0 & 1 \\ 0 & 0 & 1 & 0 \end{bmatrix}. \quad (1.35)$$

We can similarly define a C -U gate for any unitary operator U . It applies U on the target qubit if the control qubit is 1. For $(k+1)$ -qubit system, we can define a C^k -U gate, which applies U on the target qubit if all the k control qubits are 1. Fig. 1.2 shows how to represent these gates in a circuit diagram.

CNOT gates are very useful for entanglement generation. Moreover, CNOT gates are so powerful that an arbitrary unitary operation on n qubits can be constructed from one-qubit gates and two-qubit CNOT gates. Namely, these gates forms a universal set for quantum computation.

Suppose we have an integer function $f(x): \{0, 1\}^n \rightarrow \{0, 1\}^m$ that we want to evaluate. Classically, we just need to construct a gate with n inputs and m outputs that implement this function. We may not be able to implement f directly in a quantum gate because unitary operations are reversible while f might not be. However, we can always embed a function f into a reversible function $\tilde{f}: \{0, 1\}^{m+n} \rightarrow \{0, 1\}^{m+n}$ as

$$\tilde{f}(x, y) = (x, y \oplus f(x)), \quad (1.36)$$

where x is n -bit, y is m -bit, and \oplus is the bitwise XOR operation. The actually result $f(x)$ is just the last m bits of $\tilde{f}(x, 0)$. This \tilde{f} defines a unitary operator U_f , which is sometimes called the oracle operator.

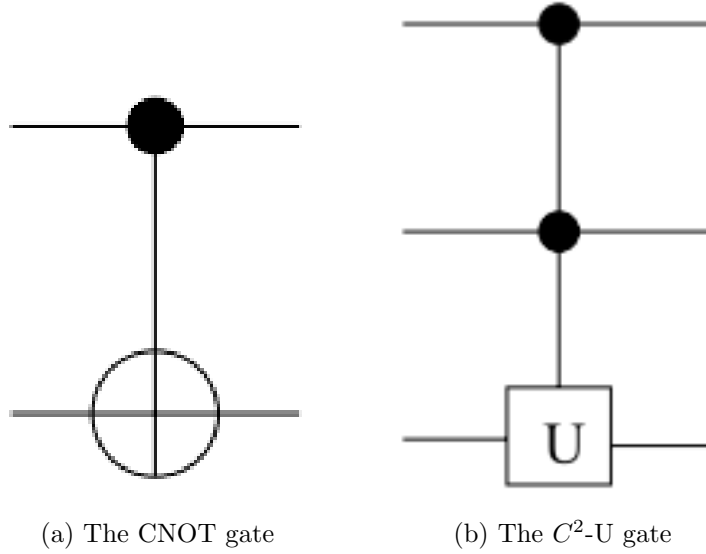


Figure 1.2: Circuit representations of the CNOT gate (controlled by one qubit) and a general unitary gate (controlled by two qubits).

1.4.1 Quantum Search

The unstructured database search problem is concerned with the finding one particular item in an unstructured database. It can be phrased in terms of an ordinary search problem which is important for the study of many computer science problem such as the NP class. The search problem can be described as follows. Suppose we would like to find one marked item x_0 among $\{0, 1, \dots, N-1\}$. We have at our disposal a function $f: \{0, 1\}^n \rightarrow \{0, 1\}$ with $n \geq \log(N)$ which checks if the input is the marked one:

$$f(x) = \begin{cases} 1 & \text{if } x = x_0, \\ 0 & \text{otherwise.} \end{cases} \quad (1.37)$$

The problem is to find x_0 with fewer queries of an oracle operator of f as possible. For a quantum algorithm, this oracle O is usually defined by¹

$$|x\rangle \xrightarrow{O} (-)^{f(x)} |x\rangle. \quad (1.38)$$

A classical algorithm can do no better than an exhaustive search of all the possibilities and the complexity is $O(N)$. However, Grover showed that a quantum algorithm can solve it in $O(\sqrt{N})$ queries and let us see how it works.

Besides the oracle O , let us define the following operator D that can also act on the n qubit system:

$$D = 2|S\rangle\langle S| - I, \quad (1.39)$$

¹It can be constructed from the standard oracle operator, Eq. 1.36 by setting the second register $|y\rangle$ to $|-\rangle$.

where $|S\rangle$ is the equal superposition state:

$$|S\rangle = \frac{1}{\sqrt{2^n}} \sum_{x=0}^{2^n-1} |x\rangle. \quad (1.40)$$

D is sometimes referred to as the inversion about mean operator. Grover's iterator is defined as

$$G = DO. \quad (1.41)$$

The initial state of the n qubits is set to $|S\rangle$, which can be obtained from $|0\rangle$ by applying a Hadamard gate on each qubit. We will repeatedly apply Grover's iterator, and the state is going to reach pretty close to $|x_0\rangle$ at some point. To see why, let us have a geometric representation of Grover's iteration as in Fig. 1.3. The figure plots a (real) 2-D plane spanned by $|x_0\rangle$ and $|S\rangle$. Let $|x_0^\perp\rangle$ denote the state orthogonal to $|x_0\rangle$, and θ be the angle between $|S\rangle$ and $|x_0^\perp\rangle$. If a state $|\psi\rangle$ is on this plane, O is a reflection operation about $|x_0^\perp\rangle$, and D is a further reflection about $|S\rangle$. The combined effect, i.e. the Grover iteration, is a counterclockwise rotation of angle 2θ . It is easy to see for a large N , $k \approx \frac{\pi}{4\theta} \approx \frac{\pi}{4}\sqrt{N} = O(\sqrt{N})$ applications of the iterator achieves the goal. A simple measurement in the standard basis at the end will reveal $|x_0\rangle$ with high probability.

It can be shown that Grover's algorithm is asymptotically optimal, namely, there is no search algorithm that can do better than $O(\sqrt{N})$ queries.

Let us now come back to a point we glossed over at the beginning of this subsection. How can the unstructured database search problem be phrased in terms of the search problem? It seems that the function f already knows what x_0 , and what is the point of making all these queries? It turns out f just verifies if the input is the desired answer, and we can implement f without knowing what it is.

In the database search problem, the database contains items $\{d_0, d_1, \dots, d_{N-1}\}$. We know that a particular item d_{x_0} we are searching appears exactly once in the database, and we would like to find the index x such that $d_x = d_{x_0}$. We basically need a function f given by Eq. 1.37 that checks this condition. Classically, the oracle gate of f can be built out of a random access memory (RAM) where we can retrieve d_x and a comparison circuit to check $d_x = d_{x_0}$. However, to build this quantum oracle operator O of f , we need a bit more effort.

Let each item in the database be m -bit, and we will use $n \geq \log(N)$ bits for addressing. We also assume that the database is stored in a quantum RAM [35] where we can access a superposition of addresses. We will need three registers with n , m , and m bits respectively.

$$\begin{aligned} & |x\rangle |0\rangle |d_{x_0}\rangle \\ & \xrightarrow{\text{LD}} |x\rangle |d_x\rangle |d_{x_0}\rangle \\ & \xrightarrow{\text{CMP}} (-)^{f(x)} |x\rangle |d_x\rangle |d_{x_0}\rangle \\ & \xrightarrow{\text{LD}} (-)^{f(x)} |x\rangle |0\rangle |d_{x_0}\rangle \end{aligned}$$

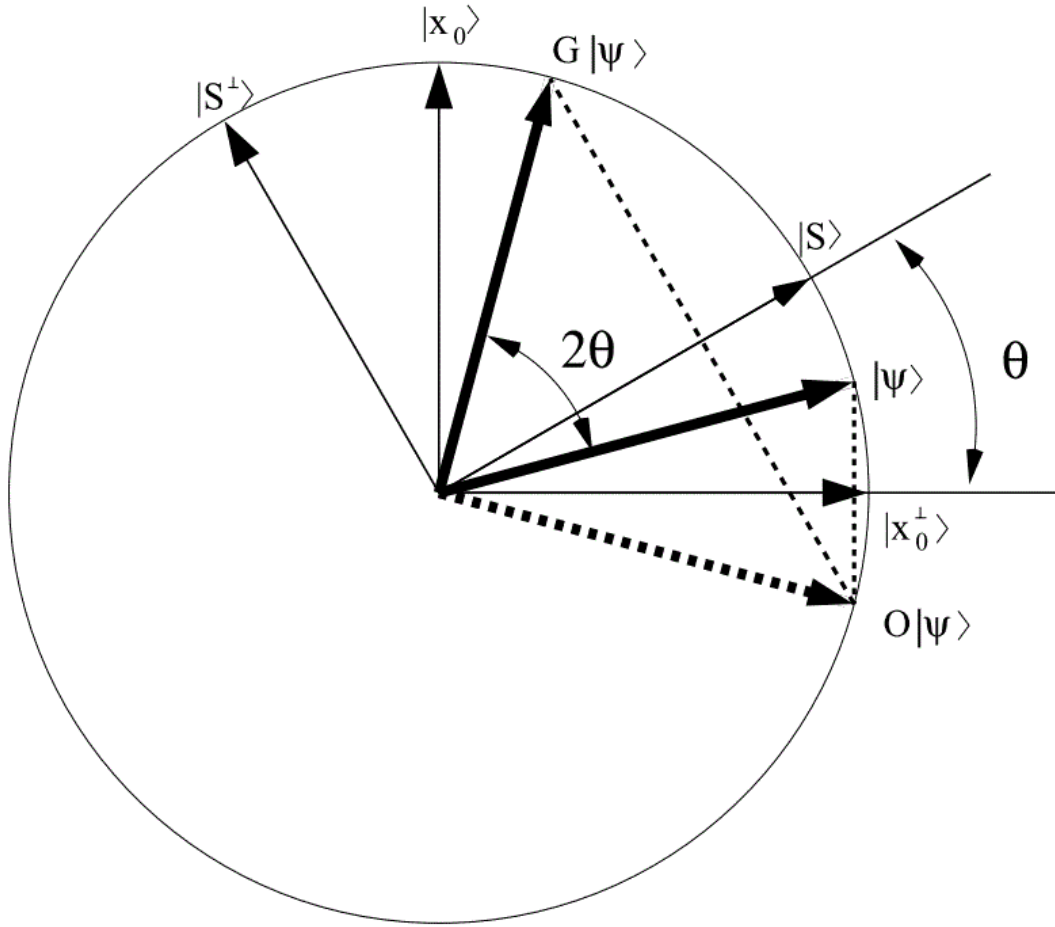


Figure 1.3: Geometric visualization of Grover's iteration [3].

The initial states of the registers are indicated in the diagram above. We first apply the LD operation, which loads from the quantum RAM the item d_x addressed by the first register to the second register: $LD(|x\rangle|y\rangle) = |x\rangle|d_x \oplus y\rangle$. We then apply the CMP operation, which flips the sign of the state if the values of the second and third register are the same. We finally applies the LD operation again to reset the state of the second register. The combined effect of this three unitary operations is exactly the oracle operator indicated in Eq. 1.38 since the last two register values are unchanged. Therefore we constructed this operator without knowing x_0 , and reduced the unstructured database search problem into the standard search problem.

1.4.2 The quantum Fourier transform

The quantum Fourier transform is a unitary operator F on a register of n qubits ($N = 2^n$). It is defined by its action on the basis states:

$$F(|j\rangle) = \frac{1}{\sqrt{N}} \sum_{k=0}^{N-1} \exp(2\pi i j k / N) |k\rangle. \quad (1.42)$$

The transformation of the coefficients of any state under the application of F is exactly the discrete Fourier transform.

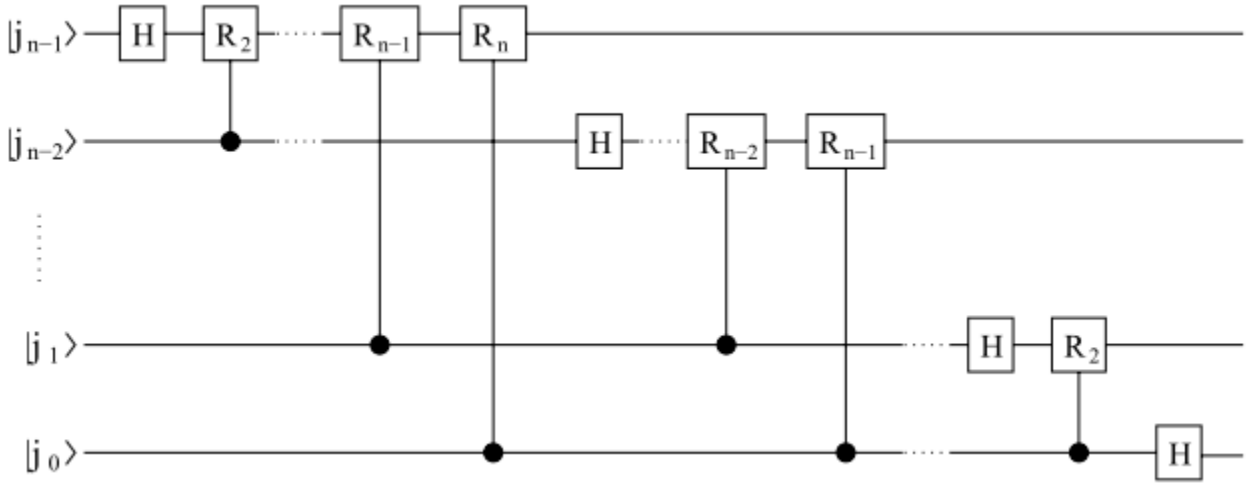


Figure 1.4: A circuit implementing the quantum Fourier transform [3]. The input bits are laid out with the most significant one on the top and output bits with the most significant one on the bottom.

The quantum Fourier transform can be implemented in $O(n^2)$ elementary operation as shown in Fig. 1.4, where R_k in the diagram denotes the phase shift operator $R_z(\frac{2\pi}{2^k})$. The fastest known classical algorithm, the fast Fourier transform, requires $O(N \log(N)) = O(2^n n)$ elementary operations [17], which is exponentially slower than the quantum counterpart. There is a caveat however. The result in the quantum Fourier transform is encoded in the amplitudes of a superposition state and we may not access all the information.

The debut of Shor's algorithm for integer factorization in 1994 revolutionized people's understanding of quantum algorithms. It is believed to be in the complexity class NP but not P , and many modern cryptographic algorithms are based on the hardness of this problem. The best known classical algorithm requires $\exp(O(n^{1/3}(\log n)^{2/3}))$ operations [18] while Shor's algorithm requires only $O(n^2 \log n \log(\log n))$ operations [106]. The Shor's algorithm is based on period finding, which is in turn based on the quantum Fourier transform. Some other applications of the quantum Fourier transform include discrete logarithms, the hidden subgroup problem, and etc.

1.4.3 Conclusions

The class of problems that can be efficiently solved by quantum computers is called BQP (bounded error, quantum, polynomial time). It is the counterpart of BPP (bounded error, probabilistic, polynomial time) on classical computers. It is speculated that BQP contains part of NP but not NP-complete. The integer factorization problem, which is in BQP, is widely believed to be outside P . Please refer to Ref. [citenielsen2010quantum](#) for a detailed discussion. The field of quantum computing is still in its infancy, and there is much to be done before we can tell how powerful quantum computers are.

1.5 Quantum Cryptography

1.5.0.1 Public-key Cryptosystems

In this era of rapid technological and social development, information exchange among people all over the globe becomes increasingly important and frequent. Cryptography helps us encrypt a message so that it can only be decrypted by authorized parties. The most commonly used cryptosystem today is the public-key cryptosystem, which is the foundation for secure online transactions. The sender encrypts the message with the public key of the receiver, and only the receiver can decrypt it because no one else knows the secret key. The function of the public-key cryptosystem relies on the concept of one-way functions with a trapdoor: It takes a classical computer exponentially long time to compute the function in the reverse direction compared with the forward direction without knowing the trapdoor. A well known implementation of the public-key cryptosystem is the RSA algorithm, which is related to the computational complexity of factoring the product of two large prime numbers [74]. However, these kinds of algorithms pose ever increasing security concerns. First, there is no proof of the existence of any one-way function with a trapdoor, and it may be possible to realize the reverse computation of the one-way functions used today with some advancement of mathematics. Second, the quantum factorization algorithm developed by Peter Shor could do the prime factorization (and complete the reverse computation) in polynomial time. These risks of the widely used public-key cryptosystems call for alternative encryption methods.

1.5.0.2 Secret-key Cryptosystems

Secret-key Cryptosystems use the same key, which is kept secret between the sender and the receiver, to encrypt and decrypt the message. The most common example of this kind is the one-time pad. If both parties somehow manage to obtain a complete random key which is at least as long as the message, the sender could send the binary sum of the message and the key, and the receiver could recover the message by subtracting the key from it. The cryptogram does not provide any information to a third party since it is just as random as the secret key. Everything works fine so far, but the problem with the one-time pad lies on the

practical difficulty in distributing such keys to only designated receivers. Authorities that have high security demands would typically use a courier to deliver such keys. However, not only is sending couriers inconvenient, but there is not a “physical principle” that prevents a human from abusing keys. Moreover, one-time pad is so called because it is no longer secure when used more than once. For example, an eavesdropper may distill the binary sum of the original two messages by taking the binary sum of the messages encrypted with the same key. Therefore, we need to keep sending couriers as we have more and more messages to deliver. What we really desire is a method to automatically distribute the secret key whose security is guaranteed by physical laws.

1.5.0.3 Quantum Key Distribution

When traditional information transmission is no longer believed to be secure, quantum mechanics comes into rescue. Some properties of quantum mechanics seem to be designed for cryptography: a measurement will in general perturb a system; it is impossible to clone a quantum state; entanglement creates non-classical correlation between measurement results separated by remote distances. In a classical channel between Alice and Bob, Eve may well intercept the signal, get the information, and resend it to Bob. However, in quantum mechanics, Eve cannot duplicate the signal, and any measurement attempting to obtain information from it might reveal her existence. Therefore, it is feasible to distribute a secret key using a quantum mechanical channel, which is known as quantum key distribution (QKD). It is the main topic in quantum cryptography.

1.5.1 QKD protocols

1.5.1.1 Prepare-and-measure protocols

In prepare-and-measure protocols, Alice sends to Bob a sequence qubits, which encodes a secret key. Bob makes measurements on the qubits received and obtains the key based on the measurement results. These protocols do not require quantum computation or storage, and are feasible to implement nowadays or in near future. The first QKD protocol ever proposed, the BB84 protocol [5], belongs to this category. It is named after its inventor Charles Bennett and Gilles Brassard. According to the protocol, Alice transmits states in a 2-D Hilbert space, for example, the photon spin system. We will work in two different bases, with basis 1 constituting vertical ($|90\rangle$) and horizontal ($|0\rangle$) polarizations, and basis 2 constituting plus 45° ($|45\rangle$) and minus -45° ($|-45\rangle$) polarizations. Furthermore, we interpret $|90\rangle$ and $|45\rangle$ as value 1, $|0\rangle$ and $|-45\rangle$ as value 0 in a binary digit. Alice sends a sequence of photons chosen randomly among these four states, and Bob measures the incoming photons with polarizations chosen randomly between these two bases. Then Alice and Bob communicate through a classical channel about which bases they use to send or measure the photons (not the polarizations) and keep the data when they use the same one. They are left with about half of the digits where their data are perfectly correlated,

which can be used as a secret key. In the protocol, it is crucial that Alice and Bob randomize among the bases and polarizations. Let us suppose Eve intercepts the photons, measures the polarizations in the bases of her choice, and resends them to Bob after her measurements, which is known as the intercept-resend attack. Randomization ensures that there is a 50 percent probability that she uses a different basis compared to the one Alice and Bob use for each qubit; there is also a 50 percent probability that Bob will obtain the right measurement result if the photon is polarized in a different basis. Therefore, Eve will create a 25% error rate, which may well reveal her presence. Also keep in mind that Eve guesses correctly for about 75% of the qubits. There are a lot of protocols similar to BB84. One can use two non-orthogonal states or six states in the 2-D Hilbert space. In the latter, Alice randomizes among six states, which correspond to the intersections of x, y, and z axes with the Poincare sphere centered at the origin, and Bob makes measurements in the bases randomly chosen from the three bases. This protocol will best preserve the symmetry of the system. Other prepare-and-measure protocols include randomizing with unequal probabilities over the states and working in dimensions higher than 2. However, it is far from clear which protocols are most effective.

1.5.1.2 Entanglement based protocols

Entanglement based protocols usually utilize EPR pairs to generate secret keys. They were first developed by Artur Ekert in 1991 [26]. A source generates a sequence of photon pairs in singlet states. One photon in each pair is sent to Alice and the other to Bob, the same setup in the Bell's measurements. Then both of them measure the incoming photon spins with polarizations randomly chosen from the two bases described in the BB84 protocol. Because of the entanglement, they will get perfectly correlated results whenever they use the same measurement basis. Therefore, they could use the scheme in the BB84 to establish the sifted key. Photon pairs in other bell states may also be used. In these protocols, the secret keys are generated by measurements in quantum mechanics and are ensured to be random.

1.5.2 Eavesdropping Analysis

1.5.2.1 Error Correction and Privacy Amplification

Ideally, the sifted key obtained in the protocols described earlier can be used as a one-time pad. However, in a real system there will be a significant Quantum Bit Error Rate (QBER) in the sifted key, due to the imperfectness of the sources and detectors, the loss in the channels of transmission, and potential eavesdropping. However, we need to make our protocols secure even if the QBER is entirely due to Eve's interference. Let us suppose the outcome of their measurements provide Alice, Bob, and Eve random variables a , b , and e , respectively, with a joint probability distribution $P(a, b, e)$. Consequently, the last step in a QKD protocol often uses classical algorithms, first to correct the errors, and then to reduce Eve's information on the final key to a negligible level, a process called privacy amplification [36]. Here, I would

like to state a theorem in information theory [19]: *For a given $P(a,b,e)$, Alice and Bob can establish a secret key (using only error correction and classical privacy amplification) if and only if $I(a,b) \geq I(a,e)$ or $I(a,b) \geq I(b,e)$, where $I(a,b)$ is the mutual information between a and b .* In general, Alice and Bob will first compare part of the sifted key to estimate the QBER and then calculate the mutual information. This theorem guarantees a secure key using only one-way communication if Bob has more information than Eve about Alice's qubits, and they will abort the communication otherwise. A cascade protocol is typically used to make error corrections. This scheme operates in several rounds, and in each round both keys are divided into blocks and the parity of those blocks is compared. If a difference in parity is found then a binary search is performed to find and correct the error. If an error is found in a block from a previous round that had correct parity then another error must be contained in that block; this error is found and corrected as before. This process is repeated recursively, which is the source of the cascade name. After all blocks have been compared, Alice and Bob both reorder their keys in the same random way, and a new round begins. At the end of multiple rounds Alice and Bob will have identical keys with high probability. Privacy amplification uses Alice and Bob's key to produce a new, shorter key, in such a way that Eve has only negligible information about the new key. Let us consider a pedagogical example where Eve knows that each bit of the secret key has a Bernoulli distribution $B(p)$ over 0 and 1 with $\frac{1}{2} < p < 1$. Suppose Alice and Bob divide the key into pairs of bits and form a new key of half the length by taking the binary sum of each pair. Then, to Eve, each bit of the new key has a distribution $B(p')$ with $p' = p^2 + (1-p)^2$. Since $\frac{1}{2} < p' < p$, this process reduces Eve's information about the secret key. In practice, privacy amplification can be done using a universal hash function, chosen at random from a publicly known set of such functions, which takes as its input a binary string of length equal to the key and outputs a binary string of a chosen shorter length. The amount by which this new key is shortened is calculated, based on how much information Eve could have gained about the old key (which is known due to the errors this would introduce), in order to reduce the probability of Eve having any knowledge of the new key to a very low value. In fact, Alice and Bob can still establish a secret key by using advantage distillation even if the conditions in the theorem are not satisfied. As its name suggest, advantage distillation enables Alice and Bob gain an information advantage over Eve despite the initial disadvantage. A simple protocol involves Alice and Bob dividing the keys into pairs of bits and comparing the binary sum of each pair. They discard the entire pair if the sums match and discard the second bit of the pair otherwise. They keep iterate the process until Bob has more information than Eve about Alice's bits. Advantage distillation schemes require two-way communication and are much less efficient. If we use EPR pairs to distribute secret keys, a quantum privacy amplification scheme, called Entanglement Purification Protocols (EPP) offers a brand new way for post-processing received qubits. Alice and Bob can use Local Operation and Classical Communication (LOCC) to purify the partially entangled photon pairs. They let the photon pairs achieve a desired fidelity that Eve will have negligible information on their measurement results. (A secure EPP will be offered in the next section.) Remember that perfect EPR pairs are automatically disentangled with the environment and leak no

information to Eve. Similarly, EPP protocols can use either one-way or two-way classical

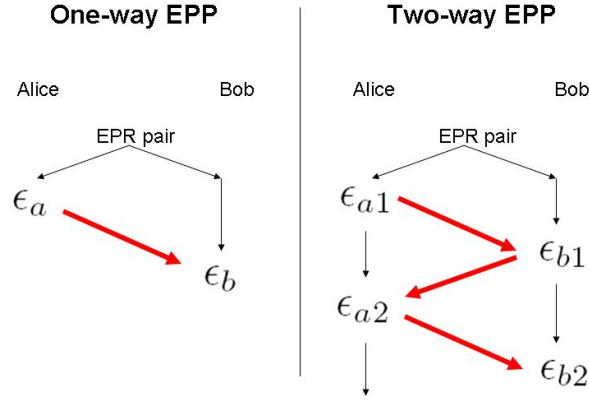


Figure 1.5: Schematic representation of entanglement purification protocols

communication. As shown in the figure above, in a one-way EPP protocol, Alice performs some quantum operation on her qubits (including measurements), and send her measurement results (the red line) to Bob. Bob then manipulates his qubits according to the information received from Alice. When QBER is too large for one-way EPPs to be secure, we may use two-way EPPs, which iterate the process for enough rounds until one-way EPPs are safe to perform.

1.5.2.2 Types of attacks

Let us follow Ref. [36] and discuss several kinds of eavesdropping strategies. Eve can either measure the qubits Alice sends independently, known as an individual attack, or transform and measure multiple qubits coherently, known as a joint attack. However, it is not yet known if the joint attacks are more efficient than the individual attacks. Let us first examine the intercept-resend strategy, the simplest example of the individual attacks, on the BB84 protocol. Eve resends a bit after performing a polarization measurement. Alice's input, a , takes one of two values, and Eve's variable, e , gets one of the four possible results, $|90\rangle$, $|45\rangle$, $|0\rangle$, and $| - 45\rangle$. Their mutual information can be calculated from the following formula [36]:

$$I(a, e) = H(a) + \sum_{a, e} P(a, e) \log_2 P(a|e) \quad (1.43)$$

where $H(a)=1$ is the entropy of a qubit from Alice, $P(a, e)$ and $P(a|e)$ are the joint and conditional probability density. One can compute $P(a|e)$ from the Bayes's theorem since $P(e|a)$ is known. Finally, we get $I(a, e) = 0.5$. This result makes sense, since Eve is certain about half of the qubits Alice sent and knows nothing about the other half. The mutual information between Alice and Bob is calculated by [36]:

$$I(a, b) = 1 + D \log_2 D + (1 - D) \log_2 (1 - D) \quad (1.44)$$

where D is the QBER. If Eve intercepts every qubit, then $D = 0.25$, and $I(a, b) = 0.18 < I(a, e)$. Alice and Bob cannot deduce a secret key as a result. A more sophisticated individual

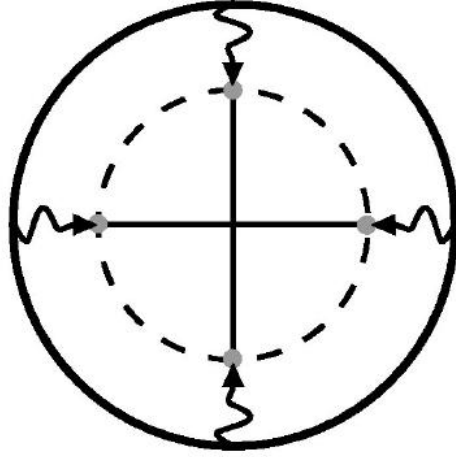


Figure 1.6: Poincare sphere representation of BB84 state in the event of a symmetric attack [36].

attack is the symmetric attack. Eve performs some unitary operation in the joint Hilbert space, $\mathbf{C}^2 \otimes H_e$, where \mathbf{C}^2 is the qubit space and H_e is the space of Eve's probe system. This operation will in general reduce Bob's state to a mixed one, and a symmetric attack relates the mixed state to the original state Alice sends by a simple shrinking factor, shown in Figure 1.6. Eve waits until Alice and Bob announces their bases and takes measurement accordingly. The most effective symmetric attack maximizes the mutual information $I(a, e)$ while keeping QBER fixed. I omit the analysis here, and the resulting mutual information as a function of QBER is presented in Figure 1.7. Below a critical QBER, $D_0 = \frac{1-1/\sqrt{2}}{2} \approx 15\%$, Bob has more information than Eve, and secret-key agreement can be achieved using information reconciliation and privacy amplification. D_0 is precisely the noise threshold above which the Bell's inequality is no longer violated.

1.5.2.3 A proof of conditional security

In eavesdropping analysis, it is desired that our protocols are secure against all kinds of possible attacks, and finding mathematical proofs of the unconditional security is worthwhile. This kind of proofs guarantees the security of information transmission, even if Eve uses any conceivable future technology and all the QBER is attributed to Eve, as long as the attacks obey the laws of quantum mechanics. Sometimes these ultimate proofs are non-existent or hard to find, and people may develop practical proofs of the protocols, which only guarantee securities against specific attacks or implementations [36]. The BB84, the six-state protocol,

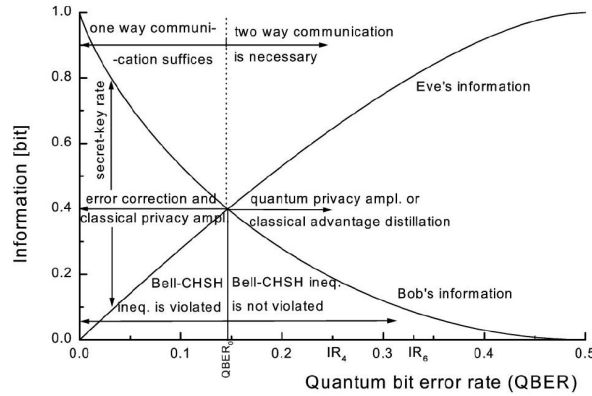


Figure 1.7: Eve's and Bob's information vs the QBER for individual attack against BB84 protocol [36].

and the EPR protocol have been proven secure against any attacks allowed by quantum mechanics, both for sending information using an ideal photon source which only ever emits a single photon at a time, and also using practical photon sources which sometimes emit multi-photon pulses. I will provide some unconditional proofs in the next section. Here, I would like to sketch a security proof of the BB84 protocol under individual attacks since it is conceptually clean. Suppose Bob measures n qubits sent out by Alice in the correct bases. There is a fact that can be understood fairly intuitively but is not straightforward to prove [36]:

$$I(a, e) + I(a, b) \leq 1. \quad (1.45)$$

This inequality sets an upper bound on the total information Bob and Eve know about Alice's qubits. Namely, the information cannot exceed 1 per qubit. Therefore, we need $I(a, b) \geq 1/2$ on average to extract a secret key. Combining this with Equation 1.44 yields the safety range of the QBER: $D \leq 11\%$. In the classical post-processing, Alice and Bob first randomly choose half of the bits in the key to get the QBER and discard them. Since they are exponentially certain the rest sequence of bits will have a similar QBER, they can safely proceed with classical error correction and privacy amplification if the QBER is below 11%. This proof also valid if the key is much longer than the number of qubits that Eve attacks coherently, so that the Shannon information we used represents averages over many independent realizations of classical random variables [36]. However, we still have the same 11% bound for any kind of attacks, which will be presented in the next subsection. This bound is clearly consistent with the 15% bound mentioned earlier in the symmetric attack. It is widely speculated that we need the more stringent 11% bound only if Eve has the power to coherently attack as many qubits as she wants.

1.5.3 Proofs of Unconditional Security

In joint attacks, the error caused by or information gained by Eve for one qubit may be correlated with that of another, which makes it hard to bound Eve's information by simply looking at QBER. To prove that a protocol is secure against any kind of attacks Eve may use is not easy. Such an unconditional proof was first suggested by D. Mayers when he gave a speech in 1996 in Italy, although at that time hardly anyone in the audience understood him. Two years later, H. Lo and H. F. Chau published a paper which rigorously proves the unconditional security of the EPR protocol using the Mayer's schemes [66]. In 2000, P. Shor, and J. Preskill systematically reduced the EPR protocol to a BB84 protocol without compromising the security and obtained the 11% security bound for BB84 QBER [107]. Some generalizations and improvement of this result was further developed. Before delving into the proofs, we need to know the mathematical definition of security: A QKD protocol is secure if, for any security parameters $s > 0$ and $r > 0$, and for any eavesdropping strategy, either the protocol aborts with probability at least $1 - s$, or it guarantees that Eve's mutual information with the final key is less than r if the protocol succeeds. The reason we allow the protocol to abort as an alternative is that demanding Eve has negligible information all the time is too strong to achieve. Consider a simple case where Eve intercepts and resends every bit, which will cause a reasonable protocol to abort. However, in the extremely unlikely circumstance where Eve passes the security check performed by Alice and Bob, Eve will have non-negligible information about the final key. There are a few additional assumptions I need to make in order to validate the proofs in the following subsections. (There are proofs relaxing some of these constraints, but I will not discuss them in this paper.)

- Alice and Bob have perfect photon generators and detectors.
- Eve cannot access Alice and Bob's encoding and decoding devices.
- Alice and Bob possess truly random number generators.
- The classical communication channel is authentic.

1.5.3.1 The modified Lo-Chau protocol

In this subsection, I would like to present and prove the security of an EPR protocol, the modified Lo-Chau protocol [107]:

1. Alice creates $2n$ EPR pairs in the state $|\psi^+\rangle = (|00\rangle + |11\rangle)/\sqrt{2}$.
2. Alice selects a random $2n$ bit string b , and performs a Hadamard transformation on the second half of each EPR pair for which b is 1.
3. Alice sends the second half of each EPR pair to Bob.
4. Bob receives the qubits and publicly announces this fact.

5. Alice randomly selects n of the $2n$ encoded EPR pairs to serve as check bits to test for Eve's interference.
6. Alice announces the bit string b , and which n EPR pairs are to be check bits.
7. Bob performs Hadamard transformations on the qubits where b is 1.
8. Alice and Bob each measure their halves of the n check EPR pairs in the Z basis and share the results. If more than t of these measurements disagree, they abort the protocol.
9. Alice and Bob measure their remaining n qubits according to the check matrix for a pre-determined $[n, m]$ quantum code correcting up to $t(1 + \epsilon)$ errors. They share the results, compute the syndromes for the errors, and then correct their states, obtaining m nearly perfect EPR pairs.
10. Alice and Bob measure the EPR pairs in the Z basis to obtain a shared secret key.

The basic idea in this protocol is to obtain the QBER from the check qubits and then perform quantum error corrections. Because an operation element of any quantum operation can be written as a linear superposition of tensor products of identity and Pauli matrices (I , σ_x , σ_y and σ_z), we can reduce a continuous set of transformations by Eve to a discrete set of Pauli operations [38]. In step 2, Alice transforms half of the qubits to create symmetry between Z basis and X basis and enable them to detect both bit flip and phase flip errors (and simultaneous occurrences of the two). When the number of disagreements of the check qubits is bound by t , Alice and Bob will be exponentially certain that the remaining qubits have less than $t(1 + \epsilon)$ errors. Therefore, the fidelity of their m EPR pairs is exponential close to 1 after they perform error corrections in Step 9 [38]. High fidelity implies low entropy. One can prove the following: if $F(\rho, |\psi^+\rangle^{\otimes m})^2 > 1 - 2^{-s}$, then $S(\rho) < (2m + s + 1/\ln 2)2^{-s} + O(2^{-2s})$, where ρ is the density matrix of Alice and Bob's photon pairs [80]. Take the state the whole world to be pure, the entropy of the rest of the world is $S(\rho_{envi}) = S(\rho)$. Even if the rest of the world is at Eve's disposal, and she is able to make any kind of measurements she wants, the mutual information between Eve's measurement result and the final key is bound by $S(\rho_{envi})$, according to Holevo's theorem. Since Eve's information about the final key may be made as small as possible, the modified Lo-Chau protocol is unconditionally secure. However, in this protocol, Bob needs to wait for Alice's classical information before making transformations and measurements. Therefore, quantum memory is required to store the qubits for a reasonably long time. Moreover, the quantum error correction scheme requires quantum computers. Neither quantum memory nor quantum computation is not likely to realize in near term. Therefore, the construction of a practical, secure BB84 protocol is desired.

1.5.3.2 The secure BB84 protocol

In this section, we follow the proof given by Shor and Preskill [107] and systematically reduce the manifestly secure EPR protocol to a one-way BB84 protocol. The key idea in this reduction is to bring Alice's measurements to before she sends the qubits. Because the operations on Alice's bits commute with all the operations on the Hilbert space of the rest of the world, performing measurements beforehand makes no difference for Bob and Eve. Therefore, we can first bring forward Alice's measurements on the check qubits. The result is to change each EPR state to a state randomly chosen from $|00\rangle, |11\rangle$ for those bits where b is 1. Notice the replaced states are not entangled at all, and Alice only needs to create the second qubit of each pair and send it to Bob. In order to further reduce the modified Lo-Chau protocol, we assume Alice and Bob use an $[n, m]$ CSS code of C_1 over C_2 , $CSS(C_1, C_2)$.² In this scheme, Alice and Bob both measure the stabilizer generators given by the parity check matrices H_1 and H_2^\perp on their n qubits. Alice sends Bob her measurement results (a binary string), and Bob performs Pauli operations to correct error according to the error syndromes. It can be shown that Alice's syndrome measurements collapse her n qubits with equal probability to codeword spaces corresponding to a family of equivalent $CSS(C_1, C_2)$ codes, and her final measurements collapse the qubits randomly into one of the codeword states, $\frac{1}{\sqrt{|C_2|}} \sum_{\omega \in C_2} |v_k + \omega\rangle$, where v_k is a representative of one of the 2^m cosets of C_2 in C_1 . Therefore, Alice's measurements on her half of the n EPR pairs are equivalent to choosing a random v_k and sending the corresponding $CSS(C_1, C_2)$ encoded states. Through additional simplification, Alice may encode v_k in the Z basis, and Bob's decoding procedure is removed. [80] In the final step of the reduction, we double the qubits Alice sends to Bob. Bob randomly applies Hadamard transformations to the qubits, and after Alice announces b , they throw away about half the qubits where only one of them makes the transformation. This way, Bob does not need store the qubits until Alice announces the string b . Notice Alice and Bob may replace the random Hadamard transformations with sending and measuring qubits randomly in X and Z bases. We obtain the following BB84 protocol with classical post-processing [107]:

1. Alice creates $(4 + \delta)n$ random bits.
2. Alice chooses a random $(4 + \delta)n$ -bit string b . For each bit, she creates a state in the Z basis (if the corresponding bit of b is 0) or the X basis (if the bit of b is 1).
3. Alice sends the resulting qubits to Bob.
4. Bob receives the $(4 + \delta)n$ qubits, measuring each in Z or X basis at random.

²CSS codes are derived from their classical analogs. Suppose C_1 and C_2 are $[n, k_1]$ and $[n, k_2]$ classical linear codes respectively, such that $C_2 \subset C_1$, and both C_1 and C_2^\perp can correct errors on up to t bits. Then $CSS(C_1, C_2)$ is an $[n, k_1 - k_2]$ quantum error-correcting code which can correct arbitrary errors on up to t qubits [80].

5. Alice announces b .
6. Bob discards any results where he measured in a basis different from Alice prepared. With high probability, there are at least $2n$ bits left (if not, abort the protocol). Alice decides randomly on a set of $2n$ bits to use for the protocol and chooses at random n of these to be check bits.
7. Alice and Bob announce the values of their check bits. If more than t of these values disagree, they abort the protocol.
8. Alice announces $u + v$, where v is the string consisting of the remaining non-check bits, and u is a random codeword in C_1 .
9. Bob subtracts $u + v$ from his code qubits, $v + \text{error}$, and corrects the result, $u + \text{error}$, to a codeword in C_1 .
10. Alice and Bob use the coset of $u + C_2$ as the key.

The last two steps of this protocol can be interpreted as error correction and privacy amplification. The unconditional security of this BB84 protocol follows from that of the modified Lo-Chau protocol. We can calculate the safety range for the QBER. According to Shannon's bound, CSS codes exist with asymptotic key rate $k/n = 1 - 2H(t/n)$, where $H(p) = -p \log(p) - (1 - p) \log(1 - p)$. (To apply the Shannon's bound, we need to add some additional steps to the protocol which assures the errors occur randomly [107].) This key rate goes to 0 as t/n , the QBER, reaches 11%. This is exactly the bound on QBER assuming individual attacks. Therefore, this one-way BB84 protocol can tolerate QBER up to 11%.

1.5.3.3 Other secure protocols

We can use a similar scheme to construct a secure six-state protocol. In fact, if we randomly mix the three bases X, Y, Z (instead of two bases by applying Hadamard transformations) in the modified Lo-Chau protocol, we can reduce it to the six-state protocol with almost the same procedures. Notice the modified Lo-Chau protocols with CSS error-correcting codes are effectively one-way EPPs, and what we did is a reduction from one-way EPPs to one-way prepare-and-measure protocols. Gottesman and Lo showed in 2001 that carefully chosen two-way EPPs can be reduced to two-way prepare-and-measure protocols [38]. Two-way communications greatly improve the error tolerance of the cryptosystems at the expense of efficiency.

1.5.3.4 Bounds on QBER

In this section, I would like to summarize the security bounds on QBER for prepare-and-measure protocols, shown in Tab. 1.1. The upper bounds come from eavesdropping strategies

that compromise the security of cryptosystems for any protocol Alice and Eve may use, and the lower bounds come from QKD protocols provably secure against any eavesdropping strategies. Shor and Preskill's proof provides the 11% lower bound for the one-way BB84, and Lo slightly improved the result for the six-state protocol. The lower bounds for the two-way protocols are obtained by Chau [11]. The isotropic optimal cloning eavesdropping strategy, which copies states with fidelity $5/6$, gives the $1/6$ upper bound on the one-way six-state protocol. No protocol can generate a secure key with this QBER because Eve may receive as much information from Alice as Bob may and is able to produce a final key just like Bob. For the one-way BB84 protocol, which is biased towards the X and Z bases, Eve can further optimize the cloning strategy and compromise the security of cryptosystems with a slightly lower QBER. Both two-way upper bounds come from the intercept-resend strategy. For this strategy, Bob's measurement results can be interpreted as a classical random variable whose distribution is completely known by Eve. No matter what Alice and Bob do, Alice cannot know more about Bob's variable than Eve does. Therefore, the corresponding QBER is not secure. It is interesting to notice that the provably secure 27.6% QBER for the six-

Table 1.1: Security bounds of QBER on the BB84 and the six-state protocols

The BB84 Protocol		
	one-way	two-way
Upper bound	14.6%	$1/4$
Lower bound	11.0%	20.0%
The six-state Protocol		
	one-way	two-way
Upper bound	$1/6$	$1/3$
Lower bound	12.7%	27.6%

state protocol is higher than the upper bound of QBER for a secure BB84, which indicates that the six-state protocol is more error tolerant than BB84.

1.5.4 Conclusions

Quantum cryptography is an illuminating application of Quantum mechanics. Its security relies on the fundamental physical principles rather than computational complexity. As of March 2007 the longest distance over which quantum key distribution has been demonstrated using optic fiber is 148.7 km, achieved by Los Alamos/NIST using the BB84 protocol [44]. Currently, there are also several companies offering commercial quantum cryptography systems, such as MagiQ Technologies in New York. With rapid improving photon generators, detectors, and optic fiber networks, the widespread adoption of quantum cryptography will not be far away.

Chapter 2

Open Quantum Systems

2.1 Introduction

Real quantum systems are rarely isolated. The coupling to an environment typically leads to dissipative processes such as decoherence of the system. Such open quantum system processes pose a tremendous challenge to quantum information processing. It is crucial to understand open quantum system evolution in order to effectively track and control a quantum state. In addition, we may intentionally need a quantum system to be open in order to perform a measurement. Different measurement operations can be realized by engineering the measurement apparatus and their interaction with the system. This chapter provides some preliminary ways to describe open quantum systems. Sec. 2.2 introduces the Lindblad master equation, which is a theoretically important concept that describes the most general time-homogeneous Markovian processes. In Sec. 2.3 we will see that open quantum system evolution can be approximated by the Lindblad master equation under certain assumptions. Sec. 2.4 introduces continuous-in-time measurement processes where we continuously monitor the environment the open system is coupled to. In Sec. 2.5, we will look at a particular measurement technique, photodetection, which is commonly used today.

2.2 The Lindblad Master Equation

Master equations are widely used to describe the temporal evolution of many open quantum systems. In this section, we will follow Ref. [4] and derive the Lindblad master equation (the most general type of Markovian and time-homogeneous master equation) within the framework of the quantum operation formalism.

The Markovian and time-homogeneous master equation takes the form of

$$\dot{\rho} = \mathcal{L}\rho, \tag{2.1}$$

and we would like to find a generic expression for this Liouvillian superoperator¹. We assume a quantum operation evolves the state from $\rho(t)$ to $\rho(t + dt)$. In the Kraus representation,

$$\rho(t + dt) = S(t, t + dt)\rho(t) = \sum_{k=0}^{M-1} E_k \rho(t) E_k^\dagger, \quad (2.2)$$

where $M(\leq N^2)$ is the number of Kraus operators. To ensure that $S(t, t) = 1$, we may quite generally write the Kraus operators for this infinitesimal transformation as follows (See Sec. 6.2.2 in [4]):

$$E_0 = I + \frac{1}{\hbar}(-iH + K)dt, \quad (2.3a)$$

$$E_k = L_k \sqrt{dt}, \quad (k = 1, \dots, M - 1). \quad (2.3b)$$

where H and K are Hermitian operators and $\{L_k\}$ are called Lindblad operators. The completeness relation for the Kraus operators, Eq. 1.19, then becomes

$$K = -\frac{\hbar}{2} \sum_{k=1}^{M-1} L_k^\dagger L_k. \quad (2.4)$$

Plugging the expression for E_k into Eq. 2.2 and ignoring higher order terms in dt , we immediately identify the Liouvillian superoperator as

$$\mathcal{L}\rho = -\frac{i}{\hbar}[H, \rho] + \sum_{k=1}^{M-1} \mathcal{D}[L_k]\rho, \quad (2.5)$$

where the operator (A) dependent superoperator $\mathcal{D}[A]$ is defined as

$$\mathcal{D}[A]\rho \equiv A\rho A^\dagger - \frac{1}{2}(A^\dagger A\rho + \rho A^\dagger A). \quad (2.6)$$

Eq. 2.1 and 2.5 gives the master equation in the Lindblad form.

2.3 Open Quantum Systems and Born-Markov Approximation

In this section, we will follow Ref. [9] and show that the Lindblad master equation describes the dynamics of many open quantum systems under certain assumptions and approximations.

We once again consider a system S coupled to a bath B . The Hamiltonian for the total system (which is assumed to be constant) can be written as follows:

$$H = H_S + H_B + H_I, \quad (2.7)$$

¹This Liouvillian superoperator is the generator of the so called quantum dynamical semigroup.

where H_S and H_B are the free Hamiltonians of the system and the bath respectively, and H_I is the interaction between them. H_I can be expanded in the following form:

$$H_I = \sum_{\alpha} A_{\alpha} \otimes B_{\alpha}, \quad (2.8)$$

where A_{α} and B_{α} are Hermitian operators acting on the system and the bath. In the following derivation of the master equation, the interaction picture will be used. Let us assume the system and the bath start out in the product state:

$$\rho(0) = \rho_S(0) \otimes \rho_B(0), \quad (2.9)$$

where $\rho_B(0)$ is assumed to be a stationary state of H_B , e.g., the thermally equilibrium state. The bath correlation functions, which will come in handy soon, are defined as

$$C_{\alpha\beta}(t) \equiv \langle B_{\alpha}(s) B_{\beta}(s-t) \rangle. \quad (2.10)$$

Here, the RHS is independent of s for a stationary ρ_B . The correlation functions typically decay exponentially with t , and the characteristic time scale τ_B for the decay is called the correlation time of the bath. The dynamics of the total density matrix is given by

$$\dot{\rho}(t) = -i[H_I(t), \rho(t)], \quad (2.11)$$

which can be written in the following integral form:

$$\rho(t) = \rho(0) - i \int_0^t ds [H_I(s), \rho(s)]. \quad (2.12)$$

Without loss of generality, we can assume $\langle B_{\alpha}(t) \rangle = 0$. If this is not true, we can redefine B_{α} as $B_{\alpha} - \langle B_{\alpha} \rangle$ and move $\langle B_{\alpha} \rangle A_{\alpha}$ to the system Hamiltonian. As a consequence,

$$\text{Tr}_B[H_I(t), \rho(0)] = 0. \quad (2.13)$$

Inserting Eq. 2.12 into the right-hand side(RHS) of Eq. 2.11 and tracing over the bath, we obtain

$$\dot{\rho}_S(t) = - \int_0^t ds \text{Tr}_B[H_I(t), [H_I(s), \rho(s)]]. \quad (2.14)$$

We first employ the so called Born approximation. This states that if the system-bath coupling is sufficiently weak, the bath is negligibly affected by the system, and the total state $\rho(s)$ on the RHS of Eq. 2.14 can be approximated by $\rho_S(s) \otimes \rho_B(0)$.² To simplify the equation further, we perform the Markov approximation and replace $\rho_S(s)$ with $\rho_S(t)$. This can be justified if $\tau_B \ll \tau_R$, where τ_R is the relaxation time of the system, namely, the time

²Please be aware that unlike this expression, the actual total state will be entangled in general. Here, we are just using lower order approximations to the state in an expression to calculate higher order corrections.

over which $\rho_S(t)$ changes significantly. We now have the following Redfield Equation which is local in time:

$$\dot{\rho}_S(t) = - \int_0^t ds \text{Tr}_B[H_I(t), [H_I(s), \rho_S(t) \otimes \rho_B]]. \quad (2.15)$$

To further simplify the expression, we can approximate 0 with $-\infty$ for the lower bound of integral if we only care about the dynamics on the time scale much longer than τ_B . All the above approximations are collectively referred to as the Born-Markov approximation.

The dynamical equation arising from the Born-Markov approximation is still not time-homogeneous³. To proceed, let us denote the eigenvalues of H_S by ϵ and the projection onto the eigenspace belonging to ϵ by $\Pi(\epsilon)$. Then we can define the eigenoperators (in the Schrodinger picture)

$$A_\alpha(\omega) \equiv \sum_{\epsilon' - \epsilon = \omega} \Pi(\epsilon) A_\alpha \Pi(\epsilon'). \quad (2.16)$$

It is not hard to see that

$$\sum_\omega A_\alpha(\omega) = \sum_\omega A_\alpha^\dagger(\omega) = A_\alpha. \quad (2.17)$$

Hence, the interaction Hamiltonian can be expressed as

$$H_I(t) = \sum_{\alpha, \omega} e^{-i\omega t} A_\alpha(\omega) \otimes B_\alpha(t). \quad (2.18)$$

We now introduce the one-sided Fourier transforms:

$$\Gamma_{\alpha\beta}(\omega) \equiv \int_0^\infty C_{\alpha\beta}(t) e^{i\omega t} dt. \quad (2.19)$$

With a little bit of algebra, the master equation under the Born-Markov approximation can be rewritten as

$$\dot{\rho}_S(t) = \sum_{\omega, \omega'} \sum_{\alpha, \beta} e^{i(\omega' - \omega)t} \Gamma_{\alpha\beta}(\omega) (A_\beta(\omega) \rho_S(t) A_\alpha^\dagger(\omega') - A_\alpha^\dagger(\omega') A_\beta(\omega) \rho_S(t)) + \text{h.c.} \quad (2.20)$$

In order to obtain the Markovian master equation, we need to make a rotating wave approximation. The intrinsic time scale of the system τ_S is set by the typical value of $|\omega' - \omega|^{-1}$, the reciprocal of level spacings. If $\tau_S \ll \tau_R$, the $\omega' \neq \omega$ terms in Eq.2.20 oscillate rapidly and have negligible contribution to the dynamics. We thus have

$$\dot{\rho}_S(t) = \sum_\omega \sum_{\alpha, \beta} \Gamma_{\alpha\beta}(\omega) (A_\beta(\omega) \rho_S(t) A_\alpha^\dagger(\omega) - A_\alpha^\dagger(\omega) A_\beta(\omega) \rho_S(t)) + \text{h.c.} \quad (2.21)$$

Let us define two components of the one-sided Fourier transforms:

$$S_{\alpha\beta} \equiv \frac{1}{2i} (\Gamma_{\alpha\beta}(\omega) - \Gamma_{\beta\alpha}^*(\omega)), \quad (2.22)$$

³And it does not guarantee a quantum dynamical semigroup.

and

$$\gamma_{\alpha\beta}(\omega) \equiv \Gamma_{\alpha\beta}(\omega) + \Gamma_{\beta\alpha}^*(\omega) = \int_{-\infty}^{+\infty} C_{\alpha\beta}(t) e^{i\omega t} dt. \quad (2.23)$$

It can be shown that $\gamma_{\alpha\beta}(\omega)$ form a positive semi-definite matrix [9].

With these definitions we finally obtain the desired Markovian master equation (in the interaction picture):

$$\dot{\rho}_S(t) = -\frac{i}{\hbar} [H_{LS}, \rho_S(t)] + \mathcal{D}(\rho_S(t)). \quad (2.24)$$

H_{LS} is the Lamb shift Hamiltonian, which is

$$H_{LS} = \sum_{\omega} \sum_{\alpha, \beta} S_{\alpha\beta}(\omega) A_{\alpha}^{\dagger}(\omega) A_{\beta}(\omega). \quad (2.25)$$

It commutes with the system Hamiltonian and causes a shift in the intrinsic energy levels of the system. The dissipator term takes the form

$$\mathcal{D}(\rho_S) = \sum_{\omega} \sum_{\alpha, \beta} \gamma_{\alpha\beta}(\omega) (A_{\beta}(\omega) \rho_S(t) A_{\alpha}^{\dagger}(\omega) - \frac{1}{2} \{A_{\alpha}^{\dagger}(\omega) A_{\beta}(\omega), \rho_S\}). \quad (2.26)$$

This dissipator can be brought into the Lindblad form (Eq. 2.5 and 2.6) by diagonalizing the matrices $\gamma_{\alpha\beta}(\omega)$ (where the two layers of summation can be collectively indexed by k) [9].

In conclusion, the Lindblad master equation can be used to describe a general open quantum system evolution under the aforementioned approximations and assumptions. In the next chapter, we will see a more accurate (and more complicated) way to describe the evolution, using the Hierarchical Equations of Motions [52], and compare the results.

2.4 Weak Measurements

For a typical generalized measurement, the state of the quantum system is strongly perturbed by the measurement. For a weak measurement, the state either has an infinitesimal probability to change appreciably (weak measurement of the first kind), or an appreciable probability to change infinitesimally (weak measurement of the second kind). As a result, the unconditioned state is only perturbed weakly and very little information is revealed by the measurement. This infinitesimal change is characterized by a quantity $\epsilon \ll 1$. For a continuous-in-time measurement, the effect of each infinitesimal time dt is a weak measurement with $\epsilon = k dt$, where k is called the measurement strength.⁴ The evolution of a quantum state under such continuous-in-time measurement form a quantum trajectory. Most experimental measurements are continuous-in-time measurements, as it takes time to

⁴From the point of view of weak measurement, k should really be called measurement strength per unit time.

collapse the state of a system. It has also been shown that weak measurements are universal in the sense that any generalized measurement can be decomposed into a sequence of weak measurements without the use of an ancilla [83]. Therefore, it is both theoretically and experimentally important to formulate weak measurements.

We shall use a single qubit with $H = 0$ as a simple example to illustrate the aforementioned two kinds of weak measurement. For the first kind, let us examine a generalized measurement with the following two operation elements [10]:

$$M_0 = |0\rangle\langle 0| + \sqrt{1-\epsilon}|1\rangle\langle 1|, \quad (2.27a)$$

$$M_1 = \sqrt{\epsilon}|1\rangle\langle 1|. \quad (2.27b)$$

It is easy to see that they satisfy the completeness relation. Let us define $c = |1\rangle\langle 1|$ and write

$$M_0 = \sqrt{I - \epsilon c^\dagger c}, \quad (2.28a)$$

$$M_1 = \sqrt{\epsilon}c. \quad (2.28b)$$

If a state ψ is measured, we have probability $1 - \epsilon\|c|\psi\rangle\|^2$ of getting outcome 0 with (unnormalized) post-measurement state

$$|\psi\rangle'_1 \approx (I - \frac{\epsilon}{2}c)\psi \quad (2.29)$$

and probability $\epsilon\|c|\psi\rangle\|^2$ of getting outcome 1 with (unnormalized) post-measurement state

$$c|\psi\rangle. \quad (2.30)$$

Therefore, we usually have outcome 0 and the state changes infinitesimally; very rarely we have outcome 1 and the state changes significantly. Typically, this rare outcome 1 event will reveal a lot of information about the state of the system. For $c = |1\rangle\langle 1|$, it simply means the state collapses to $|1\rangle$. Let us take this measurement as continuous-in-time and get an evolution equation for $\psi(t)$. We write $\epsilon = dt$; k is set to 1 here because it can always be absorbed in c . Let us use $dN(t)$ as the indicator random variable for outcome 1 to happen during $[t, t + dt]$. Then

$$E[dN(t)] = dt\|c|\psi\rangle\|^2. \quad (2.31)$$

From the post-measurement states and probabilities, it is straightforward to obtain the following Stochastic Schrodinger Equation(SSE) (Eq. 4.19 in Ref. [130]):

$$d|\psi(t)\rangle = \left[dN(t) \left(\frac{c}{\sqrt{\langle c^\dagger c(t) \rangle}} - 1 \right) + dt \left(\frac{1}{2} \langle c^\dagger c \rangle(t) - \frac{1}{2} c^\dagger c \right) \right] |\psi(t)\rangle. \quad (2.32)$$

If we work with density operators, the Stochastic Master Equation (SME) for the above dynamics is (Eq. 4.22 in Ref. [130]):

$$d\rho(t) = \left\{ dN(t)\mathcal{G}[c] - dt\mathcal{H}\left[\frac{1}{2}c^\dagger c\right] \right\} \rho(t) \quad (2.33)$$

where

$$\mathcal{G}[A]\rho = \frac{A\rho A^\dagger}{\text{Tr}[A\rho A^\dagger]} - \rho, \quad (2.34)$$

$$\mathcal{H}[A]\rho = A\rho + \rho A^\dagger - \text{Tr}[A\rho + \rho A^\dagger]\rho. \quad (2.35)$$

Eq. 2.33 is the conditioned master equation, where evolution depends on the outcome of measurements. The evolution of $\rho(t)$ with a particular noise realization $dN(t)$ constitutes a quantum trajectory. The evolution is continuous whenever $dN(t) = 0$. However, a discontinuity, which is called a quantum jump, happens when $dN(t) = 1$. By averaging over the measurement noise, the evolution of the unconditioned state turns out to be [130]:

$$\dot{\rho} = \mathcal{D}[c]\rho \quad (2.36)$$

This is just the Lindblad master equation we encountered in Sec. 2.2. Please be aware that we did not assume any specific form for the operator c .

Let us now examine the second kind of weak measurement on a qubit. Consider the following two operation elements [10]:

$$M_0 = \sqrt{\frac{1}{2} + \sqrt{\epsilon}} |0\rangle \langle 0| + \sqrt{\frac{1}{2} - \sqrt{\epsilon}} |1\rangle \langle 1|, \quad (2.37a)$$

$$M_1 = \sqrt{\frac{1}{2} - \sqrt{\epsilon}} |0\rangle \langle 0| + \sqrt{\frac{1}{2} + \sqrt{\epsilon}} |1\rangle \langle 1|. \quad (2.37b)$$

Because both operation elements are infinitesimally different from $I/\sqrt{2}$, both outcomes appear with roughly $\frac{1}{2}$ probability and the state changes infinitesimally. Also, little information is gained from the measurement. If we write $\epsilon = dt$, we can obtain the following SME (conditioned on the measurement outcome) for the qubit density operator $\rho(t)$ [10]:

$$d\rho(t) = \mathcal{D}[\sigma_z]\rho(t)dt + \mathcal{H}[\sigma_z]\rho(t)dW. \quad (2.38)$$

where dW is a Wiener increment, which satisfies mean $E[dW] = 0$ and variance $E[dW^2] = dt$. dW captures the diffusive behavior that is the continuous limit of small quantum jumps. The evolution for the unconditioned state is again described by a Lindblad master equation:

$$d\rho(t) = \mathcal{D}[\sigma_z]\rho(t)dt. \quad (2.39)$$

Next let us look at an example where the Hilbert space is continuous. We will examine a weak position measurement on the 1D position space $L^2(\mathbb{R})$ [58] with the following operation elements labeled by the continuous variable α :

$$M(\alpha) = \left(\frac{4\epsilon}{\pi}\right)^{\frac{1}{4}} \int_{-\infty}^{\infty} \exp[-2\epsilon(x - \alpha)^2] |x\rangle \langle x| dx. \quad (2.40)$$

It is easy to check that the completeness relation $\int_{-\infty}^{\infty} M(\alpha^\dagger)M(\alpha)d\alpha = 1$ is satisfied. Because it is Gaussian weighted sum of position projectors centered around α , $M(\alpha)$ can be regarded as a ‘weak’ projector onto position α . A post-measurement state $M(\alpha)|\psi\rangle$ is only infinitesimally different from the pre-measurement state $|\psi\rangle$ (so it shall be interpreted as the weak measurement of the second kind).

We will regard the measurement as continuous-in-time and set $\epsilon = kt$ as usual. Let us derive the probability distribution of α when such a measurement is performed on a state ψ [58]:

$$\begin{aligned} P(\alpha) &= \|A(\alpha)|\psi\rangle\|^2 \\ &= \left(\frac{4kdt}{\pi}\right)^{1/2} \int_{-\infty}^{\infty} |\psi(x)|^2 \exp[-4kdt(x - \alpha)^2] dx \\ &\approx \left(\frac{4kdt}{\pi}\right)^{1/2} \exp[-4kdt(\alpha - \langle X \rangle)^2]. \end{aligned} \quad (2.41)$$

At the last step, we have treated $|\psi(x)|^2$ as a delta function centered at its average, $\delta(x - \langle X \rangle)$, because dt is small. Therefore, α can also be written as the following stochastic variable

$$\alpha = \langle X \rangle + \frac{1}{\sqrt{8k}} dW/dt. \quad (2.42)$$

where dW is a Wiener increment. Jacobs and Steck have worked out the post measurement state as follows [58]:

$$\begin{aligned} |\psi(t + dt)\rangle &\propto M(\alpha)|\psi(t)\rangle \\ &\propto \exp\{-2kdtX^2 + X[4k\langle X \rangle dt + (2k)^{1/2}dW]\} |\psi(t)\rangle \\ &\propto \{1 - [kX^2 - 4kX\langle X \rangle]dt + (2k)^{1/2}XdW\} |\psi(t)\rangle. \end{aligned} \quad (2.43)$$

In the second line, we have written α in terms of dW and in the third line we have expanded everything to $O(dt)$. Normalizing this gives the following SSE (Eq. 30 in [58]):

$$d|\psi\rangle = -k(X - \langle X \rangle)^2 dt + (2k)^{1/2}(X - \langle X \rangle)dW |\psi\rangle. \quad (2.44)$$

The corresponding SME can be written as (Eq. 32 in [58])

$$d\rho = 2k\mathcal{D}[X]\rho dt + \sqrt{2k}\mathcal{H}[X]\rho dW, \quad (2.45)$$

with \mathcal{H} given by Eq. 2.35 and \mathcal{D} given by Eq. 2.6. The unconditioned master equation (averaged over the measurement records) is again in the Lindblad form:

$$d\rho = 2k\mathcal{D}[X]\rho dt. \quad (2.46)$$

Weak measurements on a two-level system and on $L^2(\mathbb{R})$ can both be realized experimentally. Direct photodetection of the fluorescence of a two-level atom can realize a weak

measurement with $c = \sigma_-$ jumps [122]. A circuit-QED system can implement a weak measurement of the Pauli operators on a transmon qubit [61]. An optical cavity can be used to weakly measure the position of a trapped atom or the mirror confining the cavity [122]. Because it only weakly perturbs the state, weak measurement has many interesting applications in state tomography, process tomography, continuous error correction and feedback control, etc.

2.5 Photodetection and Homodyne Detection

In this section, let us look at a very sensitive and widely used quantum measurement, photodetection, and see how it can be used to monitor the system.

2.5.1 Direct Detection

In a direct photodetection, the system (an atom, cavity, etc) is coupled to a photon bath which is initially in a vacuum state, and we can continuously monitor photons coming into the bath. Let c be the system operator, and $b(t)$ be the photon bath annihilation operator satisfying the commutation relation [130]:

$$[b(t), b^\dagger(t')] = \delta(t - t'). \quad (2.47)$$

Let us define $dB_t = b(t)dt$, and it is easy to see that $[dB_t, dB_t^\dagger] = dt$. Let us assume the interaction between the system and the bath in the interval $[t, t + dt)$ takes the following form [130]:

$$U(t + dt, t) = \exp[cdB^\dagger - c^\dagger dB - iHdt], \quad (2.48)$$

where we are in the interaction picture of the bath and H is the system Hamiltonian. If the system-bath starts at $|\psi(t)\rangle |0\rangle$, after dt the state becomes

$$U(t + dt, t) |\psi(t)\rangle |0\rangle = |\psi\rangle [1 - dtc^\dagger c/2 - iHdt] |0\rangle + c |\psi(t)\rangle dB^\dagger |0\rangle. \quad (2.49)$$

It is clear that the first term represents zero photon and that the second term represents one photon. Therefore, the probability of detecting one photon in bath is

$$\|c |\psi(t)\rangle dB^\dagger |0\rangle\|^2 = \|c |\psi(t)\rangle\|^2 dt. \quad (2.50)$$

and system state jumps to $c |\psi\rangle$ after the detection.⁵ Therefore, direct detection can be described by a weak measurement with the following two operation elements:

$$M_0 = I - dt(iH + \frac{1}{2}c^\dagger c), \quad (2.51a)$$

⁵The bath state will also revert back to vacuum after detection as new field moves in to interact with the system.

$$M_1 = \sqrt{dt}c. \quad (2.51b)$$

The form of the measurement is similar to that in Eq. 2.28 in the qubit example.⁶ The conditioned SME,

$$d\rho(t) = \left\{ dN(t)\mathcal{G}[c] - dt\mathcal{H}\left[iH + \frac{1}{2}c^\dagger c\right] \right\} \rho(t), \quad (2.52)$$

and the unconditioned master equation,

$$d\rho(t) = -idt[H, \rho] + dt\mathcal{D}[c]\rho, \quad (2.53)$$

can be derived in an analogous way. The photocurrent is defined as the number of detections per unit time, ie.,

$$I(t) = dN(t)/dt, \quad (2.54)$$

and $E[I(t)] = \text{Tr}[\rho(t)c^\dagger c]$. In the case of a cavity, it just means the photon flux leaking out.

2.5.2 Homodyne Detection

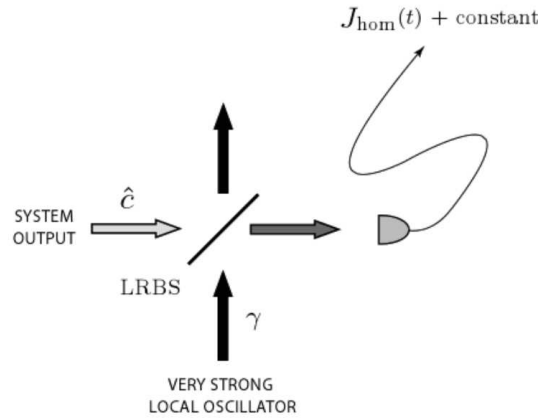


Figure 2.1: A scheme for simple homodyne detection. A low-reflectivity beam-splitter (LRBS) transmits almost all of the system output, and adds only a small amount of the local oscillator through reflection. Nevertheless, the local oscillator is so strong that this reflected field dominates the intensity at the single photoreceiver. This is a detector that does not resolve single photons but rather produces a photocurrent proportional to $J(t)$ plus a constant [130].

In many situations we would like to obtain quadrature measurement of a beam, which carries information about its phase. This is where a homodyne detection comes in. The way

⁶Here, we have the additional unitary evolution term.

we do it is to mix the signal beam with a strong reference beam (called a local oscillator) with the same frequency, and we measure the intensity of the output beam, as shown in Fig. 2.1. The mixing is done through a beam splitter. Just from classical analysis, we can conclude that to the first order only the component of the signal in-phase with the local oscillator will affect the intensity of the resulting beam [113]. By tuning the phase of the local oscillator, we can measure a desired quadrature of the signal. Let us see how everything works quantum mechanically.

Let γ be the complex amplitude of the local oscillator. The beamsplitter basically does the following transformation: $c \rightarrow c + \gamma$ [130]. Under such transformation, the measurement operators transform (from Eq. 2.51) to

$$M_0 = I - dt[iH + \frac{1}{2}(c\gamma^* - c^\dagger\gamma) + \frac{1}{2}(c^\dagger + \gamma^*)(c + \gamma)], \quad (2.55a)$$

$$M_1 = \sqrt{dt}(c + \gamma). \quad (2.55b)$$

It is easy to check that the unconditioned master equation is still given by Eq. 2.53 while the conditioned SME becomes

$$d\rho(t) = \left\{ dN(t)\mathcal{G}[c + \gamma] - dt\mathcal{H}[iH + \gamma c + \frac{1}{2}c^\dagger c] \right\} \rho(t). \quad (2.56)$$

dN is the indicator random variable for a photon detection during $[t, t + dt]$, which satisfies

$$E[dN(t)/dt] = \text{Tr}[(c^\dagger + \gamma^*)(c + \gamma)\rho(t)]. \quad (2.57)$$

Let us take γ to be real. $E[dN(t)/dt] = \text{Tr}[\gamma^2 + \gamma(c^\dagger + c) + c^\dagger c\rho(t)]$ and the homodyne detection measures the quadrature $x = c^\dagger + c$. In the large γ limit, the number of detection dN can be written as⁷ [130]

$$dN(t) = \gamma^2[1 + \langle x \rangle / \gamma]dt + \gamma dW. \quad (2.58)$$

The homodyne detection current is defined as [130]

$$J(t) \equiv \lim_{\gamma \rightarrow \infty} \frac{dN - \gamma^2 dt}{\gamma dt} = \langle x \rangle(t) + \xi(t), \quad (2.59)$$

⁸where $\xi = dW/dt$ is the Wiener noise. The expectation value of the current is exactly the expectation value of the system quadrature operator we would like measure. The SME becomes (Eq. 4.72 in [130])

$$d\rho(t) = -i[H, \rho(t)]dt + \mathcal{D}[c]\rho(t)dt + \mathcal{H}[c]\rho(t)dW. \quad (2.60)$$

⁷Here the time step dt is taken to be on the order of $\gamma^{-3/2}$ so the number of detection events is large while the system change is small during the interval.

⁸ $\gamma^2 dt$ represents the number of detection events coming from the local oscillator in the absence of the system output. γdt is a normalizing factor.

We immediately see that the unconditioned master equation is still Eq. 2.53 unchanged (because dW averages to zero).

The above mentioned scheme is called a simple homodyne detection. In practice, a balanced homodyne detection is more common where we use a 50 : 50 beam splitter and mix the signal from both output ports to produce a homodyne current [130]. It has many practical advantages over a simple homodyne detection. Theoretically, the dynamics in the large γ limit, i.e. Eq. 2.59 and 2.60, is the same for both.

Homodyne detection is widely used for measuring Cavity-QED systems (in both radio and optical frequency). Many experimental demonstrations of quantum error correction and feedback control have homodyne detection as an integral component [130].

Chapter 3

Hierarchical Equations of Motion

3.1 Formalism

Understanding open quantum system evolution is crucial for quantum information processing. The difficult part in quantum dissipation theory is how to trace over the bath degrees of freedom, which are usually infinitely many. The Lindblad master equation derived in Sec. 2.3 can approximately describe dissipative systems in its regime of validity. Let us summarize the assumptions made. First, the system-bath coupling is weak, so we can expand the exact equation of motion perturbatively. Second, the bath correlation time is much shorter than the system relaxation time, so the evolution is Markovian. Lastly, the intrinsic time scale of the system (which is the inverse of the typical level spacing) is much larger than the relaxation time of the system, so the evolution can be regarded as time-homogeneous under the rotating wave approximation. These assumptions are violated in many real quantum systems, and a more general treatment is desired. It turns out that the system evolution can be described exactly in terms of an influence phase functional under a Gaussian bath assumption [92]. However, the expression with the influence phase functional is not time local. We are going to write the system evolution in terms of a set of hierarchical equations of motion (HEoM). HEoM can be solved effectively because they are time-local differential equations and can be truncated at certain order. Let us see how it works in detail.

We break the system-bath Hamiltonian into three parts as usual:

$$H = H_S + H_B + H_I. \quad (3.1)$$

Let us assume the bath is a collection of harmonic oscillators, e.g.,

$$H_B = \sum_k \omega_k b_k^\dagger b_k. \quad (3.2)$$

We also assume the interaction takes the form

$$H_I = VB, \quad (3.3)$$

where V is a Hermitian system operator and B is Hermitian bath operator that is a linear combination of creation and annihilation operators, e.g.,

$$B = \sum_k (g_k b_k + g_k^* b_k^\dagger). \quad (3.4)$$

The product form for H_I is assumed for simplicity of illustration. The derivation of the HEoM can be generalized straightforwardly if the interaction takes the completely general form

$$H_I = \sum_{i=1}^N V_i B_i. \quad (3.5)$$

The spectral density of the interaction, which describes how the interaction strength varies with frequency, is defined as

$$J(\omega) = \sum_k |g_k|^2 \delta(\omega - \omega_k). \quad (3.6)$$

Let us further assume the system-bath starts out in the product state

$$\rho(0) = \rho_S(0) \otimes \rho_B, \quad (3.7)$$

where ρ_B is the thermal state

$$\rho_B = \frac{\exp(-\beta H_B)}{\text{Tr}_B[\exp(-\beta H_B)]}. \quad (3.8)$$

We define the average over thermal bath operation $\langle \dots \rangle_B$ as $\langle O \rangle_B = \text{Tr}_B(O \rho_B)$. Then the evolution of the system density operator can be written as [124]

$$\rho_S(t) = \left\langle T_+ \exp \left(\int_0^t \mathcal{L}(s) ds \right) \right\rangle_B \rho_S(0), \quad (3.9)$$

where T_+ means chronological time ordering, and \mathcal{L} is the Liouvillian (see Chap. 2) for the total Hamiltonian H .

Let us work in the interaction picture defined by $H_S + H_B$. We define the following Gaussian property of a bath for its annihilation operators a_k according to Wick's theorem [92]:

$$\langle T_+ a_k(t_{2n}) a_k(t_{2n}) \dots a_k(t_1) \rangle_B = \sum_{a.p.p} \prod_{i,j} \langle T_+ a_k(t_i) a_k(t_j) \rangle_B, \quad (3.10)$$

where *a.p.p* means all ways of picking pairs among $2n$ operators [52]. It basically states that the n -point correlation functions are completely determined by the 2-point correlation functions, and that odd-point correlation functions are all zero. The Gaussian property is guaranteed for a bath that consists of harmonic oscillators, as assumed in Eq. 3.2. This

property is also valid in more general classes of bath, as long as the interaction consists of a large number of weak interactions [112]. We use C to denote the 2-point correlation function (with no time ordering):

$$C(t_2 - t_1) \equiv \langle B(t_2)B(t_1) \rangle_B. \quad (3.11)$$

Let C^R and C^I be its real and imaginary components. It is easy to check that

$$C^R = \frac{1}{2} \langle \{B(t_2), B(t_1)\} \rangle_B, \quad (3.12)$$

$$C^I = -\frac{i}{2} \langle [B(t_2), B(t_1)]_B \rangle, \quad (3.13)$$

where $\{, \}$ is the anticommutator and $[,]$ is the commutator. C can be expressed in terms of the spectral density as [110]

$$C(t) = \frac{1}{\pi} \int_0^\infty d\omega J(\omega) \frac{\exp(-i\omega t)}{1 - \exp(-\beta\omega)}. \quad (3.14)$$

The expansion of Eq. 3.9 contains bath operators of all orders. However, the trace of the bath of all these operators can be eliminated in favor of $C(t)$ because of the Gaussian property. Therefore, (with somewhat lengthy algebra) Eq. 3.9 can be expressed as

$$\rho_S(t) = T_+ \exp(i\Delta[V])\rho_S(0), \quad (3.15)$$

with the influence phase functional $\Delta[V]$ given by [68]

$$\Delta[V] = i \int_0^t dt_2 \int_0^{t_2} dt_1 V(t_2)^\times [C^R(t_2 - t_1)V(t_1)^\times + iC^I(t_2 - t_1)V(t_1)^\circ], \quad (3.16)$$

where $A^\times B \equiv [A, B]$ and $A^\circ B \equiv \{A, B\}$. $\Delta[V]$ completely captures the influence of the bath on the system and hence the name.

A standard way to solve Eq. 3.15 is to use a path integral representation involving the Feynman-Vernon influence functional [29]. However, evaluation of this remains challenging for most practical systems. In this section, we are going to decode instead it into a set of time-local differential equations, HEoM.

First, we need to cast $C(t)$ (in the $t > 0$ region) into a sum of exponential functions of t :

$$C(t) = \sum_m c_m \exp(\nu'_m t). \quad (3.17)$$

The following Drude spectral density is often used in chemical physics and biophysics:

$$J(\omega) = \frac{2\lambda\gamma\omega}{\omega^2 + \gamma^2}. \quad (3.18)$$

Using Eq. 3.14, the corresponding correlation function expansion, Eq. 3.17, is seen to be an infinite series with

$$\nu'_0 = \gamma, \quad (3.19a)$$

$$\nu'_{m \geq 1} = 2\pi m / \beta, \quad (3.19b)$$

$$c_0 = \gamma \lambda (\cot(\beta\gamma/2) - i), \quad (3.19c)$$

$$c_{m \geq 1} = \frac{4\lambda\gamma\nu'_m}{\beta(\nu'^2_m - \gamma^2)}. \quad (3.19d)$$

The series can be truncated at some order $m = M$, with the value of m required to achieve converged result increasing as temperature decreases. In the high temperature regime where $\beta\gamma < 1$, keeping one or two terms in the series typically suffices [52]. For most chemical and biological systems, the high temperature condition is satisfied.

For many quantum computing devices, e.g. cavity-QED, the coupling spectral density takes the Lorentz shape [68]:

$$J(\omega) = \frac{\lambda\gamma}{\pi[(\omega - \Omega)^2 + \gamma^2]}. \quad (3.20)$$

In the regime where $\gamma \ll \Omega$ and $\beta\Omega \gg 1$, the corresponding correlation function can be approximated as a single exponential with¹

$$\nu'_0 = -(\gamma + i\Omega), \quad (3.21a)$$

$$c_0 = \lambda. \quad (3.21b)$$

For a more general spectrum, we can use a few exponential functions to fit the correlation function.

With the correlation function cast into the sum-of-exponentials form, the system evolution (in the Schrodinger picture) can be cast into the following form [68]:

$$\rho_S(t) = U(t)T_+ \exp \left[\int_0^t dt_2 \int_0^{t_2} dt_1 \Phi(t_2) \sum_{k=1}^K e^{-\nu_k(t_2-t_1)} \Theta_k(t_1) \right] \rho_S(0)U^\dagger(t), \quad (3.22)$$

where $U(t) = \exp[-i(H_S + H_B)t]$. $\Phi(t) = -iV(t)^\times$ and $\Theta(t)$ is a linear combination of $V(t)^\times$ and $V(t)^\circ$. (K is at most twice as large as M .) Let us introduce the following hierarchy of auxiliary density operators indexed by the non-negative integer vector $\mathbf{n} = \{n_1, n_2, \dots, n_K\}$:

$$\begin{aligned} \rho_{\mathbf{n}}(t) = & U(t)T_+ \left\{ \prod_{k=1}^K \left[\int_0^t d\tau e^{-\nu_k(t-\tau)} \Theta_k(\tau) \right]^{n_k} \right. \\ & \times \exp \left[\int_0^t dt_2 \int_0^{t_2} dt_1 \Phi(t_2) \sum_{k=1}^K e^{-\nu_k(t_2-t_1)} \Theta_k(t_1) \right] \Big\} \rho_S(0)U^\dagger(t), \end{aligned} \quad (3.23)$$

¹In Ref. [68] it is treated as an exact expression, but it is really just an approximation with a regime of validity, even at zero temperature.

and one can see that ρ_S is the same as ρ_0 . Let $\boldsymbol{\nu} = \{\nu_1, \nu_2, \dots, \nu_K\}$ and \mathbf{e}_k be the K -vector such that $(\mathbf{e}_k)_i = \delta_{ki}$. By directly differentiating Eq. 3.23, we can obtain the following K -level hierarchy equations that relate the time derivative of each auxiliary operator to some other auxiliary operators:

$$\dot{\rho}_{\mathbf{n}}(t) = -(iH_S^\times + \mathbf{n} \cdot \boldsymbol{\nu})\rho_{\mathbf{n}}(t) + \Phi(t) \sum_{k=1}^K \rho_{\mathbf{n}+\mathbf{e}_k}(t) + \sum_{k=1}^K n_k \Theta_k(t) \rho_{\mathbf{n}-\mathbf{e}_k}(t). \quad (3.24)$$

²It holds for $\mathbf{n} = \mathbf{0}$ and all auxiliary \mathbf{n} . The initial conditions of the operators are

$$\rho_{\mathbf{n}}(0) = \begin{cases} \rho_S(0) & \text{for } \mathbf{n} = \mathbf{0}, \\ 0 & \text{otherwise.} \end{cases} \quad (3.25)$$

If the system-bath interaction takes the form of sum of N terms as in Eq. 3.5, the HEoM would be NK -level.

The HEoM can be terminated at a finite stage for computation. Typically $\rho_{\mathbf{n}}$ with $\mathbf{n} \cdot \boldsymbol{\nu} \gg \omega_S$ can be ignored [52], where ω_S is the characteristic intrinsic frequency of the system.

We see that the HEoM method relaxes most of the assumptions that are necessary for deriving the Lindblad master equation (mentioned at the beginning of the section). The HEoM usually provide an effective way to solve for the dynamics of an open quantum system as long as the bath is Gaussian.

In the next section, we will look at an example where the bath correlation function takes the form described by Eq. 3.21. For this particular case, the two-level ($K = 2$) HEoM can be written as [68]

$$\dot{\rho}_{\mathbf{n}}(t) = -(iH_S^\times + \mathbf{n} \cdot \boldsymbol{\nu})\rho_{\mathbf{n}}(t) - i \sum_{k=1}^2 V^\times \rho_{\mathbf{n}+\mathbf{e}_k}(t) - \frac{i\lambda}{2} \sum_{k=1}^2 n_k [V^\times + (-1)^k V^\circ] \rho_{\mathbf{n}-\mathbf{e}_k}(t). \quad (3.26)$$

3.2 Qubit Relaxation

In this section we will look at a qubit system coupled to a Gaussian bath. The dephasing (T_2) effect can be modeled by setting $V = \sigma_z$ and the relaxation (T_1) effect can be modeled by setting $V = \sigma_x$. We will study relaxation as an example. Let the qubit frequency and the bath correlation function be given by Eq. 3.20, namely,

$$C(t_2 - t_1) = \lambda \exp[-(\gamma + i\Omega)(t_2 - t_1)], \quad (3.27)$$

²The RHS of Eq. 3.24 is obtained by taking the time derivative of the RHS of Eq. 3.23 with the product rule and substituting in the auxiliary operators. (Keep in mind that the time derivative operator and the time ordering operator commute.) $-iH_S^\times \rho_{\mathbf{n}}(t)$ comes from the terms involving $\frac{d}{dt}U$ and $\frac{d}{dt}U^\dagger$; $-\mathbf{n} \cdot \boldsymbol{\nu} \rho_{\mathbf{n}}(t)$ and $+\sum_{k=1}^K n_k \Theta_k(t) \rho_{\mathbf{n}-\mathbf{e}_k}(t)$ comes from the term involving $\frac{d}{dt} \prod_{k=1}^K \left[\int_0^t d\tau e^{-\nu_k(t-\tau)} \Theta_k(\tau) \right]^{n_k}$; $+\Phi(t) \sum_{k=1}^K \rho_{\mathbf{n}+\mathbf{e}_k}(t)$ comes from the term involving $\frac{d}{dt} \exp \left[\int_0^t dt_2 \int_0^{t_2} dt_1 \Phi(t_2) \sum_{k=1}^K e^{-\nu_k(t_2-t_1)} \Theta_k(t_1) \right]$.

which approximately corresponds to the Lorentz coupling spectrum at near zero temperature. The correlation time is characterized by γ^{-1} .

3.2.1 The natural relaxation

We first like to see what the Lindblad master equation tells us about the process. The Fourier transform of the correlation function, $\Gamma(\omega)$,³ turns out to be the same as the Lorentz spectral density, Eq. 3.20, up to a constant factor of $2/\pi$:

$$\Gamma(\omega) = \frac{2\lambda\gamma}{(\omega - \Omega)^2 + \gamma^2}. \quad (3.28)$$

According to Eq. 2.24, the Lindblad master equation can be written as⁴

$$\dot{\rho} = \Gamma(\omega_0)\mathcal{D}[\sigma^-]\rho + \Gamma(-\omega_0)\mathcal{D}[\sigma^+]\rho. \quad (3.29)$$

This equation can be solved analytically in a straightforward way. The steady state (in terms of the Bloch vector components x_{ss} , y_{ss} , and z_{ss}) is given by

$$x_{ss} = 0, \quad (3.30a)$$

$$y_{ss} = 0, \quad (3.30b)$$

$$z_{ss} = -\frac{\Gamma(\omega_0) - \Gamma(-\omega_0)}{\Gamma(\omega_0) + \Gamma(-\omega_0)}, \quad (3.30c)$$

which is very close to the ground state as we expect. The evolution of the Bloch vector components x , y , z is given by

$$x(t) = \exp(-t/(2\tau_R))x(t), \quad (3.31a)$$

$$y(t) = \exp(-t/(2\tau_R))y(t), \quad (3.31b)$$

$$z(t) = z_{ss} + (z(0) - z_{ss})\exp(-t/\tau_R), \quad (3.31c)$$

where the system relaxation time $\tau_R = [\Gamma(\omega_0) + \Gamma(-\omega_0)]^{-1}$. Dotted red lines in Fig 3.1 show the relaxation process of the qubit if the initial state is set to be maximally mixed ($x = y = z = 0$). The monotonic nature of the relaxation is consistent with the Markovian dynamics assumed in the Lindblad model.

Let us solve the same relaxation process with the HEOm, Eq. 3.26. We will keep the auxiliary density matrices to the second order, namely $\rho_{\mathbf{n}}$ with $n_1 + n_2 \leq 2$. Solid blue lines in Fig 3.1 show the solution to this second order HEOm, which should be treated as almost

³It is the same as $\gamma(\omega)$ in Sec. 2.3.

⁴ $\Gamma(-\omega_0)$ represents a very weak unphysical excitation process. It comes from the error in approximating the correlation function with the single exponential. We use the same correlation function for both the Lindblad master equation and the HEOm, so it does not jeopardize our comparison anyway.

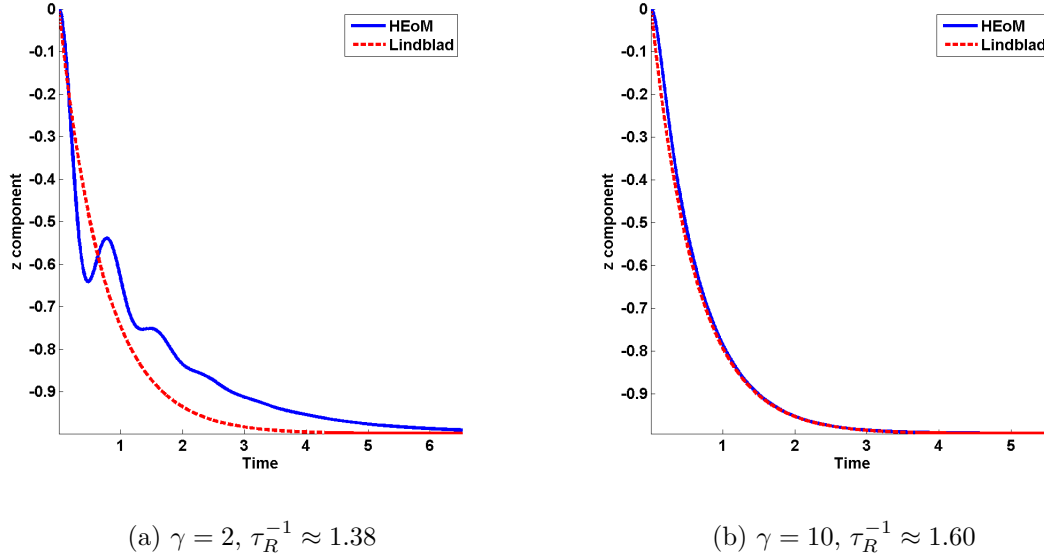


Figure 3.1: This figure compares the relaxation process of a qubit predicted by the Lindblad master equation (Eq. 3.29) and the 2nd order HEoM (Eq. 3.26). $x = y = 0$ is satisfied throughout the process, and only the evolution of z is shown. $\omega_0 = 95$, $\Omega = 100$, $\lambda = 10$, and two different values of bath correlation rate γ are chosen.

exact. We can see the relaxation process is not a monotonic decay, there can now exist oscillatory behavior which is characteristic of non-Markovianity.

From the comparison, we see that when the bath correlation time and the system relaxation time are comparable ($\gamma^{-1} \sim \tau_R$), the Lindblad master equation has a significant deviation from the HEoM (Eq. 3.1a). Specifically, it fails to demonstrate the oscillatory behavior in the decay. However, when the bath correlation time becomes much shorter than the system relaxation time ($\gamma^{-1} \ll \tau_R$), the Lindblad master equation becomes reasonably accurate (Eq. 3.1b).

3.2.2 The controlled relaxation

In this subsection, we are going to see how an open loop unitary control operation might aid the relaxation process. We will solve everything using HEoM.

Let us look at control for an example in the non-Markovian regime where the qubit frequency ($\omega_0 = 90$) is further away from the peak ($\Omega = 100$) of the coupling spectrum than in Fig. 3.1a. We take $\gamma = 2$ as before. Fig. 3.2 demonstrates different control schemes for such a highly non-markovian parameter regime. The natural relaxation process (shown in the solid black line) is significantly slower than in Fig. 3.1a because the qubit and the bath are far off-resonant. In order to speed up the process, we try a simple control Hamiltonian $H_c = 5\sigma_z$ that brings the effective qubit frequency to the same value as Ω . The system

evolution under this on-resonant control is shown in the dotted blue line. Although this is much faster than the natural relaxation, there is a strong oscillatory behavior where the system “bounces back” from close to the ground state. In order to alleviate the problem, let us try an improved strategy. We initially apply H_c to create a resonance; when the qubit is most close to the ground state, we turn off H_c to bring qubit out of resonance. This strategy is shown in the dashed red line in the plot. We see that the oscillatory effect is indeed reduced and the qubit has better relaxation behavior under this control strategy.

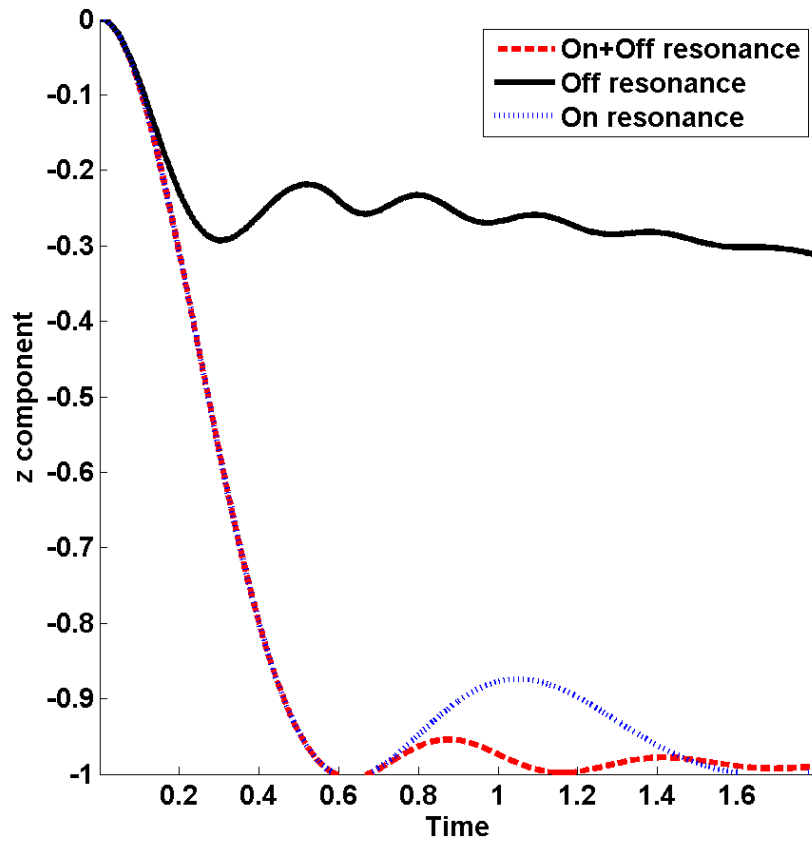


Figure 3.2: This figure shows the relaxation process of the qubit subject to different control protocols. For ‘Off resonance’ protocol, there is no control Hamiltonian added. For ‘On resonance’ protocol, $H_c = 5\sigma_z$ is on all the way through. For ‘On+Off’ resonance protocol, H_c is on until $t \approx 0.6$. Parameters chosen are $\omega_0 = 90$, $\Omega = 100$, $\lambda = 10$, $\gamma = 2$.

3.2.3 Conclusion

In this section, we saw that the Lindblad master equation fails to capture certain important feature of an open quantum system outside its regime of validity. The Born-Markov approximation breaks down if the bath is non-Markovian, the system-bath coupling is strong, or the control Hamiltonian is strong. However, the HEoM are typically still valid and provide a useful tool to tackle such open quantum systems. We also see for qubit relaxation that we can use coherent control to battle the non-markovian effects by solving HEoMs.

3.3 Unravelling HEoMs

⁵ In the previous chapter, we see that a deterministic master equation can be unraveled into a stochastic master equation, with the former describing the average behavior of the latter. When the stochastic master equation is equivalent to a stochastic Schrodinger equation, it can be advantageous to solve the deterministic master equation by numerically averaging out the solutions to the stochastic Schrodinger equation. The reason is that for a Hilbert space of dimension N , a density operator is of size $N \times N$ while a pure state vector is of size N . Although we need to solve many runs of a stochastic differential equation(SDE) to obtain a good average, this unravelling technique is useful when N is large enough, particularly if we do not even have a RAM of size $N \times N$.

We would like to apply the same trick to unravel the HEoM. Please be aware that this is merely a mathematical treatment, where individual trajectories have no physical meaning. In order to show the possibility of such an unravelling, we consider a system coupled to a bath via $H_I = V \otimes B$. We assume the bath is at a high temperature T and the coupling has the Drude spectral density (Eq. 3.18). Let us write the first order HEOM that involves the density operator ρ and a single auxiliary density operator σ [52]:

$$\begin{aligned} \frac{d\rho}{dt} &= -i[H, \rho] + i[V, \sigma] \\ \frac{d\sigma}{dt} &= -i[H, \sigma] - \gamma\sigma + i2\lambda T[V, \rho] + \lambda\gamma\{V, \rho\} \end{aligned} \quad (3.32a)$$

We write $\rho(t) = E[|\psi(t)\rangle\langle\bar{\psi}(t)| + h.c.]$, $\sigma(t) = E[|\phi(t)\rangle\langle\bar{\phi}(t)| + h.c.]$. Eq. 3.32 can then be unraveled into the following linear SDE for $|\psi(t)\rangle$, $|\bar{\psi}(t)\rangle$, $|\phi(t)\rangle$, and $|\bar{\phi}(t)\rangle$:

$$d|\psi\rangle = -iH|\psi\rangle dt + iV|\phi\rangle dt + |\phi\rangle dW_{\bar{\psi}}, \quad (3.33a)$$

$$d|\bar{\psi}\rangle = -iH|\bar{\psi}\rangle dt + |\bar{\phi}\rangle dW_{\psi} + iV|\bar{\phi}\rangle dW_{\bar{\psi}}, \quad (3.33b)$$

$$d|\phi\rangle = -(iH + \gamma/2)|\phi\rangle dt + (i2\lambda T + \lambda\gamma)V|\psi\rangle dW_{\phi} + |\psi\rangle dW_{\bar{\phi}}, \quad (3.33c)$$

$$d|\bar{\phi}\rangle = -(iH + \gamma/2)|\bar{\phi}\rangle dt + |\bar{\psi}\rangle dW_{\phi} + (i2\lambda T + \lambda\gamma)V|\bar{\psi}\rangle dW_{\bar{\phi}}, \quad (3.33d)$$

⁵This section is my joint work with Alireza Shabani.

where dW_ψ and $dW_{\bar{\psi}}$ are two independent Wiener processes, as also dW_ϕ and $dW_{\bar{\phi}}$.⁶

It turns out that almost all trajectories of the above SDE are unbounded, although their true average will be our desired solution to the HEoM. The symmetric random walk in 1D would be an analogy: almost all trajectories diverge, but the average stays constant at the initial position. Therefore, the number of trajectories we need to average over increases with time and this unravelling approach is not feasible once time gets large.

The way to alleviate the problem is to make the trajectories as bounded as possible. Please notice that the trace of ρ is conserved in the HEoM. It corresponds to the quantity

$$T_\rho = \langle \bar{\psi} | \psi \rangle + \langle \psi | \bar{\psi} \rangle \quad (3.34)$$

in the SDE, which can be made conserved for individual trajectories if we apply the trick mentioned in Ref. [33]. The idea behind this trick will be explained soon. Let

$$R_\psi = \frac{1}{2}(\langle \bar{\phi} | \psi \rangle + \langle \bar{\psi} | iV | \phi \rangle) + h.c., \quad (3.35a)$$

$$R_{\bar{\psi}} = \frac{1}{2}(\langle \phi | \bar{\psi} \rangle + \langle \psi | iV | \bar{\phi} \rangle) + h.c., \quad (3.35b)$$

and

$$R_\phi = 0, \quad (3.36a)$$

$$R_{\bar{\phi}} = 0. \quad (3.36b)$$

The non-linear but ρ -trace-preserving unraveling can be written as:

$$d|\psi\rangle = -iH|\psi\rangle dt - |\psi\rangle dB_\rho + iV|\phi\rangle(R_\psi dt + dW_\psi) + |\phi\rangle(R_{\bar{\psi}} dt + dW_{\bar{\psi}}), \quad (3.37a)$$

$$d|\bar{\psi}\rangle = -iH|\bar{\psi}\rangle dt - |\bar{\psi}\rangle dB_\rho + |\bar{\phi}\rangle(R_\psi dt + dW_\psi) + iV|\bar{\phi}\rangle(R_{\bar{\psi}} dt + dW_{\bar{\psi}}), \quad (3.37b)$$

$$d|\phi\rangle = -(iH + \gamma/2)|\phi\rangle dt - |\phi\rangle dB_\sigma + (i2\lambda T + \lambda\gamma)V|\psi\rangle(R_\phi dt + dW_\phi)/C \\ + C|\psi\rangle(R_{\bar{\phi}} dt + dW_{\bar{\phi}}), \quad (3.37c)$$

$$d|\bar{\phi}\rangle = -(iH + \gamma/2)|\bar{\phi}\rangle dt - |\bar{\phi}\rangle dB_\sigma + C|\bar{\psi}\rangle(R_\phi dt + dW_\phi) \\ + (i2\lambda T + \lambda\gamma)V|\bar{\psi}\rangle(R_{\bar{\phi}} dt + dW_{\bar{\phi}})/C, \quad (3.37d)$$

where

$$dB_\rho = R_\psi dW_\psi + R_{\bar{\psi}} dW_{\bar{\psi}} + \frac{1}{2}(R_\psi^2 + R_{\bar{\psi}}^2)dt, \quad (3.38)$$

$$dB_\sigma = R_\phi dW_\phi + R_{\bar{\phi}} dW_{\bar{\phi}} + \frac{1}{2}(R_\phi^2 + R_{\bar{\phi}}^2)dt, \quad (3.39)$$

and C can be an arbitrary real constant⁷.

⁶It is ok to have correlations between other pairs, (eg, dW_ψ and dW_ϕ) although we will treat all the Wiener processes to be independent of each other in the simulation.

⁷We set $C = \sqrt{|i2\lambda T + \lambda\gamma|}$ for best convergence in simulation.

Eq. 3.37 unravels the original HEoM for arbitrary deterministic functions R_ψ , $R_{\bar{\psi}}$, R_ϕ , and $R_{\bar{\phi}}$. However, only Eq. 3.35 ensures that ρ is normalized for each unravelling. We set the other two to zero in Eq. 3.36 just to make the unravelling simpler; σ can not be normalized as its trace is not conserved in the original HEoM.

The idea behind the above normalized unravelling is the following. For the original unnormalized unravelling, Eq. 3.33, we have

$$dT_\rho = 2R_\psi dW_\psi + 2R_{\bar{\psi}} dW_{\bar{\psi}}. \quad (3.40)$$

For each trajectory, we can apply the following transformation

$$\psi(t) \rightarrow \psi(t)/\sqrt{T_\rho(t)}, \quad (3.41a)$$

$$\bar{\psi}(t) \rightarrow \bar{\psi}(t)/\sqrt{T_\rho(t)}, \quad (3.41b)$$

to ψ and $\bar{\psi}$, so that T_ρ (after the transformation) is held constant at 1. However, in order to keep the trajectory's contribution to the average the same, we need to increase its probability by T_ρ to compensate for the fact that Eq. 3.41 scales it down by T_ρ . As explained in Ref. [33], this probability renormalization can be achieved by making the following transformation to the Wiener noise increments [33]:

$$dW_\psi \rightarrow 2R_\psi dt + dW_\psi, \quad (3.42a)$$

$$dW_{\bar{\psi}} \rightarrow 2R_{\bar{\psi}} dt + dW_{\bar{\psi}}. \quad (3.42b)$$

Eq. 3.37 is then obtained by applying the above transformations (and similar ones associated with ϕ and $\bar{\phi}$) to Eq. 3.33.

We will use qubit dephasing as an example. Let $H = \frac{1}{2}\omega_0\sigma_z$ and $V = \sigma_z$. Fig. 3.3b shows, for a general initial state, the dynamics solved from HEoM directly (dotted line) vs. the average of the normalized unraveling (solid line). (Shown are the Bloch vector components in the rotating frame, X , Y , and Z , where Z should stay constant for this dephasing dynamics.) One can spot a systematic deviation between them. I tried both the Euler-Maruyama method and the 4th order Runge-Kutta method for the unraveled SDE, and I chose different time steps, but the same deviation is present. Therefore, this unravelling approach does not seem to work as we desire.

I speculate that the reason why the simulation average deviates from the true average may be the following. ϕ and $\bar{\phi}$ can go unbounded for some trajectories, although the probabilities are exponentially suppressed by the γ terms; ψ and $\bar{\psi}$ can go unbounded too, even if T_ρ is fixed at 1 (which is manifested by the spikes in Fig. 3.3a). Such unbounded trajectories have non-negligible contribution to the true average. However, they are not adequately sampled in the simulation because their probabilities are perhaps exponentially low. As a result, the stochastic trajectory average is erroneous.

One may also use Poisson processes instead of Wiener processes in an unravelling. A Poisson process $dN(t)$ that happens in $[t, t + dt)$ takes either 0 or 1 and has expectation

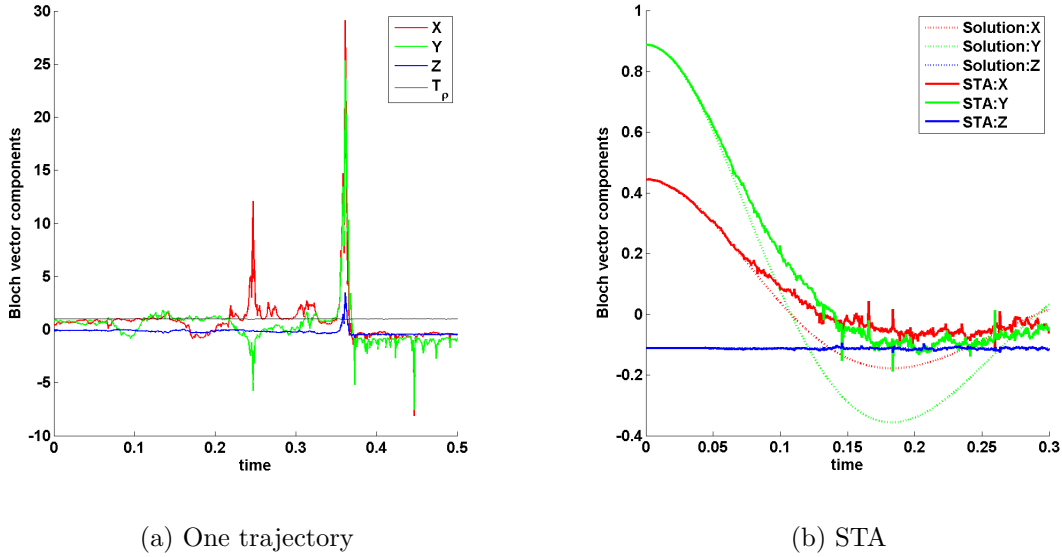


Figure 3.3: The Bloch vector components X , Y , Z (in the rotating frame defined by ω_0) associated with (a) one typical unravelling (b) the HEoM, Eq. 3.32 with $V = \sigma_z$, solution (labeled with 'Solution') vs. stochastic trajectory average (labeled with 'STA') of the unravellings. The average is done with 20000 simulation runs. Parameters chosen are $T = 40$, $\lambda = 1$, $\gamma = 10$. (ω_0 is irrelevant here.)

value dt . In order to get a Poisson type of unravelling, we just need to replace dW with $dN - dt$ in the above unravelings. However, the Poisson SDE run into an even worse convergence issue because there seems to be no way to even normalize the trajectories using the trace-preserving technique.

So far I am not able to come up with an unravelling scheme that is feasible to implement, but it is worthy of future research.

Chapter 4

PI Control

Quantum states are fragile and decoherence poses a main challenge to implementing a quantum computer. One way to battle decoherence is to control the quantum system based on the past measurement record, also known as feedback control or closed-loop control. The simplest feedback method would be tuning the feedback strength so that it is always proportional to the instantaneous measurement current [127]. This method is referenced to nowadays as Wiseman-Milburn feedback [130], or (direct) proportional feedback. Wiseman-Milburn feedback strategies can give us significant improvement over no feedback at all, but they are usually far from optimal. The most effective feedback method would be to perform a real-time estimation of the current quantum state and to adjust the control accordingly. However, real-time estimation is usually extremely difficult to implement experimentally, due to the complicated dependence of the state estimator on the measurement records. In this section, we will introduce a quantum control strategy that is based on integrations of past measurement currents, called integral feedback. It is well-known in classical control theory [109] but has not been extensively studied for quantum control.¹ Integral feedback is a trade-off between performance and feasibility. It might perform better than proportional feedback because it takes into account measurement records in the past in addition to those at present, and a simple integral is also much easier to implement experimentally than a complicated state estimator. A control strategy that combines the proportional feedback and integral feedback is called PI control. In this section, we will formulate the quantum theory of PI control and give two examples comparing the relative performance of proportional and integral feedback.

4.1 Formalism

In this section, we will develop the formalism for a quantum system under continuous-in-time measurement (e.g., homodyne detection) and PI feedback control. Let ρ be the state

¹The idea of integral feedback on quantum systems was mentioned in Ref. [98] where a low-pass filter of the measurement signal over a small time window was used to condition the feedback.

of the system, H be the intrinsic Hamiltonian, c be the measurement operator,² η be the measurement efficiency. We will set $\hbar = 1$ in this section.

The measurement conditioned dynamics of the system without control can be described by the following stochastic master equation which we studied in Sec. 2.60:

$$[d\rho(t)]_{nf} = -i[H, \rho(t)] + \mathcal{D}[c]\rho(t)dt + \sqrt{\eta}\mathcal{H}[c]\rho(t)dW(t), \quad (4.1)$$

where dW is a Wiener increment satisfying $dW^2 = dt$. The superoperators in this equation are defined as $\mathcal{D}[A]\rho \equiv A\rho A^\dagger - \frac{1}{2}(A^\dagger A\rho + \rho A^\dagger A)$ and $\mathcal{H}[A]\rho \equiv A\rho + \rho A^\dagger - \text{Tr}[(A + A^\dagger)\rho]\rho$. The measurement current can be written as [130]

$$J(t) = \langle c + c^\dagger \rangle(t) + \xi(t)/\sqrt{\eta}, \quad (4.2)$$

where $\xi(t) = dW/dt$ is the Wiener noise. A PI feedback superoperator \mathcal{K} , which may be dependent on both the instantaneous current and a time integral of the current, generates the following additional dynamics:

$$[\dot{\rho}(t)]_{fb} = \mathcal{K}\rho \equiv J(t - \tau_P)(-i)[F_P, \rho(t)] + J_{int}(t)(-i)[F_I, \rho(t)], \quad (4.3)$$

where F_P and F_I are the control operators associated with the proportional and integral feedback respectively. The time delay τ_P is physically present in a real feedback system and sometimes can also be utilized to improve the feedback performance (see subsection 4.3.3). The integral J_{int} of the current can be expressed as:

$$J_{int}(t) = \int_0^{\tau_I} J(t-s)w(t,s)ds, \quad (4.4)$$

where $w(t,s)$ is a filter representing how heavily we weigh the photocurrent at time s ago towards the feedback and τ_I is the filter integration time. We will normalize $w(t,s)$ by $\int_0^{\tau_I} w(t,s)ds = 1$.³ Therefore, $J_{int}(t)$ behaves just like a smoothed-out version of $J(t)$ with the same integrated strength. A simple filter could have a constant $w(t,s)$. However, a $w(t,s)$ that decays in s would likely perform better, because it puts lesser weight on current further in the past. Please note that the filter does not reduce the amount of noise injected into the system, it merely injects each piece of noise over a period of time instead of in a single shot.

The following derivation of system dynamics will be similar to that for the Wiseman-Milburn feedback in Ref. [130]. Let us define the anti-commutator superoperator F^\times as $F^\times \rho \equiv [F, \rho]$. When we evolve the system for time dt , we need to add the feedback incremental superoperator $\exp(\mathcal{K}dt)$ to the evolution given by Eq. 4.1, namely,

$$\rho(t+dt) = \exp(\mathcal{K}dt) \times \{1 - iH^\times dt + \mathcal{D}[c]dt + \sqrt{\eta}\mathcal{H}[c]dW(t)\}\rho(t), \quad (4.5)$$

²The measurement strength is encoded in this operator.

³For time-homogeneous filters, $w(t,s)$ is independent of t .

and

$$\mathcal{K}dt = [\langle c + c^\dagger \rangle (t - \tau_P)dt + dW(t - \tau_P)/\sqrt{\eta}](-i)F_P^\times + J_{int}(-i)F_I^\times dt. \quad (4.6)$$

The dW term in $\mathcal{K}dt$ is of $O(\sqrt{dt})$ and needs to be expanded to the second power in $\exp(\mathcal{K}dt)$. The other two terms in $\mathcal{K}dt$ are of $O(dt)$ and need to be expanded to the first power only. In particular, J_{int} , as seen from Eq. 4.4, is basically a weighted sum of $N = \tau_I/dt$ independent Wiener increments dW_i ($i=1, 2, \dots, N$). Hence, $(J_{int})^2$, which consists of a sum of N terms, $(dW_i)^2$, that are of $O(dt)$, is regular (i.e., $O(dt^0)$). Therefore, J_{int} is regular as well and $J_{int}dt \sim O(dt)$. We note that the time step dt should be much smaller than the filter integration time τ_I here.⁴

In principle, the proportional feedback can be treated as the integral feedback with a delta function filter, namely, the first term in Eq. 4.3 can be absorbed in the second term by adding the filter $w(t, s) = \delta(s - \tau_P)$. We can choose a rectangle with (very narrow) width τ_I and height $1/\tau_I$ to approximate this delta function. Practically, $1/\tau_I$ represents the bandwidth of the proportional feedback loop. However, the time step needs to be much smaller than this τ_I when we simulate the resulting SME, which can be very inefficient. Therefore, we still treat the proportional term separately when deriving the SME.

The result for the total conditioned evolution of the system is then

$$\begin{aligned} \rho(t + dt) = & \{1 + [\langle c + c^\dagger \rangle (t - \tau_P)dt + dW(t - \tau_P)/\sqrt{\eta}](-i)F_P^\times + \mathcal{D}[F_P]dt/\eta + J_{int}(-i)F_I^\times dt\} \\ & \times \{1 - iH^\times dt + \mathcal{D}[c]dt + \sqrt{\eta}\mathcal{H}[c]dW(t)\}\rho(t). \end{aligned} \quad (4.7)$$

For $\tau_P > 0$, the conditioned SME becomes:

$$\begin{aligned} d\rho(t) = & dt \left\{ -i[H, \rho(t)] + \mathcal{D}[c]\rho(t) + \langle c + c^\dagger \rangle (t - \tau_P)(-i)[F_P, \rho(t)] + \mathcal{D}[F_P]\rho(t)/\eta \right. \\ & \left. + J_{int}(-i)[F_I, \rho(t)] \right\} + dW(t - \tau_P)(-i)[F_P, \rho(t)]/\sqrt{\eta} + \sqrt{\eta}dW(t)\mathcal{H}(c)\rho(t). \end{aligned} \quad (4.8)$$

For $\tau_P = 0$, the conditioned SME becomes:⁵

$$\begin{aligned} d\rho(t) = & dt \left\{ -i[H, \rho(t)] + \mathcal{D}[c]\rho(t) - i[F_P, c\rho(t) + \rho(t)c^\dagger] + \mathcal{D}[F_P]\rho(t)/\eta + J_{int}(-i)[F_I, \rho(t)] \right\} \\ & + dW(t)\mathcal{H}[\sqrt{\eta}c - iF_P/\sqrt{\eta}]\rho(t). \end{aligned} \quad (4.9)$$

One can see that unlike proportional feedback, the integral feedback just adds a regular unitary evolution term to the system dynamics. In this paper, we will always simulate the above integral stochastic differential equations(SDE) with what we call a generalized Euler-Maruyama method. For the usual Euler-Maruyama [59] method, we generate a Wiener noise increment $dW(t)$ for each time step $[t, t+dt]$ and update the state according to the stochastic differential equation. For our generalized Euler-Maruyama method, we always keep a record of the noise up to time $\tau = \max(\tau_I, \tau_P)$ in the past, i.e., $dW(t)$, $dW(t - dt)$, ... $dW(t - \tau)$. Therefore, $dW(t - \tau_P)$ is accessible and $J_{int}(t)$ can be calculated at each time t , and the state can be updated according to the SDE as usual.

⁴More precisely, dt should be much smaller than the duration in s over which $\omega(t, s)$ varies significantly.

⁵The system evolution described by Eq. 4.8 converges smoothly to that described by Eq. 4.9 as τ_P approaches zero.

4.2 Two-qubit Entanglement Generation

In this section, we explore the use of PI control to generate an entangled two-qubit state with a local Hamiltonian and non-local measurement. We will continue to set $\hbar = 1$ in this section. Let us use T_i to denote the triplet state with total spin i , where $i = -1, 0, 1$. Namely, $T_{-1} = |00\rangle$, $T_0 = |01\rangle + |10\rangle$, and $T_1 = |11\rangle$. Our goal is to stabilize the state to T_0 .

We assume the two qubits are subject to a simple intrinsic Hamiltonian $h_1\sigma_{z1} + h_2\sigma_{z2}$ where h_1 and h_2 are constants and decoherence is negligible. If we work in the rotating frame defined by the intrinsic Hamiltonian, the system Hamiltonian vanishes, i.e., $H = 0$. We assume the measurement operator c is given by

$$c = \sqrt{2k}L_z, \quad (4.10)$$

where $L_z = (\sigma_{z1} + \sigma_{z2})/2$ and k is the measurement strength. We also assume that a $L_x = (\sigma_{x1} + \sigma_{x2})/2$ feedback Hamiltonian with controllable strength (see below) is at our disposal. If the initial state is in the triplet subspace, the subsequent evolution will stay within the subspace under such measurement and feedback. Without loss of generality, we set $k = 1$.

The measurement current (as given by Eq. 4.2) serves as a good error signal. At the target state T_0 , the expectation value of the current is 0; at T_1 and T_{-1} the expectation is positive and negative respectively.

Let us write $F_P = f_P L_x$ and $F_I = f_I L_x$, where f_P and f_I are the proportional and integral feedback strength. Since applying a L_x rotation can bring $T_{\pm 1}$ closer to T_0 , the feedback Hamiltonian can partially correct the error. Therefore, we expect the feedback as given by Eq. 4.3 will be helpful. For the integral feedback, we would like to choose the following filter that takes the exponential decay form:

$$J_{int}(t) = \frac{1}{\tau_I} \int_{-\infty}^t J(s) \exp(-(t-s)/\tau_I) ds. \quad (4.11)$$

To judge the quality of the feedback strategies, we will look at the steady state populations of the three triplet states as well as the concurrence. Given a density operator ρ , the population of a pure target state $|\psi\rangle$ is defined as $\langle\psi|\rho|\psi\rangle$. Concurrence, an excellent measure of entanglement, is defined for a mixed state of two qubits as

$$\mathcal{C}(\rho) \equiv \max(0, \lambda_1 - \lambda_2 - \lambda_3 - \lambda_4) \quad (4.12)$$

in which $\lambda_1, \dots, \lambda_4$ are the eigenvalues, in decreasing order, of the Hermitian matrix

$$R = \sqrt{\sqrt{\rho} \tilde{\rho} \sqrt{\rho}} \quad (4.13)$$

with

$$\tilde{\rho} = (\sigma_y \otimes \sigma_y) \rho^* (\sigma_y \otimes \sigma_y) \quad (4.14)$$

the spin flipped state of ρ [43, 131].

The steady state is independent of a wide variety of initial states we explored. Fig. 4.1a and Fig. 4.1c show the unconditioned evolution of the system under proportional and integral feedback respectively. The measurement efficiency and feedback strength are the same for both strategies ($f_I = f_P = 0.2$, $\eta = 0.4$). We chose $\tau_P = 0$ for the proportional feedback and a near-optimal integration time $\tau_I = 3$ for the integral feedback. The unconditioned density matrices for the proportional feedback are calculated with the (unconditioned) Wiseman-Milburn equation (Eq. 4.9 without the J_{int} term and the dW term), and those for the integral feedback are calculated with Eq. 4.9 by averaging over 2000 runs. One can see that the concurrence and the three triplet populations reach steady state for both feedback strategies, but the integral feedback is able to produce a higher steady state concurrence than the proportional feedback. (Please be aware that all triplet populations vary wildly between 0 and 1 for individual trajectories under both feedback strategies.)

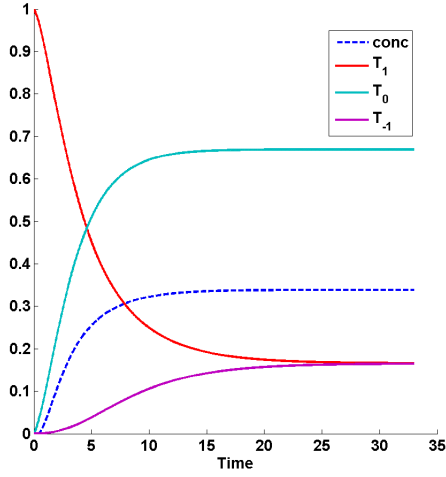
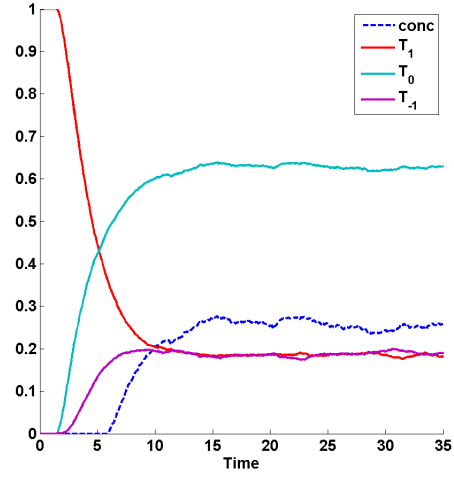
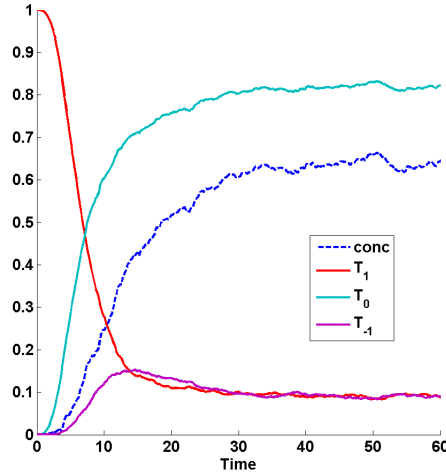
To further illustrate the trade-off between short and long integration time, Fig. 4.2 plots the steady state concurrence vs. filter integration time τ_I for the integral control. ($\tau_I = 0$ should be understood as the proportional feedback with no delay.) For any feedback strength, there is a peak in concurrence that corresponds to a non-zero optimal filter integration time.⁶ For a fixed filter integration time, the steady state concurrence decreases with the feedback strength f_I , and it converges to some upper limit as the strength goes to zero.⁷ For the proportional feedback (at $\tau_I = 0$ as noted above), this limiting concurrence is about 0.36, but Fig. 4.2 shows that integral feedback can exceed this limit by a wide margin. We also simulated proportional feedback strategies with delay (e.g., Fig. 4.1b), and these also perform worse than the best integral feedback strategies.⁸ Therefore, our two-qubit entanglement generation problem is a convincing example that shows feedback control with a filtered current is effective in generating entanglement and outperforms the conventional proportional feedback strategy.

The reason why integrating the current helps can be understood as follows. The feedback is ineffective in correcting any incremental measurement noise, because the generator of the measurement noise, $\mathcal{H}[L_z]$, is not proportional to the generator of the feedback, L_x^\times . Indeed, when the state is close to T_0 , measurement in an infinitesimal time tends to slightly mix the state with more $T_{\pm 1}$ population, but we are better off not performing any L_x rotation at all at the feedback step, since the T_0 population still dominates. However, if measurement drives the state all the way to be T_{-1} or T_1 dominant after some finite time, we can perform a finite L_x feedback rotation and bring the state much closer to T_0 . Therefore, the feedback is effective in correcting accumulated measurement noise instead of incremental measurement noise, and integrating the measurement record will be very useful.

⁶The peak for $f_i = 0.1$ is out of the range of Fig. 4.2.

⁷The system takes longer and longer to reach steady state as the feedback strength f_I goes to zero, however.

⁸The performance of proportional feedback decreases with the delay time τ_P as we expect.

(a) Proportional control with $\tau_P = 0$ (b) Proportional control with $\tau_P = 1.5$ 

(c) Integral control

Figure 4.1: The average evolution of a two-qubit system under feedback control. (a) shows the proportional feedback with $\tau_P = 0$ and $f_P = 0.2$ calculated according to the unconditional Wiseman-Milburn equation; (b) shows the proportional feedback with $\tau_P = 1.5$ and $f_P = 0.2$ calculated by averaging over trajectories simulated with Eq. 4.8; (c) shows the integral feedback with $\tau_I = 3$ and $f_I = 0.2$ calculated by averaging over trajectories simulated with Eq. 4.9. $\eta = 0.4$ is chosen for both. The initial state is taken to be the unentangled state T_1 .

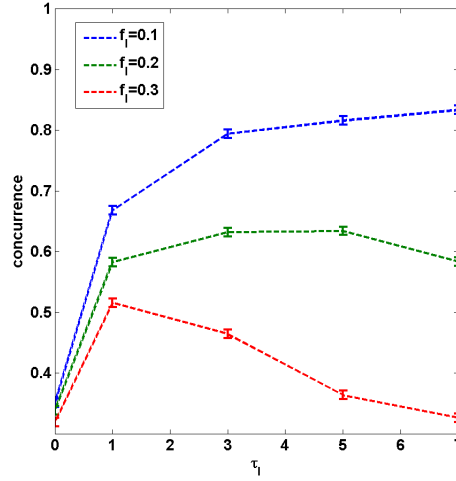


Figure 4.2: The steady state concurrence vs. integration time for the integral control. The relation is plotted with $\eta = 0.4$ and three different f_I values.

4.3 Harmonic Oscillator State Stabilization

The feedback control on a harmonic oscillator has many practical interests, both classical and quantum mechanical. Manipulating trapped cold ions or atoms would be an example. The quantum case was considered in Refs. [24, 47, 25]. We investigate here if adding a filter in the control loop enhances control or not. The system is damping at rate γ due to some coupling to a bath of zero temperature (spontaneous emission in the case of a trapped atom). We apply a continuous measurement of the position x with strength k and efficiency η . The master equation can be written as [25]

$$d\rho = -\frac{i}{\hbar}[H_0, \rho]dt + 2\gamma\mathcal{D}[a]\rho + 2k\mathcal{D}[x]\rho dt + \sqrt{2\eta k}\mathcal{H}[x]\rho dW, \quad (4.15)$$

where $\omega = 2\pi/T$ is the angular frequency and a is the annihilation operator. $H_0 = m\omega x^2/2 + p^2/(2m)$. The measurement current j is given by⁹ [24]

$$j(t) = 4\eta k\langle x \rangle(t) + \sqrt{2\eta k}\xi(t). \quad (4.16)$$

Based on the outcomes of the measurement, we apply a feedback linear in x and p . Let us write the proportional feedback operator as

$$F_P = \alpha x + \beta p. \quad (4.17)$$

⁹This expression is the same as Eq. 4.2 except an overall constant.

α and β are proportional feedback strength. This proportional feedback is the same as in Ref. [24] except we will also consider a delay τ_P in the feedback loop. Let us add the following regular feedback to the above proportional feedback

$$H_f = f_x(t)p - f_p(t)x, \quad (4.18)$$

where $f_x(t)$ and $f_p(t)$ are the strength for x and p control respectively, which include any dependence on integrals of the measurement records.

If we start with a Gaussian state, the state will remain Gaussian under such measurement and feedback [53]. A Gaussian state is completely determined by its first moments ($\langle x \rangle, \langle p \rangle$) and second moments ($V_x \equiv \langle (x - \langle x \rangle)^2 \rangle$, $V_p \equiv \langle (p - \langle p \rangle)^2 \rangle$, $C_{xp} \equiv \frac{1}{2} \langle xp + px \rangle - \langle x \rangle \langle p \rangle$). It has been shown that the evolution of second moments are independent of the feedback and that they will reach steady state [24]. The steady state values can be expressed as follows in the $\gamma \ll k$ limit [24]:

$$V_x = \left(\frac{\hbar}{\sqrt{2\eta}m\omega} \right) \frac{1}{\sqrt{\xi + 1}}, \quad (4.19a)$$

$$V_p = \left(\frac{\hbar m\omega}{\sqrt{2\eta}} \right) \frac{\xi}{\sqrt{\xi + 1}}, \quad (4.19b)$$

$$C_{xp} = \left(\frac{\hbar}{2\sqrt{\eta}} \right) \frac{\sqrt{\xi - 1}}{\sqrt{\xi + 1}}, \quad (4.19c)$$

where

$$\xi = \sqrt{1 + \frac{4}{\eta r^2}}, \quad r = \frac{m\omega^2}{2\hbar\eta k}. \quad (4.20)$$

One can see that the state becomes more squeezed in the x quadrature than in the p quadrature as a result of the x measurement.

The evolution of the first moments is given by [24]

$$d\langle x \rangle(t) = (\langle p \rangle/m)dt + d\tilde{x}(t), \quad (4.21a)$$

$$d\langle p \rangle(t) = -m\omega^2 \langle x \rangle dt + d\tilde{p}(t). \quad (4.21b)$$

where

$$d\tilde{x}(t) = -\gamma \langle x \rangle(t)dt + f_x(t)dt + 4\eta k \beta \langle x \rangle(t - \tau_P)dt + \sqrt{2\eta k} (2V_x dW(t) + \beta dW(t - \tau_P)), \quad (4.22a)$$

$$d\tilde{p}(t) = -\gamma \langle p \rangle(t)dt + f_p(t)dt - 4\eta k \alpha \langle x \rangle(t - \tau_P)dt + \sqrt{2\eta k} (2C_{xp} dW(t) - \alpha dW(t - \tau_P)). \quad (4.22b)$$

The above results are obtained with the Heisenberg equations of motion associated with the SME (Eq. 4.9) under the aforementioned measurement and control. For simplicity, we will

consider the dynamics when the second moments have reached steady state, as given by Eq. 4.19.

For better simulation behavior, we make a change of variables and write the two quadratures operators x and p in the lab frame in terms of X and P in the rotating frame, namely,

$$x = X(t) \cos(\omega t) + P(t) \sin(\omega t) / (m\omega), \quad (4.23a)$$

$$p = -m\omega X(t) \sin(\omega t) + P(t) \cos(\omega t). \quad (4.23b)$$

The expectation values of the quadrature operators obey the same transformation rules above, obviously. Then the dynamics in the lab frame, Eq. 4.21, can be translated to the following dynamics in the rotating frame¹⁰:

$$d\langle X \rangle(t) = d\tilde{x}(t) \cos(\omega t) - d\tilde{p}(t) \sin(\omega t) / (m\omega), \quad (4.24a)$$

$$d\langle P \rangle(t) = m\omega d\tilde{x}(t) \sin(\omega t) + d\tilde{p}(t) \cos(\omega t). \quad (4.24b)$$

where the right hand side can also be written in terms of $\langle X \rangle$ and $\langle P \rangle$ using Eq. 4.22 and 4.23.

In the following subsections, we will explore the state stabilization problem where the goal is to center the state at an arbitrary point ($\langle X \rangle = X_g$, $\langle P \rangle = P_g$) in the rotating frame. Also, $(x_g(t), p_g(t))$ denotes the same target state in the lab frame, which is again related to (X_g, P_g) with the transformation Eq. 4.23. The cooling problem can be viewed as a special case where $X_g = 0$ and $P_g = 0$.

4.3.1 x and p Control

In the case where both x and p control are feasible, any state can be driven exponentially close to the target state $(x_g(t), p_g(t))$ by setting $\alpha = 2C_{xp}$, $\beta = -2V_x$, $f_x(t) = (\gamma + 8\eta k V_x)x_g(t)$, and $f_p(t) = \gamma p_g(t) + 8\eta k C_{xp}x_g(t)$.¹¹ Then Eq. 4.22 becomes

$$d\tilde{x}(t) = -\gamma(\langle x \rangle(t) - x_g(t))dt - 8\eta k V_x(\langle x \rangle(t) - x_g(t))dt, \quad (4.25a)$$

$$d\tilde{p}(t) = -\gamma(\langle p \rangle(t) - p_g(t))dt - 8\eta k C_{xp}(\langle x \rangle(t) - x_g(t))dt. \quad (4.25b)$$

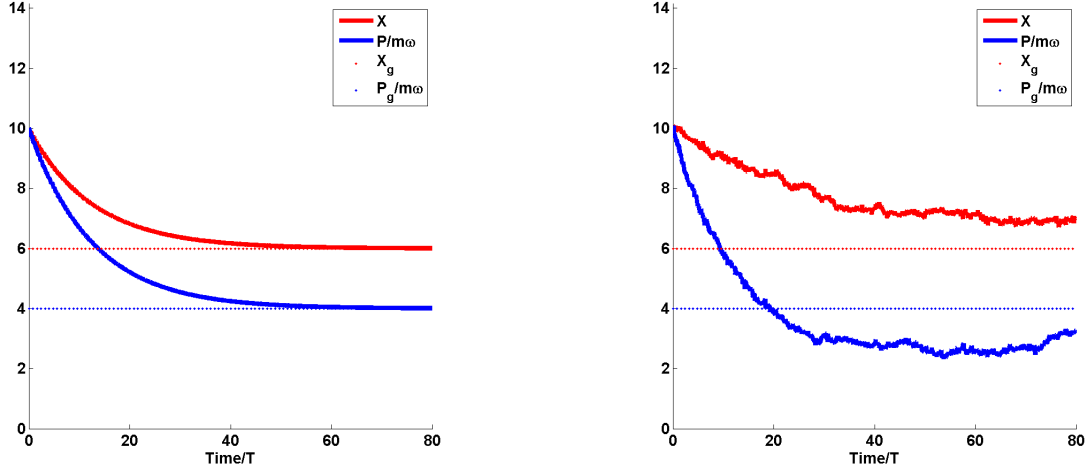
The idea behind this setting is two-fold. First, the measurement noise (dW terms) is completely canceled out by feedback and the evolution is deterministic.¹² Second, the relaxation terms, which are proportional to the error signals $\langle x \rangle - x_g$ and $\langle p \rangle - p_g$, correct any deviation from the target state. (The term $\langle x \rangle - x_g$ in the dynamics for $p_g(t)$ does not act as a feedback, but it does not do much harm either. It will eventually decay to zero

¹⁰Ref. [25] did the frame change using the rotating wave approximation, but we are doing it rigorously.

¹¹Our settings generalize those in Ref. [24], which studied the cooling problem, i.e., $X_g = 0$ and $P_g = 0$.

¹²Similar noise cancelling behavior is also observed in feedback control of a single qubit [64].

when the target state is approached.) Therefore, any initial state can be perfectly stabilized as illustrated in Fig. 4.3a. We note that $f_x(t)$ and $f_p(t)$ here are basically (time dependent) offsets that are independent of the measurement current, so the scheme described above is essentially a current proportional feedback.



(a) Proportional control

(b) Integral control

Figure 4.3: The evolution of X and P quadratures in the rotating frame of an oscillator subject to an x and p control Hamiltonian. The parameters of the oscillator are as follows: $m = 1$, $\omega = 1$, $\eta = 0.1$, $k = 0.02$, $\gamma = 0$. The initial state is set to $X_g = 10$, $P_g/(m\omega) = 10$ and the target state is set to $X_g = 6$, $P_g/(m\omega) = 4$. For the integral control, the characteristic time τ_I for the exponential filter is set to $0.04T$. The chosen feedback strengths are very optimal.

Now let us see what happens when we use integral control. We would like to average out the currents up to about time τ_I in the past, so we process the current with the following exponential filter:

$$I(t) = \frac{1}{\tau_I} \int_{-\infty}^t j(s) \exp(-(t-s)/\tau_I) ds. \quad (4.26)$$

A very good choice of feedback making use of such an integral filter is the following:

$$\begin{aligned} f_x(t) &\approx -2V_x(I(t) - 4\eta k x_g(t)) + \gamma x_g(t), \\ f_p(t) &\approx -2C_{xp}(I(t) - 4\eta k x_g(t)) + \gamma p_g(t). \end{aligned} \quad (4.27)$$

The idea behind the choice of coefficients in this current integration feedback is similar to the case of the current proportional feedback above, namely noise cancellation and correction based on the error signals. A typical evolution, from the same initial states as in the proportional case, is shown in Fig. 4.3b. One can spot a systematic deviation from the target

state; this deviation can be removed by adjusting the coefficients in front of x_g and p_g in the feedback. However, there is nevertheless randomness in the evolution because we are not able to cancel out the noise precisely in the integral feedback.¹³ Hence, the actual state will fluctuate around the target state, preventing perfect state stabilization. We will see in the next subsection that another good choice of filter is the sinusoidal filter, but we nevertheless get this stochastic behavior for virtually all filters. We therefore conclude that if we have access to both x and p control, integrating the current will only make things worse.

4.3.2 x Control only under Rotating Wave Approximation

Let us now explore what will happen if we only have access to a control Hamiltonian that is proportional to x . It physically represents a force, which is most realistic. Because the strength f_p for the control Hamiltonian x enters the dynamics in $d\langle p \rangle$ as indicated in Eq. 4.22, getting a good estimate of $\langle p \rangle$ would be very helpful. However, the measurement current only directly reveals information about x . In order to proceed, we will integrate the current with sin and cos filters to get good estimate of the two quadratures $\langle X \rangle$ and $\langle P \rangle$ of the oscillator in the rotating frame, as Doherty suggests [25]:

$$J_X(t) = \sqrt{\hbar/(m\omega k\eta)} \int_{t-\tau'_I}^t j(s) \cos(\omega s) ds / \tau'_I, \quad (4.28a)$$

$$J_P(t) = \sqrt{\hbar m\omega/(k\eta)} \int_{t-\tau'_I}^t j(s) \sin(\omega s) ds / \tau'_I, \quad (4.28b)$$

where τ'_I should be chosen as an integer multiple of $T/2$, especially when it is small.

Let us also write the feedback strength $f_p(t)$ in terms of two lab frame quantities $f_X(t)$ and $f_P(t)$

$$f_p(t) = -2m\omega f_X(t) \sin(\omega t) + 2f_P(t) \cos(\omega t). \quad (4.29)$$

In order to come up with a simple dynamical equation, let us apply the rotating wave approximation [25], which only discerns dynamics on a scale larger than one period of oscillation. This approximation is valid when $k \ll m\omega^2/\hbar$, and f_X together with f_P are slowly varying. In this picture, the effective measurement strength is $K = \hbar k/(m\omega)$, and the above two quadrature currents can be written as [25]

$$J_X(t) = 2\sqrt{\eta K} \langle X \rangle(t) + \sqrt{\hbar/(m\omega)} \xi_X, \quad (4.30a)$$

$$J_P(t) = 2\sqrt{\eta K} \langle P \rangle(t) + \sqrt{\hbar m\omega} \xi_P, \quad (4.30b)$$

where ξ_X and ξ_P are two independent Wiener noise processes.¹⁴ Also, under rotating wave approximation, the state evolution, Eq. 4.24, can be simply expressed as [25]

$$d\langle X \rangle(t) = -\gamma \langle X \rangle(t) dt + f_X(t) dt + 2\sqrt{\eta k} (V_x dW_X - C_{xp} dW_P / (m\omega)), \quad (4.31a)$$

¹³There is no precise noise cancellation in integral feedback because the measurement noise term dW is singular but the integral feedback term is regular, i.e., is $O(dt^0)$.

¹⁴They come from the two quadratures of the original Wiener noise in $j(t)$.

$$d\langle P \rangle(t) = -\gamma\langle P \rangle(t)dt + f_P(t)dt + 2\sqrt{\eta k}(m\omega V_x dW_P + C_{xp}dW_X), \quad (4.31b)$$

where f_X and f_P can be anything dependent on J_X and J_P as a result of the feedback. A sensible integral feedback with strength u_X and u_P and characteristic filter length τ_I can be written as

$$f_X(t) = \frac{u_X}{\tau_I} \int_{-\infty}^t J_X(s) \exp(-(t-s)/\tau_I) ds + \gamma X_g, \quad (4.32a)$$

$$f_P(t) = \frac{u_P}{\tau_I} \int_{-\infty}^t J_P(s) \exp(-(t-s)/\tau_I) ds + \gamma P_g. \quad (4.32b)$$

The proportional feedback can be understood as the $\tau_I \rightarrow 0$ limit as before. It can be simulated by directly setting $f_X = u_X J_X + \gamma X_g$ and $f_P = u_P J_P + \gamma X_g$. We note that physically τ_I needs to be at least on the order of a period for a valid rotating wave approximation, and a sinusoidal filter (which is an integration) needs to be applied anyway. However, it is still insightful to study mathematically this proportional feedback limit of the above rotating wave dynamics.

One can see that choosing $u_X = u_P = -2\sqrt{m\omega\eta k/\hbar}V_x$ results in a good cancellation of the measurement noise $V_x dW_X$ and $V_x dW_P$ from Eq. 4.31. Fig. 4.4 compares the behavior of a proportional and an integral control strategy with this strength. One can see the integral control protocol has much more fluctuation, although both reach the target state. (For the proportional control, there is a tiny amount of fluctuation due to the terms $C_{xp}dW_P$ and $C_{xp}dW_X$ in Eq. 4.31, but it is invisible to the eye in these plots because C_{xp} is very small.)

The quality of the feedback can be quantified by the control error, which we define as

$$e = \sqrt{E[m\omega(\langle X \rangle - X_g)^2 + (\langle P \rangle - P_g)^2/(m\omega)]/(2\hbar)} \quad (4.33)$$

in the long time limit (i.e., when e reaches a constant value). E means the expectation value, which can be well approximated by averaging over many runs of simulation.

Analysis of the dependence on filter integration time τ_I shows that in this situation, instead of having an optimal τ_I , the quality of the integral control decreases monotonically with τ_I . Fig. 4.5 plots the relation between longtime control error e and filter time τ_I for $k = 0.01$. (e scales as $\sqrt{\tau_I k}$ and is independent of η approximately.) The reason why the proportional feedback outperforms the integral one is again that the former is better at noise cancellation.

As we mentioned earlier, physically, integrals of the measurement record are needed to obtain J_X and J_P in all feedback control protocols in this subsection. However, an engineered true proportional feedback protocol with fixed delay can also stabilize the state to the target state very well, as we now show.

4.3.3 x Control only without Rotating Wave Approximation

Let us come back to the original dynamics, Eq. 4.21 and 4.22, without the rotating wave approximation. We assume the weak measurement condition, $k \ll m\omega^2/\hbar$, as usual. Under

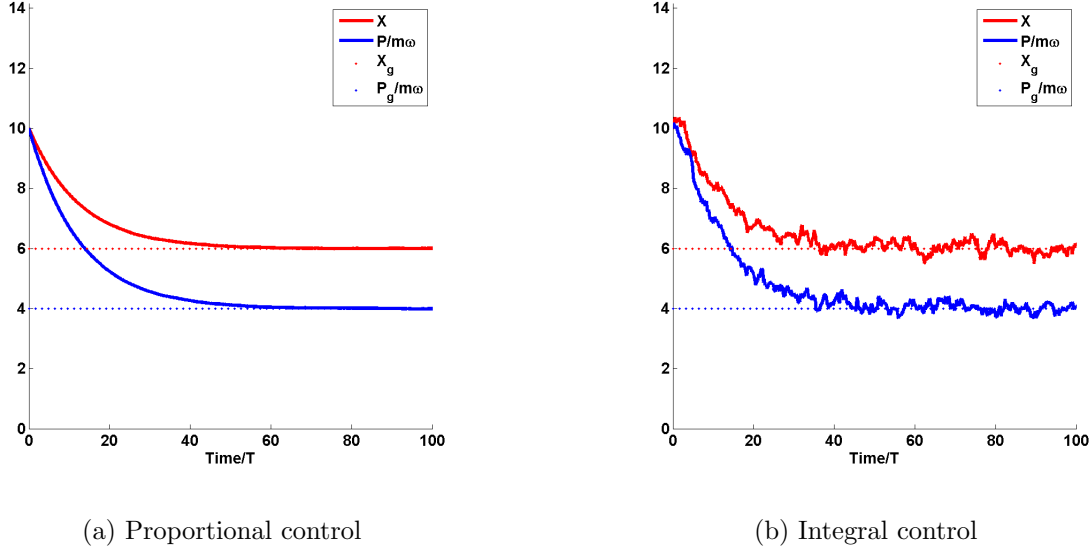


Figure 4.4: The evolution of X and P quadratures in the rotating frame of an oscillator subject to an x feedback Hamiltonian. The plots show typical simulation trajectories of Eq. 4.31, the dynamics under rotating wave approximation. The parameters of the oscillator are as follows: $\eta = 0.4$, $k = 0.01$, $\gamma = 0$. Feedback strengths are $u_X = u_P = -2\sqrt{m\omega\eta k/\hbar}V_x$. The initial state is set to $X_g = 10$, $P_g/(m\omega) = 10$ and the target state is set to $X_g = 6$, $P_g/(m\omega) = 4$. For the proportional control, $\tau_P = 0$, and for the integral control, $\tau_I = 4T$.

x control only, $\beta = 0$ and $f_x = 0$. One can see from Eq. 4.22 that the only non-noisy term involving α is $-4\eta k\alpha\langle x\rangle(t - \tau_P)dt$. However, this term is almost useless if $\tau_P = 0$, because x and p are roughly 90° out of phase with each other. Indeed, in the absence of γ , the trajectories do not have any converging behavior if we do proportional x feedback with zero delay. However, since $\langle x\rangle(t - T/4)$ is roughly proportional to $-\langle p\rangle/(m\omega)$, therefore, we would like to choose $\tau_P = T/4$ as the delay. We follow the line of logic in Subsec. 4.3.1 to tune the strength and offset of the feedback to achieve noise cancellation. We find that $\alpha \approx -2V_x m\omega$ with $f_p = (\gamma - 4\eta k\alpha/(m\omega))p_g$ gives near optimal behavior. The result is shown in Fig. 4.6a.

Next, let us compare this time delayed proportional feedback strategy with integral strategies. The sinusoidal filter mentioned in Sec. 4.3.2 can be reformulated in the following way without invoking the rotating wave approximation.

The quadrature currents J_X and J_P are obtained with integration time τ'_I , as defined in Eq. 4.28. Because J_X and J_P are proportional to X and P in the rotating frame,

$$J_p(t) = \sqrt{\frac{m\omega}{4k\eta\hbar}}(-m\omega J_X(t) \sin(\omega t) + J_P(t) \cos(\omega t)) \quad (4.34)$$

is a good estimator of the momentum $\langle p\rangle$ in the lab frame. We can feedback on this p

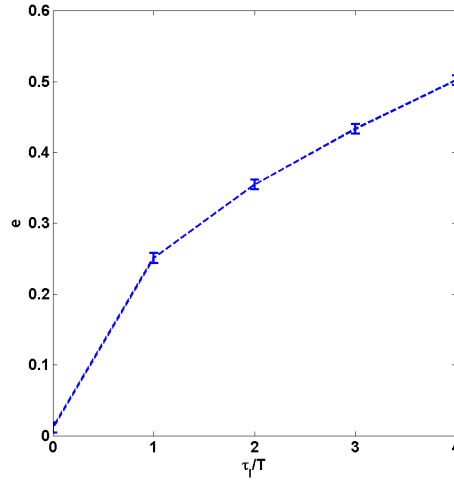


Figure 4.5: This plot shows the long time control error, e , vs. the integration time, τ_I . $\tau_I = 0$ means proportional control without delay. The parameters of the oscillator are as follows: $\eta = 0.4$, $k = 0.01$, $\gamma = 0$. Feedback strengths are $u_X = u_P = -2\sqrt{m\omega\eta k/\hbar}V_x$. e is calculated by averaging over 20000 runs.

estimator by setting

$$f_p \approx -8k\eta V_x(J_p - p_g) + \gamma p_g, \quad (4.35)$$

for best noise cancellation as usual.¹⁵ Also, we saw in Subsec. 4.3.2 that the long time error increases monotonically with the integration time, so for best behavior we would like to choose the smallest sensible τ'_I , i.e., $\tau'_I = T/2$.¹⁶ Fig. 4.6b shows the dynamics under integral feedback with the above near optimal parameter setting.

The performance of the proportional strategy with $\tau_P = T/4$ (Fig. 4.6a) is comparable to that of the integral feedback with $\tau'_I = T/2$ (Fig. 4.6b). It is hard to judge which is better from Fig. 4.6, and we need to calculate the long time error e . Fig. 4.7 shows that the integral feedback is slightly better than the proportional one for a wide range of η . (e scales as \sqrt{k} approximately for both strategies according to our simulation.) It can be understood intuitively as follows: the average delay of the information coming from the integral is $T/4$, the same as that from the proportional feedback. However, it is slightly advantageous to have the tempered version of the noise injected through the feedback instead of in a single shot, which gives the integral strategy the relative edge.

¹⁵This setting is equivalent to $u_X = u_P = -2\sqrt{m\omega\eta k/\hbar}V_x$ under rotating wave approximation mentioned in the last subsection.

¹⁶We also verified this monotonic increase in simulations without the rotating wave approximation.

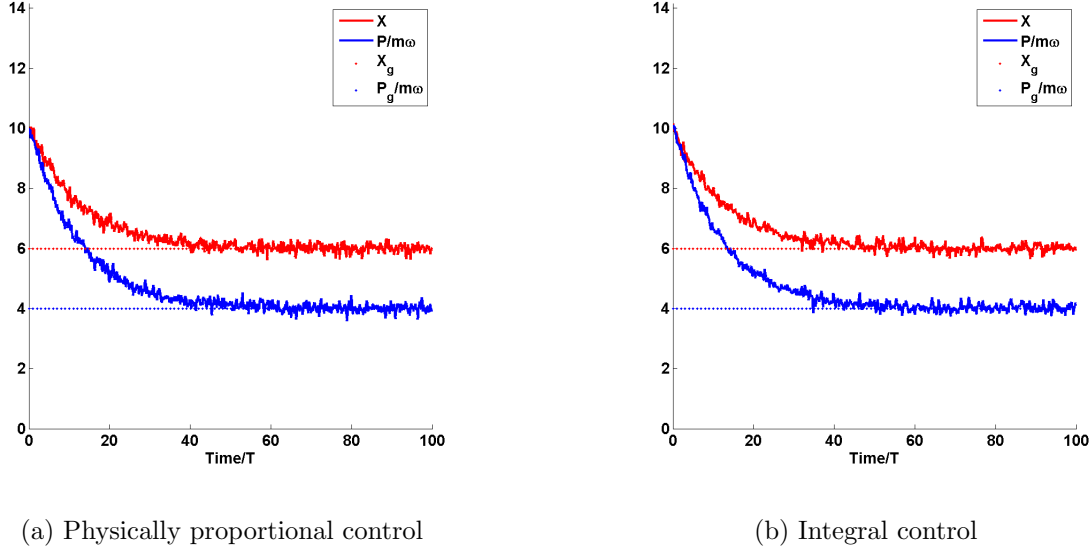


Figure 4.6: The evolution of X and P quadratures in the rotating frame of an oscillator subject to an x feedback Hamiltonian without invoking the rotating wave approximation. The parameters of the oscillator are as follows: $m = 1$, $\omega = 1$, $\eta = 0.4$, $k = 0.01$, $\gamma = 0$. The initial state is set to $X_g = 10$, $P_g/(m\omega) = 10$ and the target state is set to $X_g = 6$, $P_g/(m\omega) = 4$. For the physically proportional control, $\tau_P = T/4$, and for the integral control, $\tau_I' = T/2$. The chosen feedback strengths are very optimal for both.

4.3.4 Conclusion

We saw that for both control cases (x and p controls, or x control alone under the rotating wave approximation) in the harmonic oscillator state stabilization problem, filtering the current does not help. This behavior can be understood as follows. Our feedback can effectively correct any incremental measurement noise. As far as the first moments of a Gaussian state is concerned, the x measurement generates a translation (shift) in x and p . If we have control over both x and p , this translation can be well compensated by a feedback. Even if we only have an x control Hamiltonian, we effectively achieve control over both X and P in the rotating frame by adjusting the phase of the fast oscillating x control pulse. This manifests itself in the noise cancellation behavior that is common for the harmonic oscillator state stabilization. Therefore, we are better off correcting the noise right away rather than waiting for an integration to be done while noise accumulates.

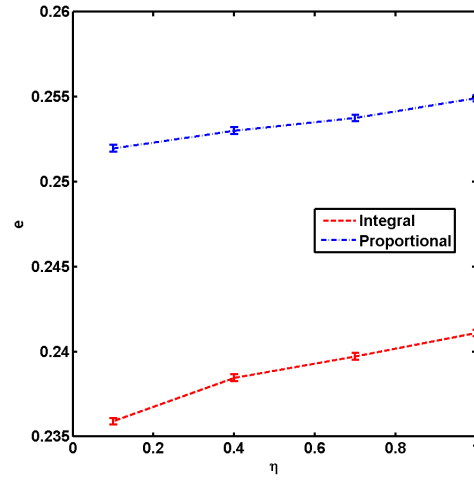


Figure 4.7: This plot shows the long time control error, e , vs. the measurement efficiency, η , for both the physically proportional feedback and the integral feedback without invoking the rotating wave approximation. The parameters of the oscillator are as follows: $m = 1$, $\omega = 1$, $k = 0.02$, $\gamma = 0$ and the target state is set to $X_g = 6$, $P_g/(m\omega) = 4$. For the physically proportional control, $\tau_P = T/4$, and for the integral control, $\tau_I = T/2$. The error e is calculated by averaging over 20000 runs.

Chapter 5

Optimal Control Protocol Analysis: an Example with Qubit Purification

¹Finding an optimal control strategy is always insightful for understanding the potential and limitations of quantum control. In optimality analysis, we usually relax many experimental constraints and study what is the best strategy theoretically. In this section, we present a simplified form of the verification theorem (Appendix 5.A) to examine the global optimality of a control protocol. As an example, we study the effect of experimental imperfections on the optimality of qubit purification protocols. Specifically, we find that the optimal control solutions in the presence of detector inefficiency and non-negligible decoherence can be significantly different from the known solutions to idealized dynamical models.

5.1 Introduction

Pure quantum states, states of systems with minimum classical uncertainty, are an ideal resource for many tasks in quantum information processing, including teleportation, quantum coding and error correction [80]. However, frequently the states of systems encountered in the laboratory are mixed quantum states that contain classical uncertainty about various aspects of the particular physical system of interest. Ordinarily this uncertainty can be removed, and the state *purified*, by an appropriate measurement or cooling procedure. Such purification is often a first, and critical, step in many quantum information processing, communication, and metrology protocols.

For many physical systems a measurement is properly treated as a finite timescale dynamical process as opposed to an instantaneous projective operation. In such systems, the measurement timescale (the time taken to complete a measurement and collect enough information to distinguish between the possible classical outcomes) is long enough that one can perform operations on the system during the measurement process. Such measurements are referred to as *weak measurements*. Some examples of quantum information systems that

¹The bulk of this chapter is adapted from Ref. [64].

can operate in regimes of weak measurement are quantum dots monitored by quantum point contacts [37], and cavity QED implementations in optics [45], or the solid-state [118].

In the case of purification implemented by a weak measurement, it is natural to ask whether it is possible to accelerate the purification process by performing operations during the measurement. Jacobs showed in Ref. [56, 57] that in an ideal scenario it is possible to increase the instantaneous rate of purification by adding feedback operations that are unitary rotations conditioned on the information collected by the weak measurement thus far. Specifically, Jacobs showed that in the case of a single qubit with perfect efficiency measurement, no decoherence, and arbitrarily strong feedback (what we will call the ideal case), a feedback strategy that always maintains a two-level quantum system (qubit) in an unbiased basis with respect to the constant measurement basis results a maximization of the instantaneous rate of purification. We shall refer to this protocol as the *unbiased measurement* protocol². Subsequently, Refs. [15, 104, 16] generalized this result and showed that in the ideal case it is possible to utilize feedback to increase the instantaneous rate of purification for arbitrary finite dimensional quantum systems. Wiseman and Ralph [128] have noted that it is useful to separate two different goals in the task of quantum state purification: the first goal, which we refer to as **max purity**, is that of maximizing the *average purity* of the system at a *given time*, while the second goal, which we refer to as **min time**, is that of minimizing the *average time* taken to achieve a *given purity*. These authors show that Jacobs' unbiased measurement strategy (which consequently maximizes the instantaneous rate of purification) is advantageous for the **max purity** goal, while a *diagonal measurement* strategy, which measures in the diagonal basis of the qubit state (and requires no feedback), is better for the **min time** goal. In fact, Wiseman and Bouten [129] later proved that in the ideal case the unbiased measurement strategy is the optimal one for purifying qubits with the **max purity** goal and that the diagonal measurement strategy is optimal for purifying qubits with the **min time** goal. This highlights another reason why quantum state purification is an important problem in quantum control theory. It is one of very few problems in this domain where questions of optimality can be constructively addressed. In contrast to this situation for the state purification problem, the optimality of most quantum feedback protocols cannot be assessed in a constructive manner.

All the above works address the problem of quantum state purification in the ideal case where the measurements are of unit efficiency (i.e., where the measurement-induced state disturbance is equally compensated by a gain in information about the state [126]) and the feedback action is arbitrarily fast. Both idealizing assumptions must typically be relaxed in realistic systems. In Ref. [39], Griffith *et al.* relax the arbitrarily fast feedback assumption and consider the performance of both the unbiased measurement and diagonal measurement protocols for purifying the state of a superconducting Cooper pair box qubit. More recently, Combes and Wiseman [14] have analyzed the impact of a wider array of imperfections on the unbiased measurement protocol for purification, including finite strength feedback, time delay in the feedback loop, calibration errors, measurement inefficiency, and decoherence.

²It is implicit in the name that this protocol requires feedback to maintain the unbiased state.

Both of these studies indicate that the acceleration of purification rate by feedback is severely hampered by practical constraints.

In this work, we extend the study of quantum state purification by studying the optimality of purification protocols in the presence of key experimental imperfections. The imperfections we consider are measurement inefficiency and extrinsic decoherence as a result of environmental noise. Both these imperfections will be present in most quantum information processing architectures. Hence it is important to consider their effects on purification, and also to formulate optimal strategies for purification in their presence. We do not consider the imperfections arising from finite strength feedback or time delay in the feedback loop, since it is much more difficult to analyze optimality in the presence of these features. The remainder of the paper is structured as follows. In section 2 we introduce the physical system and dynamics we will analyze. In section 3, we find the time local optimal strategy for purification in the presence of imperfections. Section 4 discusses the global optimality of the locally optimal strategy for the `max purity` goal, using a simplified form of the verification theorem (as part of our calculations we derive a simplified form of the verification theorem [54] for verifying global optimality of control protocols, which is presented in appendix A). We also compare the global optimality of the local strategy formulated here against other known protocols. Then the global optimality of local strategy for the `min time` goal is discussed in section 5. A summary and conclusions are presented in section 6.

5.2 Dynamics

We restrict our attention to the case of a quantum two-level system (qubit). Although this is the simplest finite dimensional system, it is also the most relevant from a quantum information perspective since physical implementations of qubits are the fundamental building blocks for most quantum information tasks. In addition, to examine the effect of imperfections on state purification, it suffices to examine the case of a qubit.

The system is subject to a weak, continuous measurement of an operator M with strength k and efficiency η . In addition, we assume the qubit is coupled to a low temperature environment which induces relaxation and decoherence dynamics on the qubit. The master equation describing the time evolution of a qubit with such dynamics is given by [9, 126]

$$d\rho = \gamma_1 \mathcal{D}[\sigma_-] \rho dt + \gamma_\phi \mathcal{D}[\sigma_z] \rho / 2 dt + \mathcal{D}[\sqrt{2k}M] \rho dt + \mathcal{H}[\sqrt{2k\eta}M] \rho dW, \quad (5.1)$$

where ρ is the qubit density matrix, dW is a Wiener increment, and we have set $\hbar = 1$. The super-operators in this equation are defined as: $\mathcal{D}[A]\rho \equiv A\rho A^\dagger - \frac{1}{2}(A^\dagger A\rho + \rho A^\dagger A)$ and $\mathcal{H}[A]\rho \equiv A\rho + \rho A^\dagger - \text{Tr}[(A + A^\dagger)\rho]\rho$. This equation is in a rotating frame with respect to a free Hamiltonian of the form $\frac{1}{2}\omega(t)\sigma_z$, and M and ρ should be interpreted in this rotating frame. Here we have utilized the Born and Markov approximations of the noisy environment in order to summarize its effects on the qubit as Markovian dephasing at rate γ_ϕ and relaxation at rate γ_1 . Since the environment is considered to be at low temperature ($k_B T \ll \omega$), we only consider its de-excitation (relaxation) effects on the qubit. The time-dependent measurement

results, or measurement current, that generates conditioned evolution by Eqn. (5.1) can be expressed as:

$$I(t) = \sqrt{k}\text{Tr}[(M + M^\dagger)\rho(t)] + \xi(t)/\sqrt{\eta}. \quad (5.2)$$

where $\xi(t) = dW/dt$ in a white noise process. In this paper, we assume that the measurement is along the computational basis axis, i.e. $M = J_z = \sigma_z/2$ (note that this M has no time dependence in the rotating frame).

Finally, we add a time-dependent coherent rotation of the qubit, $F(t)$, that constitutes our feedback Hamiltonian. $F(t)$ could be based on the measurement results up to t and generates the following dynamics in addition to Eqn. (5.1) [126]:

$$[\dot{\rho}]_{fb} = -i[F(t), \rho]. \quad (5.3)$$

We consider feedback of arbitrary strength for convenience, including infinite strength feedback which is modeled as instantaneous unitary rotations at any time superposed on the evolution given by Eqn. (5.1).³

Because of rotational invariance about the z axis, going away from the $x - z$ plane does not aid purification. Thus, without loss of generality, we may restrict our attention to the Bloch vector components x and z , and consider the feedback rotation to be about the y axis.

Without feedback, the evolution of the Bloch vector components of the qubit ($\rho = \frac{1}{2}(\mathbf{1} + x\sigma_x + y\sigma_y + z\sigma_z)$) is

$$dx = -(\gamma_2 + k)xdt - \sqrt{2k\eta}xz dW, \quad (5.4a)$$

$$dz = -(\gamma_1 + \gamma_1 z)dt + \sqrt{2k\eta}(1 - z^2)dW, \quad (5.4b)$$

where $\gamma_2 = \gamma_1/2 + \gamma_\phi$ and $r = \sqrt{x^2 + z^2}$.

Using Ito's lemma [126], we can translate Eqn. (5.4) into the following dynamic equation for the variable $r = \sqrt{x^2 + z^2}$, the length of the Bloch vector:

$$\begin{aligned} dr = & [r(\gamma_2 - \gamma_1) + k(r - \frac{\eta}{r})]u^2 dt - \gamma_1 u dt \\ & + [k(\frac{\eta}{r} - r) - \gamma_2 r]dt + \sqrt{2k\eta}(1 - r^2)u dW, \end{aligned} \quad (5.5)$$

with $u = \frac{z}{r}$.⁴ Note that for $u = \pm 1$ we have $z = \pm r$ and the state lies on the z -axis. For $-1 < u < 1$, the Bloch vector makes a non-zero angle with the z axis. The feedback

³Protocols that require “infinite” feedback strength may be approximated reasonably well in circuit QED [118], where microwave rotations are significantly faster than other relevant timescales, namely, $|F(t)| \gg k, \gamma_1, \gamma_\phi$.

⁴The apparent singularity at $r = 0$ can be removed by changing the state variable from r to the purity, P , as we will see in Eqn. (5.7). However, because the qubit dynamics are more readily visualized in terms of the Bloch vector r , and expressions look simpler in r , we will use r as our state variable for the greater part of the presentation in this paper (in situations where the singularity does not affect our results). Numerical calculations of Eqn. (5.5) are handled by setting $u = -1$ at the origin to avoid the singularity.

control (which is a unitary rotation) does not affect the above dynamical equation for r , but it does affect the dynamical equation for u (which is not shown here). However, the assumption of arbitrary strength feedback simplifies the treatment since it implies that we can set u arbitrarily by instantaneous rotation at any time. Therefore, we identify r as our state variable and $u(r, t) \in [-1, 1]$ as our control input in the above dynamics. Some of the actual controls we consider for various optimality conditions below require infinite strength feedback while others do not, and we will make this requirement explicit when relevant.

Finally, we also write down the special case of Eqn. (5.5) with no decoherence for later convenience. That is, when $\gamma_1 = \gamma_\phi = 0$,

$$dr = k(r - \frac{\eta}{r})(u^2 - 1)dt + \sqrt{2k\eta}(1 - r^2)udW. \quad (5.6)$$

5.3 The Locally Optimal Strategy

In this section, we will formulate a locally optimal strategy that maximizes the instantaneous rate of purification in the presence of measurement inefficiency and decoherence. This strategy is the generalization of the unbiased measurement protocol [56, 57] which is also a locally optimal strategy, but was also shown to be globally optimal for purifying qubits with the **max purity** goal, in the ideal case with no imperfections [129]. In the following sections, we will analyze whether this locally optimal strategy is also globally optimal for any goal in the presence of imperfections.

We begin by writing an equation of motion for the purity, which is defined as: $P = \text{Tr}[\rho^2] = \frac{1}{2}(1 + r^2)$. Using Ito's lemma and Eqn. (5.5), we obtain the rate of change of purity as

$$\begin{aligned} dP = & [\gamma_2 - \gamma_1 + k(1 - 2\eta + \eta r^2)]r^2u^2dt - \gamma_1rudt \\ & + [k\eta - (\gamma_2 + k)r^2]dt + \sqrt{2k\eta}(1 - r^2)rudW. \end{aligned} \quad (5.7)$$

This equation consists of a deterministic quantity and a stochastic quantity that is proportional to $dW(t)$. The former gives the rate of change of *average* purity, $\langle \dot{P} \rangle$, since $dW(t)$ averages to zero. Here the angle brackets indicates an average over the stochastic noise processes. Notice if we write r in terms of P on the right hand side, $r = \sqrt{2P - 1}$, this equation can be regarded as the dynamics for the state variable P . Maximizing the instantaneous *average* purification rate, $\langle \dot{P} \rangle$ by choice of rotations around the y axis is equivalent to maximizing the following quadratic function of u :

$$f(u) = [\gamma_2 - \gamma_1 + k(1 - 2\eta + \eta r^2)]r^2u^2 - \gamma_1ru. \quad (5.8)$$

The control that maximizes this function can be considered a *locally* optimal strategy since it maximizes the instantaneous rate of change in average purity, and we label it $u_{lo}(t)$. It is not *a priori* clear that such a locally optimal strategy will be globally optimal for either the **max purity** or **min time** purification goals, and we will investigate this issue in sections 4 and 5 below.

5.3.1 Local optimality in the absence of decoherence

Consider $\gamma_1 = \gamma_\phi = 0$, in which case, $f(u) \rightarrow f_{\text{no-decoherence}}(u) = k(1 - 2\eta + \eta r^2)r^2 u^2$. The maximizers of this function are easily found and are summarized in Table 5.1. Interestingly, the $1/2 < \eta < 1$ case introduces a fragmentation of the locally optimal control strategy that is not present in the ideal case ($\eta = 1$).⁵ Also, Table 5.1 shows that if $\eta \leq 1/2$, the locally optimal strategy is simply to measure diagonally by keeping the state of the qubit in the σ_z basis, i.e., $|u(t)| = 1$. The simplest way to implement this *diagonal measurement* strategy is to perform an initial instantaneous rotation to the z axis (since control is assumed to be instantaneous and at no cost) and no successive feedback, and we will call this the *no-feedback diagonal measurement* protocol. On the other hand, when $\eta = 1$, which is the ideal case that was analyzed in Ref. [56], we recover the unbiased measurement protocol as the locally optimal strategy: $u(t) = 0$. This protocol keeps the qubit in an unbiased basis with respect to the measurement, and $u(t) = 0 \implies z(t) = 0$ is maintained by strong rotations.

In the intermediate case where $1/2 < \eta < 1$, a critical Bloch vector length emerges, $r^* = \sqrt{2 - 1/\eta}$, around which the locally optimal strategy switches between the diagonal measurement protocol and the unbiased measurement protocol. That is, when $r < r^*$ the feedback-induced control $u = 0$ maximizes the rate of change of average purity, while when $r \geq r^*$, the strategy of diagonal measurement maximizes this quantity. We note that there is a critical purity corresponding to the critical Bloch vector length, given simply by $P^* = \frac{1}{2}(1 + r^{*2}) = \frac{1}{2}(3 - 1/\eta)$.

A note is in order about the feedback nature of this locally optimal strategy. Obviously $|u(t)| = 1$ requires no feedback since this corresponds to constant rate measurement along a fixed axis (σ_z) and $F(t) = 0$. $u(t) = 0$ on the other hand requires maintaining the Bloch vector along the x -axis despite measurement-induced fluctuations causing deviations from this axis. To do this, as specified in Jacobs' original unbiased measurement protocol [56, 57, 14] the feedback Hamiltonian must be proportional to the measurement current: $F(t) = \sqrt{2k\eta} \frac{I(t)}{x(t)} J_y$. This is a conditioned rotation since it is inversely proportional to $x(t)$, the x projection of the Bloch vector at the current time instant.⁶ However, it should be noted that this protocol does not require real-time state estimation to execute. This is because in the presence of the feedback, when $u(t) = 0$, the evolution of the x component of the Bloch vector is deterministic, since the feedback effectively cancels the stochastic component of the evolution. In contrast, the locally optimal strategy when $1/2 < \eta < 1$ requires a switch between the diagonal measurement protocol and the unbiased measurement protocol when r crosses r^* . In order to implement this, one requires a real-time estimate of the length of the Bloch vector, $r(t)$, which does not evolve deterministically when $u \neq 0$ as can be seen from Eqn. (5.5). Furthermore, this optimal strategy requires one to rotate the state between the

⁵We note that Combes and Wiseman have previously suggested that such a fragmented, or switching, strategy might be optimal in their study of purification under imperfections [14].

⁶Technically, this $F(t)$ is an unbounded Hamiltonian since $dW(t)$ is unbounded, and furthermore, the initial state $x(0) = 0$. However, it has been shown that tempered approximations of this Hamiltonian suffice to implement the unbiased measurement protocol [14].

x and z axes as the Bloch vector length crosses r^* . More precisely, for $r < r^*$, the feedback prescribed by the unbiased measurement protocol maintains the state on the x -axis (which is unbiased with respect to the measurement along z -axis). When the Bloch vector length increases to $r > r^*$, the locally optimal strategy prescribes a fast rotation of the state from the x -axis to the z -axis (a $\pi/2$ σ_y rotation) followed by no feedback (unless $r < r^*$ again at a late time due to the stochastic evolution of purity under diagonal measurement). These operations require real-time state estimation in addition to rotations that take negligible time. Such requirements make implementation of the locally optimal strategy challenging when $1/2 < \eta < 1$.

Table 5.1: The strategy that maximizes the instantaneous rate of increase of average purity (the locally optimal strategy) when $\gamma_1 = \gamma_\phi = 0$. $r^* = \sqrt{2 - 1/\eta}$ is the critical Bloch vector length at which there is a discontinuous change in protocols when $1/2 < \eta < 1$.

	$\eta \leq 1/2$	$1/2 < \eta < 1$	$\eta = 1$
$u_{lo}(r, t)$	± 1	$\begin{cases} 0 & , r \leq r^* \\ \pm 1 & , r > r^* \end{cases}$	0

To illustrate the behavior of purification in the case when $1/2 < \eta < 1$, Fig. 5.1 shows the average rate of change of purity as a function of the instantaneous purity under both the unbiased measurement protocol and the diagonal measurement protocol. The rate of purification decreases with the instantaneous purity for both protocols, but while this rate is always positive for the diagonal measurement protocol, it can be negative for the unbiased measurement protocol when the purity is large. This is the reason it is advantageous to switch to the diagonal measurement protocol at large purity values. Physically, the reason for this switch is that the feedback required for the unbiased measurement protocol is non-ideal for inefficient measurement, and hence for Bloch vectors that are already large it is preferential to switch off the non-ideal feedback.

Analytical solution for purity evolution when $1/2 < \eta < 1$ When $\eta < 1/2$, the locally optimal strategy is simply measurement along a fixed basis, and in this case an analytical form for the probability distribution for r , the length of the Bloch vector, is easily computed and given in section 4.1 below (since the evolution is simply diffusion along the z -axis after a possible initial rotation to move the state to this axis). Similarly, when $\eta = 1$, when the locally optimal strategy is the unbiased measurement protocol, an expression for the probability distribution for r is given in Ref. [56] (not in closed form however). Here we complete this characterization and calculate an analytical expression for the probability evolution for r in the case of qubit evolution under the locally optimal strategy when $1/2 < \eta < 1$. Note that this case is significantly more complicated than the other two mentioned above since it involves a switching of protocols around the point r^* .

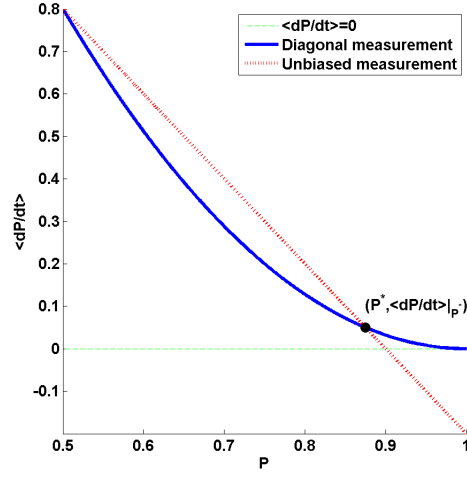


Figure 5.1: Average rate of change of purity as a function of instantaneous purity in the presence of measurement inefficiency, for the diagonal measurement protocol ($|u(r, t)| = 1$) and the unbiased measurement protocol ($u(r, t) = 0$). The point where the locally optimal strategy switched between these protocols is indicated as P^* . Parameters used for this plot are $k = 1$, $\eta = 0.8$, and $\gamma_1 = \gamma_\phi = 0$.

Consider a known initial state of the qubit on the z -axis with $r(0) = r_0$ (e.g., $r_0 = 0$ when $\rho_0 = \mathbf{I}/2$). The probability distribution function $p(r, t)$ of the Bloch vector length at time t is given by the following Fokker-Planck equation with the initial condition $p(r, 0) = \delta(r - r_0)$:

$$\begin{aligned} \frac{\partial}{\partial t} p(r, t) = & - \frac{\partial}{\partial r} \left[k \left(\frac{\eta}{r} - r \right) \theta(r^* - r) p(r, t) \right] \\ & + \frac{\partial^2}{\partial r^2} [k \eta (1 - r^2)^2 \theta(r - r^*) p(r, t)], \end{aligned} \quad (5.9)$$

where $\theta(x)$ is the Heaviside step function.

First consider $r_0 \geq r^*$. In this case the locally optimal strategy implements the diagonal measurement unless the random (diffusive) evolution results in $r(t) \leq r^*$ at some future time t . But when this happens the strategy switches to the unbiased measurement protocol which deterministically increases purity until $r(t + \Delta t) > r^*$ and we are returned to the region where the diagonal measurement protocol is preferred. Therefore, for this initial condition r will not go below r^* for a finite time. Hence we consider the following ansatz for the probability distribution function for r :

$$p(r, t) = p_1(t) \delta(r - r^*) + p_2(r, t) \theta(r - r^*). \quad (5.10)$$

Given this ansatz, the Fokker-Planck equation can be translated into the following set of

equations with initial conditions $p_2(r, 0) = \delta(r - r_0)$ and $p_1(0) = 0$:

$$r\eta(1 - r^2)^2 p_2(r^*, t) = (\eta - r^2) p_1(t), \quad (5.11a)$$

$$\frac{\partial}{\partial r} [k\eta(1 - r^2)^2 p_2(r, t)]|_{r^*} = \frac{\partial}{\partial t} p_1(t), \quad (5.11b)$$

$$\frac{\partial}{\partial t} p_2(r, t) = \frac{\partial^2}{\partial r^2} [k\eta(1 - r^2)^2 p_2(r, t)]. \quad (5.11c)$$

Note that in the region $r > r^*$ Eqn. (5.11)c is the Fokker-Planck equation. Eqn. (5.11)b enforces probability conservation at the boundary $r = r^*$. This set of equations can be solved by an appropriate change of variables: we calculate the solution explicitly in Appendix 5.C. This analytical solution will be utilized when assessing global optimality in the section below.

Now consider the alternative initial condition where $r_0 < r^*$. In this case, the locally optimal strategy implements the unbiased measurement protocol, which will deterministically increase the purity of the qubit according to:

$$r(t) = \sqrt{\eta - (\eta - r_0^2)e^{-2kt}} \quad (5.12)$$

This continues until the critical Bloch vector length is reached and the locally optimal strategy then switches over to the diagonal measurement protocol. Let $r(t^*) = r^*$. Then, after t^* , the non-deterministic diagonal measurement protocol is employed and we simply solve for the qubit dynamics that this prescribes, i.e., solve Eqn. (5.11) for the distribution function with the initial condition $p_2(r, t^*) = \delta(r - r^*)$.

Together with the explicit characterizations of evolution under the locally optimal strategies when $\eta < 1/2$ and $\eta = 1$ described above, this analytic characterization of the probability distribution for the Bloch vector length now provides a complete picture of the evolution of qubit purity under the locally optimal strategy for any measurement efficiency.

5.3.2 Local optimality in the presence of decoherence

In this subsection, we expand our analysis of locally optimal strategies that maximize the instantaneous rate of increase of average purity to the case where decoherence is present. Recall that the general expression for instantaneous average purification rate, which we want to maximize, is given in Eqn. (5.8). For general γ_1 , γ_ϕ , and η , in order to maximize $f(u)$ we require:

$$u_{lo}(r, t) = \begin{cases} -1 & \text{if } \gamma_1 + 2r[\gamma_2 - \gamma_1 + k(1 - 2\eta + \eta r^2)] \geq 0 \\ \frac{\gamma_1}{2r[\gamma_2 - \gamma_1 + k(1 - 2\eta + \eta r^2)]} & \text{otherwise} \end{cases}$$

For the explicit calculations in this work, we will focus on the most realistic situation, where $\gamma_1 \neq 0$, $\gamma_\phi \neq 0$, and $\eta < 1$.

Here, the counterpart of the regime where $\eta \leq 1/2$ in the previous case of no decoherence is the parameter space that yields $u_{lo}(r, t) \equiv -1$. A sufficient condition for this is $\gamma_\phi + k(1 - 2\eta) \geq 0$. In the presence of decoherence, the term $-\gamma_1 r u$ in $f(u)$ (see Eqn. (5.8)) ensures

that $u = +1$ is no longer a maximizing control. Physically, this simply means that because of uncontrollable relaxation (a T_1 process), it is not advantageous to attempt to purify to the excited state of the qubit. Instead, maintaining $u = -1 \implies z < 0$ is the locally optimal strategy. Now to keep the z -component of the qubit negative, we must flip the qubit (e.g., apply π rotation around y axis) whenever our σ_z measurement indicates that it is positive. Therefore this control corresponds to simply having a constant σ_z measurement (which induces diffusive motion along the z axis) that is interrupted by strong σ_y rotations whenever $z(t) > 0$. Such a feedback protocol requires continuous real-time state estimation. We shall refer to this strategy of maintaining the z -component of the qubit negative as the *negative diagonal measurement* protocol.

The negative diagonal measurement protocol is expected to have better performance than the no-feedback diagonal measurement protocol⁷ both locally and globally, as long as $\gamma_1 > 0$. The σ_z measurement has a chance of moving the qubit to the $z > 0$ region and when this happens, the strong feedback rotation in the negative diagonal measurement protocol will change the term $-\gamma_1 z$ in Eqn. (5.7) to $+\gamma_1 z$, while keeping all others invariant. This will generate a larger instantaneous purification rate. Therefore, for any noise realization $dW(t)$, the negative diagonal measurement protocol gives a trajectory that has a purity larger than or equal to evolution under the no-feedback diagonal protocol at any time. We will see this manifest in the numerical simulations assessing global optimality in sections 5.4 and 5.5.

In the parameter space where $u_{lo}(r, t) \neq 1$, $u_{lo}(r, t)$ has complicated dependence on r . We have plotted its value for a typical set of parameters in Fig. 5.4a. When the condition $\gamma_1 + 2r[\gamma_2 - \gamma_1 + k(1 - 2\eta + \eta r^2)] \geq 0$ is not met, one must perform precise rotations around the y axis so that $u = \frac{\gamma_1}{2r[\gamma_2 - \gamma_1 + k(1 - 2\eta + \eta r^2)]}$ is maintained. This also requires continuous real-time state estimation, and furthermore, requires precise knowledge of all the parameters in the system. Executing this locally optimal strategy in the presence of decoherence is hence very challenging from a practical standpoint.

The locally optimal strategy in the presence of decoherence is significantly more complex than that in the absence of decoherence. As a result we have been unable to formulate an analytical solution for the probability distribution of the Bloch vector length in this case.

5.4 Global Optimality for the max purity goal

In this section, we will consider the **max purity** purification goal, i.e., to maximize $P(t) = \frac{1}{2} + \frac{1}{2} \int_0^1 dr r^2 p(r, t)$ with a fixed purification time t , and ask whether the locally optimal strategies formulated in the previous sections are *globally* optimal for this goal. We note that in the ideal case (no decoherence and measurement efficiency $\eta = 1$) global optimality of the locally optimal strategy (i.e., the unbiased measurement protocol when $\eta = 1, \gamma_1 = \gamma_\phi = 0$) was proven in Ref. [129]. In the following subsections we investigate the extent of global optimality in other parameter regimes.

⁷While the no-feedback diagonal measurement may come with an initial rotation to either $+z$ or $-z$ axis in the decoherence free regime, we will choose the more advantageous initial rotation to the $-z$ axis here.

5.4.1 No decoherence and $\eta \leq 1/2$

In this regime, we found the locally optimal control to be $u(r, t) \equiv \pm 1$, which is the diagonal measurement protocol. Here we use the verification theorem to prove that the locally optimal solution is actually globally optimal. Appendix 5.A reviews the verification theorem [54] and provides a simplified form that is useful for the present calculations. The verification theorem provides a sufficient set of criteria to test the global optimality of a presumed solution. We will use P instead of r as the state variable in this subsection to avoid complications deriving from the $r = 0$ singularity in the dynamical equation for r (see Eqn. (5.5)). At the first step, we need to calculate a cost function $C(P, t)$, which is defined as the average impurity $\langle L(T) \rangle = 1 - \langle P(T) \rangle$ at time T , given that the purity is P at time t . For an arbitrary initial state, the no-feedback diagonal measurement protocol specifies an initial rotation of the qubit to the z -axis and then simple measurement in the z -basis (no feedback). Since the initial rotation is assumed to be instantaneous, the dynamics under this protocol is the subsequent motion along the z axis. This density matrix evolution under measurement alone can be solved with the method of linear quantum trajectories [55]. Given $z(0^+) = z_0$ (the 0^+ time simply indicates the time after the instantaneous rotation to the z -axis), $z(t)$ can be written as:

$$z(R(t)) = \tanh(\operatorname{arctanh}(z_0) + \sqrt{2k\eta}R(t)), \quad (5.13)$$

where $R(t)$ is a random variable whose distribution function at time t is given by:

$$p(R, t) = \exp\left(\frac{R^2}{2t} - k\eta t\right) \sqrt{\frac{1 - z_0^2}{2\pi t}} \cdot \cosh(\operatorname{arctanh}(z_0) + \sqrt{2k\eta}R). \quad (5.14)$$

We find the cost function $C(P, t)$ using this distribution as

$$C(P, t) = \frac{\exp[-k\eta(T - t)] \sqrt{2(1 - P)}}{\sqrt{8\pi(T - t)}} \cdot \int_{-\infty}^{+\infty} \operatorname{sech}[\operatorname{arctanh}(\sqrt{2P - 1}) + \sqrt{2k\eta}R] \cdot \exp\left[-\frac{R^2}{2(T - t)}\right] dR. \quad (5.15)$$

The G function for our dynamics (5.7), defined in appendix 5.A, is related to the derivatives of the cost function by:

$$G(P, t) = -k(2P - 1) \cdot [4\eta(P - 1)^2 \frac{\partial^2 C}{\partial P^2} + (1 - 3\eta + 2\eta P) \frac{\partial C}{\partial P}] u^2 - k(1 + \eta - 2P) \frac{\partial C}{\partial P}. \quad (5.16)$$

The derivatives $\frac{\partial C}{\partial t}$ and $\frac{\partial^2 C}{\partial P^2}$ are continuous over the interval $[0, T)$ as required by the verification theorem. The cost function in (5.15) gives the G function a nonnegative coefficient in front of u^2 (including the minus sign) for all P and t . The explicit form of this coefficient is derived in Appendix 5.B. Therefore, $u(P, t) \equiv \pm 1$ are the maximizers of the G function, and the verification procedure concludes that the corresponding diagonal measurement protocol is globally optimal in this parameter regime.

5.4.2 No decoherence and $1/2 < \eta < 1$

In the regime $1/2 < \eta < 1$, the locally optimal strategy combines the diagonal measurement protocol and the unbiased measurement protocol, with a switch between these at a critical Bloch vector length r^* . In this case, however, one can show that this locally optimal strategy is not globally optimal. To do so, we can solve for average purity as a function of time and compare it against the corresponding purity derived from other protocols. In section 5.3.1 we obtained an analytical form for the probability distribution for the Bloch vector length as a function of time, $p(r, t)$, when using the locally optimal strategy. With this distribution function, the average purity, $\langle P(t) \rangle$, can be calculated by a simple integral.

Figures 5.2a and 5.2b show how the average purity evolves as a function of time (for three different control strategies) in the absence of decoherence, with parameters chosen so that $r_0 < r^*$ and $r_0 > r^*$, respectively. We have tested a wide range of parameter values and the results are qualitatively the same throughout this regime of measurement efficiency ($1/2 < \eta < 1$). With $r_0 < r^*$, the locally optimal strategy initially outperforms the diagonal measurement protocol as expected. However, the diagonal measurement protocol (i.e., constant σ_z measurement) catches up later and purifies more effectively at late times. The catch up time occurs before the Bloch vector length reaches r^* using the locally optimal strategy. When $r_0 \geq r^*$, Fig. 5.2b, the locally optimal strategy never outperforms the diagonal measurement protocol⁸.

The fact that there is a performance difference between the locally optimal strategy and the diagonal measurement protocol when $r_0 \geq r^*$ needs some explanation. When $r_0 > r^*$, initially the locally optimal strategy is exactly the diagonal measurement protocol. However, as time progresses, while the diagonal measurement protocol simply causes diffusion of $r(t)$ along the z -axis, the locally optimal strategy switches to the unbiased measurement protocol if $r(t)$ drops below r^* at any future time. The subsequent deterministic increase of purity caused by the unbiased measurement protocol results in $r(t + \Delta t) > r^*$ again for some small Δt . Then the switch back to the diagonal measurement protocol causes diffusion of $r(t)$ again. The net result of this switching back-and-forth at the boundary is a build-up of probability at $r = r^*$ at intermediate times. This concentration of probability weight at $r = r^*$ gives rise to a smaller cumulative probability in the $r > r^*$ region than the diagonal measurement protocol. This is illustrated in Fig. 5.3, which shows the time-development of the probability distribution, $p(r, t)$, when $r_0 > r^*$ for both the locally optimal strategy and the diagonal measurement protocol. This probability concentration at the boundary is an interesting consequence of the switching behavior of the locally optimal strategy. This example demonstrates that while protocol switching can lead to local optimality, it can be detrimental to global optimality in some instances.

We also note that the unbiased measurement protocol eventually performs worse than both of the other protocols (diagonal measurement and the locally optimal strategy), regardless of the initial state. This demonstrates that using the optimal strategy derived for perfect

⁸For very short times the difference between purities for the two protocols is within numerical error.

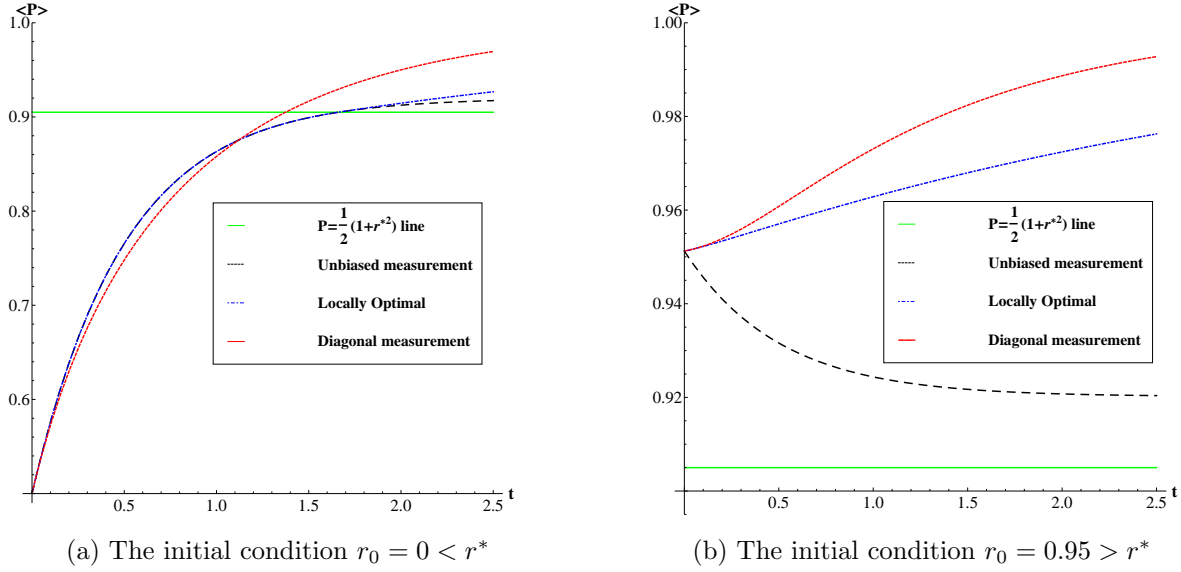


Figure 5.2: Average purity vs. time in the case of no decoherence for the unbiased measurement protocol, the locally optimal strategy, and the diagonal measurement protocol for two different initial purities. The parameters used here are $k = 1$, $\eta = 0.84$ ($r^* = 0.9$), and $\gamma_1 = \gamma_\phi = 0$.

efficiency measurements $\eta = 1$ can be inappropriate if actually the measurement efficiency is less than unity.

From the above analysis we conclude that, for the **max purity** goal, the locally optimal strategy, which maximizes the rate of increase of average purity at any time instant, is also globally optimal for both $\eta \leq 1/2$ and $\eta = 1$. Therefore, feedback control is not helpful at all for the **max purity** goal when $\eta \leq 1/2$. Instead, the locally optimal strategy in this regime is simple measurement. In contrast, in the regime $1/2 < \eta < 1$, we cannot conclude that any strategy is globally optimal.

5.4.3 In the presence of decoherence

We have not been able to apply the verification theorem to prove global optimality of the locally optimal strategy for the **max purity** goal in any parameter regime in the presence of decoherence. However, we speculate that in the parameter regime where the negative diagonal measurement protocol is the locally optimal strategy (this regime is specified by the inequality $\gamma_1 + 2r[\gamma_2 - \gamma_1 + k(1 - 2\eta + \eta r^2)] \geq 0, \forall r$), that it is also the global optimum. This is because in this regime it is advantageous to cooperate with the relaxation process, which also induces purification, and this is precisely what the negative diagonal measurement protocol does. When the locally optimal strategy has a more complicated r dependence (e.g., that in Fig. 5.4a), we numerically simulate the performance of the four different

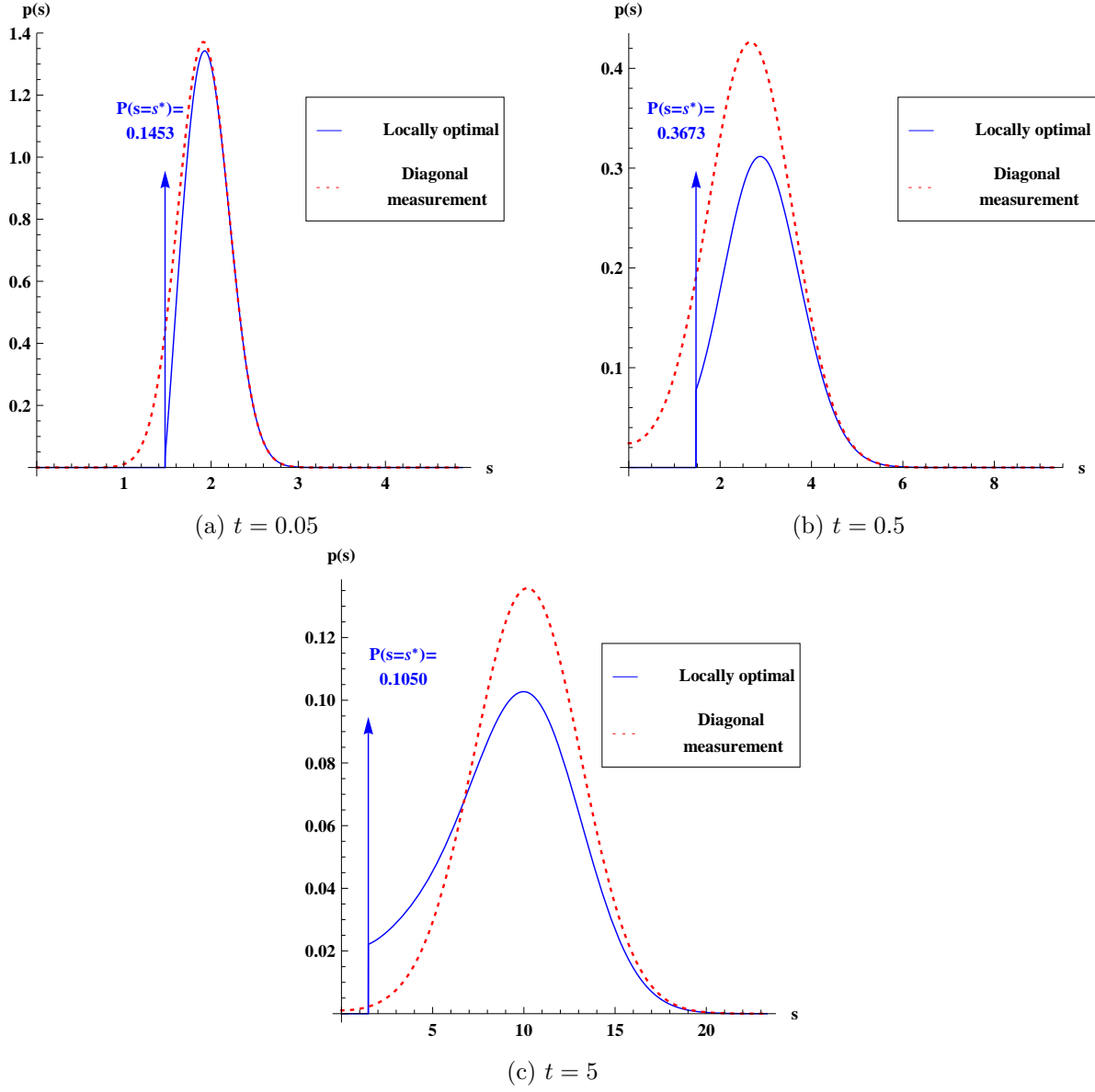


Figure 5.3: Behavior of the solution to the Fokker-Planck equation, Eqn. (5.9) at three different times t , visualized by the distribution of $s(t) = \text{arctanh}(r(t))$ as the qubit evolves under the locally optimal and the diagonal measurement protocols. Both protocols operate on a qubit initially at the same purity, with $r_0 = 0.95$. Parameters used are the same as in Fig. 5.2, namely $k = 1$, $\eta = 0.84$ ($r^* = 0.9$), and $\gamma_1 = \gamma_\phi = 0$.

protocols we considered so far (using the Euler-Maruyama algorithm [59] for those protocols involving stochastic integration). Fig. 5.4b shows the behavior of average purity as a function of time for a typical set of parameters. The performance of the free evolution (with no measurement at all) is also added for comparison, since the relaxation dynamics itself induces purification. The negative diagonal measurement protocol is superior to the no-feedback diagonal measurement protocol as expected. It also achieves greater values of purity than the locally optimal strategy in the long run, similar to the situation found in the decoherence free case. The locally optimal strategy is also superior to the no-feedback diagonal measurement strategy.⁹ The above facts suggest that, in the presence of decoherence, qubit purification measured by the `max purity` goal will always benefit from feedback, even though in the absence of decoherence the corresponding preferred purification strategy may be no feedback (at long times).

5.5 Global optimality for the `min time` goal

In this section, we consider the `min time` goal, i.e., to minimize $-\int_1^0 tdq(t)$, where $q(t)$ is the probability of not reaching a fixed target Bloch vector length at time t . We will determine whether the locally optimal strategies identified above are globally optimal in any parameter regime for this goal.¹⁰

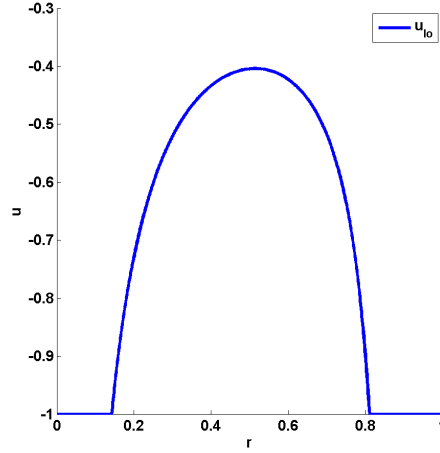
5.5.1 In the absence of decoherence

For the `min time` purification goal in the absence of decoherence, Wiseman and Bouten proved that the diagonal measurement protocol is globally optimal for perfectly efficient measurements, $\eta = 1$ [129]. We show here that in the absence of decoherence this is true for all values of measurement efficiency η using the verification theorem. In this subsection, we will again use P as the state variable, and r should be interpreted as a function of P , namely, $r = \sqrt{2P - 1}$.

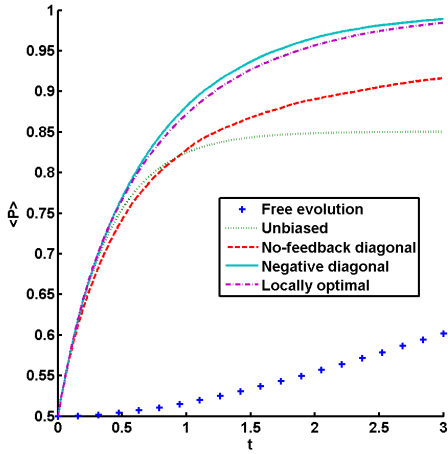
Let r_f be the final Bloch vector length that we want to achieve. The cost function $C(P, t)$ for this goal is the average remaining time of the first passage through r_f ($r_f < 1$), given that the qubit is at $r = \sqrt{2P - 1}$ ($r \leq r_f$) at time t . We took the approach given in Ref. [128] to calculate this `min time` cost, and solved the Fokker-Planck equation with absorbing boundary conditions at $r = r_f$. If $p(r, t)$ is the solution of this equation, then the probability of not hitting the target r_f by time t is $q(t) = \int_{-r_f}^{r_f} p(r, t) dr$. The average time of reaching the boundary is then obtained from $q(t)$ by integration, namely $-\int_0^\infty t \dot{q}(t) dt = \int_0^\infty q(t) dt$.

⁹At least when the decoherence rates are not too small.

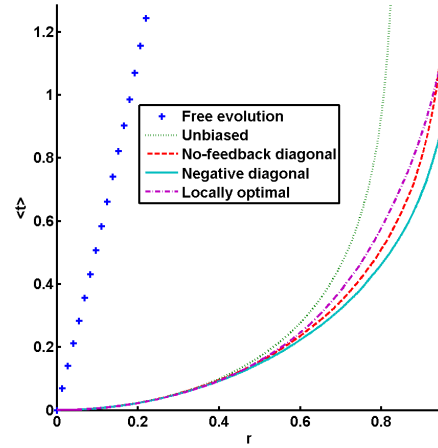
¹⁰We note that a convenient feature of the `min time` goal is that its evaluation does not depend on the definition of purity used; any definition of purity as an increasing function of r is equivalent.



(a) The locally optimal control



(b) The average purity vs. time



(c) The average time vs. the target Bloch vector length

Figure 5.4: Performance comparison of the free evolution, the locally optimal strategy, the no-feedback diagonal measurement, the unbiased measurement, and the negative diagonal measurement protocols in the presence of decoherence for initial condition $\rho_0 = \mathbf{I}/2$ ($r_0 = 0$). The chosen parameters are $k = 1$, $\eta = 0.91$, $\gamma_1 = 0.2$, $\gamma_2 = 0.3$. 5.4a plots the locally optimal strategy for this chosen set of parameters. Notice the switch from the preferred negative diagonal measurement control at small and large r values ($u_{lo}(r, t) = -1$) to a more complex preferred control ($u_{lo}(r, t) > -1$) for intermediate values of r . 5.4b shows the average purity (over 40,000 runs) vs. time and 5.4c shows the average purification time (over 20,000 runs) as a function of the target Bloch vector length for the five protocols. The statistical variation in the simulations is comparable to the line-width of the plots, so error bars are not explicitly shown.

After the initial rotation to the z -axis that the diagonal measurement protocol prescribes, $z(0^+) = r$. Then $C(P, t)$ can be obtained as described above, and takes the form

$$C(P, t) = (r_f \times \operatorname{arctanh}(r_f) - r \times \operatorname{arctanh}(r))/2k\eta. \quad (5.17)$$

Substituting this form into the G function, Eq. (5.16), results in the following expression for the coefficient of u^2 :

$$1 + \frac{1}{2}\left(\frac{r}{\eta} - \frac{1}{r}\right)(\operatorname{arctanh}r + \frac{r}{1-r^2}), \quad (5.18)$$

where $r \in [0, r_f]$.

It can be shown that Eq. (5.18) is nonnegative if $\eta = 1$. Since it is a decreasing function of η , the expression is also nonnegative for all η . The diagonal measurement protocol thus maximizes the function G , and by the verification theorem (Appendix 5.A) it is globally optimal. Therefore in the absence of decoherence, feedback is not beneficial for the `min time` goal, regardless of the efficiency of measurement.

5.5.2 In the presence of decoherence

In the presence of decoherence we cannot prove global optimality of any of the protocols, but we do have strong numerical evidence suggesting that the negative diagonal protocol is globally optimal for the `min time` goal in the presence of relaxation. We numerically simulated the qubit purification under the locally optimal, the no-feedback diagonal, unbiased measurement, and the negative diagonal measurement protocols with the Euler-Maruyama algorithm for many combinations of parameters. In Fig. 5.4c we show results for one particular parameter combination, but qualitatively similar results are obtained for all parameter regimes simulated. We find that the negative diagonal measurement protocol is always superior to the other alternatives, particularly the locally optimal one and the no-feedback diagonal one. Therefore, we speculate that the negative diagonal measurement protocol constitutes the globally optimal strategy for the `min time` problem, regardless of decoherence rates or measurement efficiency. We also conclude that feedback is likely advantageous for the `min time` goal in the presence of decoherence.

5.6 Conclusions

Optimal feedback control can provide a crucial element of precision control in solid-state quantum systems, where the measurement process typically requires a non-negligible time to complete. In this work, we studied the optimality of feedback control protocols for qubit purification in the presence of decoherence and with realistic detectors characterized by non-ideal efficiency ($\eta < 1$). We considered the two control goals: (i) maximizing the average purity at a target time (`max purity`) and (ii) minimizing the average time to reach a specific purity threshold (`min time`).

When environmental decoherence is negligible and the only source of decoherence is the measurement back-action, we arrived at the following conclusions. For the **max purity** goal and detector efficiency less than 1, we found that the globally optimal protocol is significantly different from the unbiased measurement protocol that is known to be globally optimal for this goal when $\eta = 1$ [129]. This underscores the fact that one should be careful when extrapolating the optimality of feedback control protocols from idealized to realistic scenarios. The diagonal measurement protocol, which is an initial rotation to the z -axis followed by measurement in the z basis, is optimal when $\eta \leq 1/2$, as analytically verified by the verification theorem. The diagonal measurement protocol also performs very well when $1/2 < \eta < 1$, where indeed it outperforms the locally optimal protocol in the long time limit. We were however unable to find the global optimal solution in this regime. In contrast, the situation for the **min time** purification goal is quite different. Here the diagonal measurement protocol is known to be the (globally) optimal solution for an ideal detector [129]. In this work we showed that this optimality under the most ideal conditions holds for all values of detector efficiency η , as long as no decoherence is present.

We then explored the effects of decoherence on the optimal feedback strategies in addition to non-ideal ($\eta < 1$) detectors. The decoherence sources were modeled by independent dephasing and relaxation processes under Markovian conditions. Here extensive numerical simulations show that the negative diagonal measurement protocol, which is designed to maintain the qubit in the negative segment of the z axis by strong feedback, outperforms the other three feedback strategies (unbiased measurement, no-feedback diagonal, and locally optimal) for the **min time** goal, and for the **max purity** goal in the long time limit. Similar to the decoherence free case, there is a regime where the negative diagonal measurement protocol is not locally optimal. (It typically happens when the measurement efficiency is high and decoherence is weak.) Nevertheless, the negative diagonal measurement protocol achieves better average purity than the locally optimal one after a certain time. The negative diagonal measurement protocol's good performance for both problems strongly suggests that feedback is useful in the presence of decoherence.

An interesting aspect of the study presented here is the behavior of the locally optimal protocol when $1/2 < \eta < 1$, and in the absence of decoherence. This protocol involves switching between two strategies, unbiased measurement and diagonal measurement, which corresponds to a switching between regions where the purity increases ballistically and diffusively, respectively. We demonstrated that this switching behavior results in a concentration of probability (of purity) around the boundary that defines the switching behavior. This novel aspect results directly from the dynamic switching of protocols and to the best of our knowledge has not been explored in other quantum control contexts.

Overall, this work extends prior optimal control results in the quantum realm to include realistic experimental conditions and shows that significant modifications of optimal feedback control strategies can arise in the presence of decoherence. In future it will be interesting to further extend these studies to analysis for qubits coupled to non-Markovian environments, to determine how the detailed behavior of an environment may enter the optimal control strategy.

Appendix

5.A The Verification Theorem

In this appendix, we review the procedure for verifying the (global) optimality of a given solution to a stochastic control problem. An introduction to this topic can be found in Ref. [54].

Consider the general dynamical equation for a stochastic system:

$$d\mathbf{x} = \mathbf{A}(t, \mathbf{x}, \mathbf{u}(\mathbf{x}, t))dt + \mathbf{B}(t, \mathbf{x}, \mathbf{u}(\mathbf{x}, t))d\mathbf{W}. \quad (5.19)$$

Here the state of the system is given by the vector \mathbf{x} , and the vector $\mathbf{u}(\mathbf{x}, t)$ denotes the control inputs. (The region that bounds $\mathbf{u}(\mathbf{x}, t)$ shall not depend on \mathbf{x} or t .) The vectors \mathbf{A} and \mathbf{B} are coefficients of the deterministic and stochastic parts of the dynamics, respectively.

The control objective is to minimize a cost, J :

$$J = \left\langle \int_0^T L(\mathbf{x}, \mathbf{u}(\mathbf{x}, s), s)ds + M(\mathbf{x}(T)) \right\rangle, \quad (5.20)$$

where $L(\mathbf{x}, \mathbf{u}(\mathbf{x}, t), t)$ is the cost rate, usually the consumed energy penalty, and $M(\mathbf{x}(T))$ is the cost of the final state at time T .

The cost function, $C(\mathbf{x}, t)$, is defined as the partial cost over the interval $[t, T]$, given that the system is at state \mathbf{x} at time t :

$$C(\mathbf{x}, t) = \left\langle \int_t^T L ds + M(\mathbf{x}(T)) \right\rangle. \quad (5.21)$$

To determine whether a given control protocol, $\mathbf{u}_c(\mathbf{x}, t)$, is optimal, one performs the following three steps:

1. Integrate the equations of motion of the system to calculate the cost function, $C(\mathbf{x}, t)$, for this protocol.
2. Check that C satisfies two continuity conditions:

$$\frac{\partial C}{\partial t} \quad \text{and} \quad \frac{\partial^2 C}{\partial \mathbf{x}^2} \quad (5.22)$$

are continuous. Here $\partial^2 C / \partial \mathbf{x}^2$ denotes the matrix of second derivatives of C .

3. Determine whether or not $\mathbf{v}(\mathbf{x}, t) = \mathbf{u}_c(\mathbf{x}, t)$ is a maximizer of the following function of \mathbf{v} :

$$\begin{aligned} G(t, \mathbf{x}, \mathbf{v}) = & -\frac{1}{2} \text{Tr} \left[\mathbf{B}^\dagger(t, \mathbf{x}, \mathbf{v}) \frac{\partial^2 C}{\partial \mathbf{x}^2} \mathbf{B}(t, \mathbf{x}, \mathbf{v}) \right] \\ & - \mathbf{A} \cdot \frac{\partial C}{\partial \mathbf{x}} - L(t, \mathbf{x}, \mathbf{v}). \end{aligned} \quad (5.23)$$

Note that one must check that $\mathbf{u}_c(\mathbf{x}, t)$ maximizes G separately at each time t and at each value of \mathbf{x} .

The above verification procedure provides a sufficient condition for a control strategy to be optimal. In Ref. [54], the procedure has four steps, and we have removed the third step by realizing that the Hamilton-Jacobi-Bellman equation is automatically satisfied if the \mathbf{u}_c maximizes Eq. (5.23).

For a time-optimal control problem where the goal is minimizing the average time taken for a function $h(\mathbf{x}(t), t)$ of the dynamical variables (and perhaps of time) to cross a fixed threshold h_c , the same three-step verification procedure still holds. Please note that the cost function $C(\mathbf{x}, t)$ should be defined as the average remaining time it will take to cross the threshold, given that the current time is t and current state is \mathbf{x} . The corresponding function G in step (3) is defined as

$$G(t, \mathbf{x}, \mathbf{v}) = -\frac{1}{2} \text{Tr} \left[\mathbf{B}^\dagger(t, \mathbf{x}, \mathbf{v}) \frac{\partial^2 C}{\partial \mathbf{x}^2} \mathbf{B}(t, \mathbf{x}, \mathbf{v}) \right] - \mathbf{A} \cdot \frac{\partial C}{\partial \mathbf{x}}. \quad (5.24)$$

5.B The Coefficient of the u^2 Term

In this appendix, we will prove that the coefficient of the u^2 term in Eq. 5.16 is nonnegative for all $P \in [\frac{1}{2}, 1]$, $\eta \in [0, 0.5]$, $k > 0$, and $T - t > 0$ with $C(r, t)$ given by Eq. 5.15.

The coefficient works out to be the following expression up to a positive factor:

$$\begin{aligned} & \int_{-\infty}^{+\infty} \{ 2\eta r(1 - r^2) \text{sech}^2[\text{arctanh}(r) + \sqrt{2k\eta}R] \\ & + (r^2 - \eta) \{ r + \tanh[\text{arctanh}(r) + \sqrt{2k\eta}R] \} \} \\ & \cdot \text{sech}[\text{arctanh}(r) + \sqrt{2k\eta}R] \exp\left(-\frac{R^2}{2(T-t)}\right) dR. \end{aligned} \quad (5.25)$$

First, we ignore η in the expression $k\eta$ because it can always be absorbed by k , and then we divide the above expression by η . It is easy to see that the resultant expression is a decreasing function of η , because the following integral is nonnegative from symmetry analysis:

$$\begin{aligned} & \int_{-\infty}^{+\infty} \tanh[\text{arctanh}(r) + \sqrt{2k\eta}R] \\ & \cdot \text{sech}[\text{arctanh}(r) + \sqrt{2k\eta}R] \exp\left(-\frac{R^2}{2(T-t)}\right) dR. \end{aligned} \quad (5.26)$$

Therefore, we only need to prove the positivity of Expression 5.25 for $\eta = \frac{1}{2}$. Expanding the hyperbolic functions with the addition formulas yields the following expression for the integrand:

$$\frac{2r^5 + (2r^2 - 1)(3r^2 + 1) \tanh R + r(5r^2 - 3) \tanh^2 R}{2(1 + r \tanh R)^3}$$

$$\cdot \sqrt{1 - r^2} \operatorname{sech} R \exp\left(-\frac{R^2}{2(T - t)}\right). \quad (5.27)$$

Because an odd function of R contribute nothing to the integral, we only need to take into account the even component of the integrand, which turns out to be the following expression up to a positive factor:

$$\begin{aligned} & (-6r^7 + 16r^5 - 8r^3) \tanh^4 R \\ & + (6r^7 - 18r^5 + 8r^3) \tanh^2 R + 2r^5. \end{aligned} \quad (5.28)$$

From the properties of parabolic functions, it can be shown that the above expression, and thus the even component of the integrand, is nonnegative for all R . Therefore, Expression 5.25 is nonnegative.

5.C Explicit Solution of Eq. (5.11)

Eqs. (5.11a) and (5.11b) can be combined to give a boundary condition for $p_2(r, t)$. Then we would like to make a change of variables. Let $r = \tanh s$ (similarly for r^* and r_0), and let $p_2(r, t) = \operatorname{sech} s_0 e^{-k\eta t} \cosh^3 s Q(s, t)$. Eq. (5.11) gets translated into the following equations with the initial condition $Q(s, 0) = \delta(s - s_0)$.

$$[-Q(s, t) - A \frac{\partial}{\partial s} Q(s, t) + B \frac{\partial}{\partial t} Q(s, t)]|_{s=s^*} = 0, \quad (5.29a)$$

$$\frac{\partial}{\partial t} Q(s, t) = k\eta \frac{\partial^2}{\partial s^2} Q(s, t), s > s^*, \quad (5.29b)$$

where $A = \operatorname{csch}^2 s^* \coth s^*$ and $B = \coth^2 s^* / (k\eta)$.

If $Q(s, t)$ is a solution to the above equations, it is easy to see that $q(s, t) = -Q(s, t) - A \frac{\partial}{\partial s} Q(s, t) + B \frac{\partial}{\partial t} Q(s, t)$ is a solution to the same heat equation (5.29b) with the boundary condition (5.29a) replaced by $q(s^*, t) = 0$. We can express Q in terms of q as

$$\begin{aligned} Q(s, t) = & -\frac{1}{A} \int_{-\infty}^0 \exp\left(\frac{x}{A}\right) q(s + x, t - \frac{Bx}{A}) dx \\ & + \exp\left(-\frac{s}{A}\right) f\left(\frac{B}{A}s + t\right), \end{aligned} \quad (5.30)$$

where $f(x)$ is an arbitrary function of x .

The solution to the heat equation with no boundary is given by

$$Q_0(s, t) = \frac{1}{2\sqrt{\pi\eta kt}} \exp\left(-\frac{(s - s_0)^2}{4\eta kt}\right). \quad (5.31)$$

Let $q_0(s, t) = -Q_0(s, t) - A \frac{\partial}{\partial s} Q_0(s, t) + B \frac{\partial}{\partial t} Q_0(s, t)$. We set $q(s, t) = q_0(s, t) - q_0(2s^* - s, t)$ so it satisfies the heat equation and vanishes at s^* . In order for $Q(s, t)$ in Eq. (5.30) to meet the initial condition, we also need to set $f(x) = D \exp(\frac{AC+1}{B}x)$, where

$$C = \frac{A - \sqrt{A^2 + 4B\eta k}}{2B\eta k}, \quad (5.32a)$$

$$D = \frac{2AC \exp[C(s_0 - 2s^*)]}{\sqrt{A^2 + 4B\eta k}}. \quad (5.32b)$$

It can be verified that the resulting $Q(s, t)$ given by Eq. (5.30) is the desired solution.

Chapter 6

Circuit QED

Cavity quantum electrodynamics (cavity QED) studies the interaction between photons confined in a high quality cavity and atoms (or artificial atoms). The quantum nature of the light and matter can be studied, demonstrated, and utilized in Cavity QED. In particular, a cavity is a very sensitive device to control and measure a quantum state, where suppression and enhancement of spontaneous decay, vacuum Rabi oscillations, light squeezing can all be realized. Cavity QED is an excellent testbed for the theory of open quantum system and measurement induced decoherence. Moreover, as photons in the cavity can mediate the coupling between distance atoms, cavity QED provides a promising architecture for quantum information processing and communication.

Cavity QED has been demonstrated with both optical photons [46] and microwave photons [91]. In the microwave regime, one typically integrates an artificial atom and a microwave resonator into circuits, which can potentially be made scalable using semiconductor fabrication technology. This scheme is called circuit QED, the main topic of this chapter. Circuit QED has several advantages over optical cavity QED. First, the coupling between the artificial atom and photons can be made much larger due to small volume of the resonator and large effective dipole of the artificial atom. Second, the coupling has less fluctuation because the atom can be fixed in space rather than floating in the cavity. Third, it is much easier to put multiple atoms in the cavity, which allows for multi-qubit gates and entanglement generation [136].

In Sec. 6.1 we are going to see how quantum states can be measured and controlled in a circuit QED system. Sec. 6.2 and 6.3 explore two popular choices of artificial atoms, superconducting qubits and quantum dots. The derivation of the quantum capacitance of a qubit using linear response theory and its application to a quantum dot charge qubit are my independent work. For the rest of the chapter, I will abbreviate an ‘artificial atom’ with just an ‘atom’.

6.1 Measurement and Control in Circuit-QED

Electromagnetic resonators have experimentally been built in 1D [6], 3D [1], out of large Josephson junctions [71], and out of lumped LC circuits [69]. Let us look at the 1D transmission line design as an example. Let l be the length of the line and R_l , L_l , G_l , C_l be the resistance, inductance, conductance, and capacitance per unit length. The characteristic impedance of the transmission line is defined as [90]

$$Z_0 = \frac{R_l + i\omega L_l}{G_l + i\omega C_l}, \quad (6.1)$$

and the complex propagation constant is defined as [90]

$$\gamma = \sqrt{(R_l + i\omega L_l)(G_l + i\omega C_l)}. \quad (6.2)$$

If the transmission line carries a load of impedance Z_L at one end, its impedance measured from the other end is given by [90]

$$Z_{in} = Z_0 \frac{Z_L + Z_0 \tanh \gamma l}{Z_0 + Z_L \tanh \gamma l}. \quad (6.3)$$

This formula tells us that a nearly lossless (low R_l and low G_l) transmission line exhibits an impedance resonance behavior when the length l is about an integer multiple of a quarter wavelength and the line is terminated with high ($Z_L \gg Z_0$ and $Z_{in} \approx Z_0 / \tanh(\gamma l)$) or low ($Z_L \ll Z_0$ and $Z_{in} \approx Z_0 \tanh(\gamma l)$) impedance. For a resonator terminated with low impedance shown in Fig. 6.1, a high impedance resonance (i.e. a sharp peak in Z_{in}) will be seen when l is around a quarter wavelength.¹ Such resonance will be assumed for the rest of this chapter.

The behavior of a cavity near resonance can be approximated by a parallel LC resonator (with inductance L_r and capacitance C_r) as shown in Fig. 6.2 [102]. In cavity QED, the effect of the atom coupled to the cavity can be approximated by an additional quantum capacitance. This capacitance, which depends on the state of the atom, will shift the resonance frequency slightly up or down. A measurement pulse sent through the resonator can detect the frequency shift and therefore indirectly probe the state of the atom. A control pulse can also be sent through the resonator to modify the state of the atom. Let us see mathematically how this system works.

Let us model the atom as a two-level system, i.e., a qubit. This model provides a good approximation when other eigenstates are far away from or have little coupling with the lowest two. Let us first treat the resonator classically and denote the voltage across the electrodes connected with the qubit by V_r . We will use the following linear coupling model for the total Hamiltonian of the qubit in the presence of the cavity:

$$H(t) = \frac{1}{2} \hbar \omega_a \sigma_z + (q_0 I + q_x \sigma_x + q_z \sigma_z) V_r(t), \quad (6.4)$$

¹Because the current goes to zero at the antinodes.

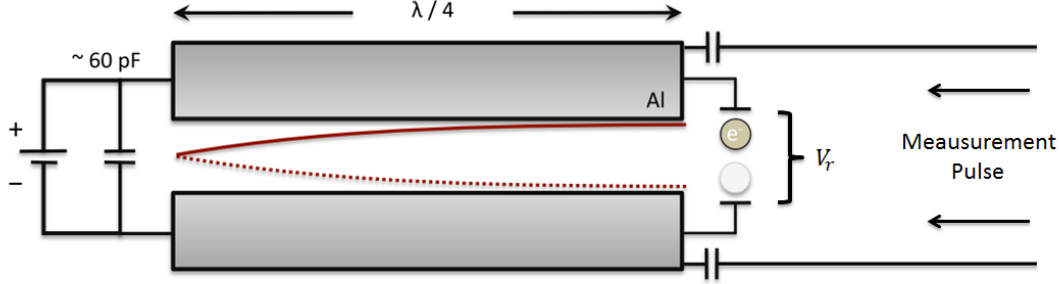


Figure 6.1: Schematics of a circuit QED setup with a quarter wave length transmission line resonator. The right end of the resonator, where measurement and control pulses are sent in and reflected, is coupled to a quantum dot. The left end of the resonator is terminated with a large capacitor which is effectively a short circuit under AC. (Courtesy of Thorsten Last.)

where ω_a is the qubit frequency, and q_0 , q_x , and q_z are the coupling constants. (The σ_y coupling can always be made zero by a basis rotation.)²

Let $H_0 = \frac{1}{2}\hbar\omega_a\sigma_z$ be the unperturbed Hamiltonian and $H'(t) = -QV_r(t)$ be the perturbation, where $Q = -q_0I - q_x\sigma_x - q_z\sigma_z$. Q has the obvious interpretation of the charge operator.

We will denote operators in the interaction picture with a subscript I . Near resonance, the qubit will go through Rabi oscillations. However, in the dispersive regime, where $\hbar|\omega_d - \omega_a| \gg |q_x|V_{r0}$, the state of the qubit will only be perturbed slightly by the cavity. Assuming $V_r(t) = V_{r0}\cos(\omega_d t)$ is turned on at time zero, linear response theory tells us:

$$\begin{aligned} \delta \langle Q(t) \rangle &= \frac{1}{i\hbar} \int_0^t \langle [Q_I(t), H'_I(t')] \rangle_0 dt' \\ &= \frac{i}{\hbar} \int_0^t \langle [Q_I(t), Q_I(t')] \rangle_0 V_r(t') dt'. \end{aligned} \quad (6.5)$$

where $\langle \rangle_0$ means the average with respect to the initial thermal equilibrium state.

The commutator in the above expression works out to be:

$$[Q_I(t), Q_I(t')] = \begin{pmatrix} 2iq_x^2 \sin[\omega_a(t-t')] & 2q_xq_z[\exp(i\omega_a t') - \exp(i\omega_a t)] \\ 2q_xq_z[-\exp(-i\omega_a t') + \exp(-i\omega_a t)] & -2iq_x^2 \sin[\omega_a(t-t')] \end{pmatrix}. \quad (6.6)$$

In thermal equilibrium, $\rho \propto \exp(-\frac{1}{2}\beta\hbar\omega_a\sigma_z)$, and $\langle \sigma_x \rangle_0 = \langle \sigma_y \rangle_0 = 0$. Therefore,

$$\langle [Q_I(t), Q_I(t')] \rangle_0 = 2iq_x^2 \sin[\omega_a(t-t')] \langle \sigma_z \rangle_0. \quad (6.7)$$

² q_x/e can be interpreted as the lever arm, which is commonly used in the community.

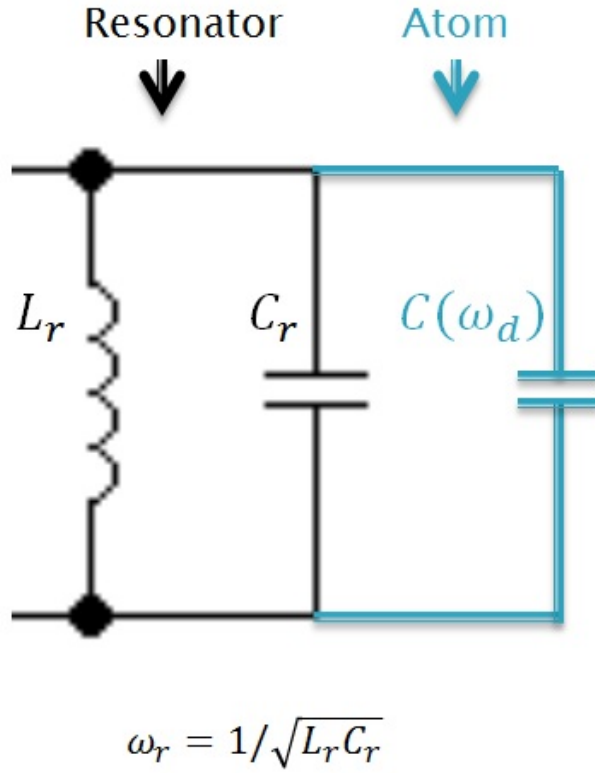


Figure 6.2: Lumped LC model of a resonator coupled to an atom near a high impedance resonance.

We have thus obtained an expression for $\delta \langle Q(t) \rangle$, and we immediately see the cavity perceives the qubit as a capacitance:

$$C(\omega_d) \equiv \frac{\delta \langle Q(\omega_d) \rangle}{V_r(\omega_d)} = \frac{2q_x^2 \omega_a \langle \sigma_z \rangle_0}{\hbar(\omega_d^2 - \omega_a^2)}. \quad (6.8)$$

The sign of this capacitance depends on which state the qubit is in.

In the adiabatic limit where the driving frequency approaches zero, the above capacitance formula becomes

$$C(0) = -\frac{2q_x^2 \langle \sigma_z \rangle_0}{\hbar \omega_a}. \quad (6.9)$$

It agrees with the naive capacitance formula $C = \frac{\partial^2 E}{\partial V_r^2}$, where E denotes an eigenvalue of the qubit Hamiltonian Eq. 6.4 (depending also on the state the qubit is in).³

³We would like to comment here that the naive capacitance formula does not always give the correct result. If we had a quadratic term $\sigma_z V_r^2$ in the qubit Hamiltonian, the naive capacitance formula fails to agree with the correct prediction given by the linear response theory.

Let $\omega_r = \frac{1}{\sqrt{L_r C_r}}$ be the frequency of the bare resonator. The frequency shift due to an additional $C(\omega_d)$ would be

$$\frac{\Delta\omega}{\omega_r} \approx -\frac{C(\omega_d)}{2C_r}. \quad (6.10)$$

We are able to detect this frequency shift in most cavity QED experiments.

Next we will reformulate the cavity QED system in the second quantization picture. Assume a single photon mode ω_r is involved in the resonator. The voltage $V_r(t)$ in Eq. 6.4 becomes the following operator after quantization:

$$V_r = \sqrt{\frac{\hbar\omega_r}{2C_r}}(a^\dagger + a), \quad (6.11)$$

where a is the annihilation operator for the photon modes in the resonator.

We define the detuning of the qubit from cavity by $\Delta = \omega_a - \omega_r$. If $\Delta \ll \omega_r$, we can apply the rotating wave approximation and neglect the highly oscillatory part of the coupling Hamiltonian. Then the Hamiltonian describing the entire system is reduced to the following Jaynes-Cummings model:

$$H_{JC} = \frac{1}{2}\hbar\omega_a\sigma_z + \hbar\omega_r(a^\dagger a + \frac{1}{2}) + \hbar g(a^\dagger\sigma^- + a\sigma^+), \quad (6.12)$$

where the last term represents the coupling between the qubit and photons, and the coupling constant g is

$$g = q_x \sqrt{\frac{\omega_r}{2\hbar C_r}}. \quad (6.13)$$

Let us explore the Jaynes-Cummings Hamiltonian a little further. Although the energy levels can be solved in a closed form [60], we will still use perturbation theory (by treating g as a small constant), which gives us more physical intuition. The eigenstates of the unperturbed Hamiltonian can be written as $|g, n\rangle$ and $|e, n\rangle$, where ‘ g ’(‘ e ’) indicates ground(excited) state of the qubit and n denotes the number of photons in the cavity.

In the case of zero detuning ($\Delta = 0$), the two states with n quanta, $|e, n-1\rangle$ and $|g, n\rangle$, have the same energy in the absence of the coupling. The degeneracy of this n quanta pair is lifted by $2g\sqrt{n}$ in the presence of the coupling, as shown in Fig. 6.3a. The eigenstates become $(|e, n-1\rangle \pm |g, n\rangle)/\sqrt{2}$, which entangle the atom and photons. Rabi oscillations between $|e, n-1\rangle$ and $|g, n\rangle$ will be observed if the initial state is either of these two unperturbed eigenstates. The oscillation between $|e, 0\rangle$ and $|g, 1\rangle$ is called the vacuum Rabi oscillation, which has frequency g/π .

In the dispersive limit where $|\Delta| \gg |g|$, the eigenstates, which are perturbed to first order in g , display a small amount of entanglement between the atom and the photons, while the energies are perturbed to second order in g . It is instructive to apply the dispersive transformation $U = \exp[(a\sigma^+ - a^\dagger\sigma^-)g/\Delta]$ to the Jaynes-Cummings Hamiltonian and keep terms up to second order in g [6]:

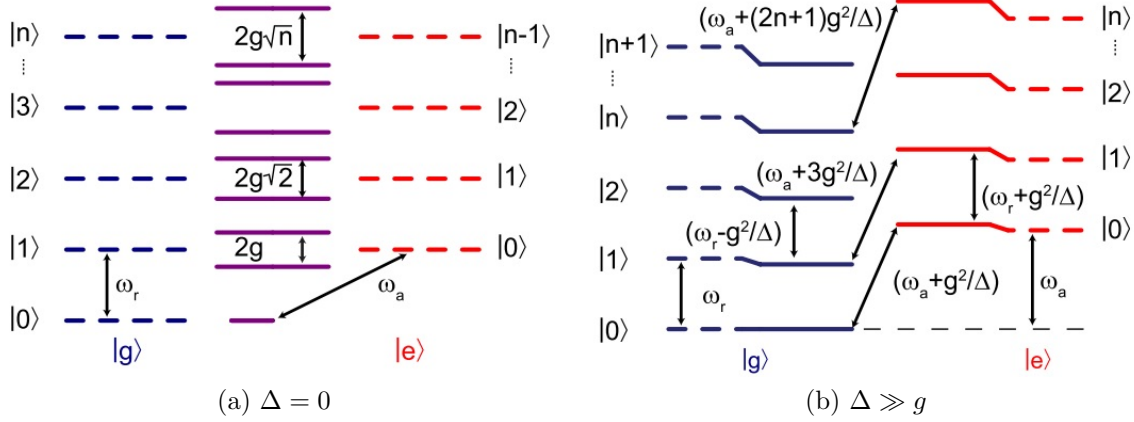


Figure 6.3: Energy spectrum of the Jaynes-Cummings Hamiltonian in (a) zero detuning and (b) large detuning [6].

$$UH_{JC}U^\dagger \approx \hbar(\omega_r + \frac{g^2}{\Delta}\sigma_z)(a^\dagger a + \frac{1}{2}) + \frac{1}{2}\hbar\omega_a\sigma_z. \quad (6.14)$$

This is known as the ‘dressed’ basis and the Hamiltonian is diagonal now! The spectrum can then be interpreted in two ways. i) The cavity shifts the atomic transition frequency by $(n + 1/2)g^2/\Delta$ depending on the number of photons⁴. ii) The atom ‘pulls’ the cavity frequency by $\pm g^2/\Delta$ depending on its energy level. We also note that this shift in the second quantization picture agrees with prediction Eq. 6.10 when $\Delta \ll \omega_r$, the regime for a valid rotating wave approximation.

The nature of the above dispersive coupling allows us to perform quantum non-demolition (QND) measurements of the qubit by probing the photons (and vice versa). In circuit QED, the photon states can be probed by sending in a pulse and measuring the phase of the reflected beam. The frequency response is shown in Fig. 6.4, where the phase interpolates between π and 0 in a frequency window of roughly κ , where κ is the decay rate of the cavity due to the measurement port. Because the state of the qubit changes the effective frequency and therefore the spectrum of the resonator, its state information can be revealed by measurement of the reflected phase. Let us formulate this scheme in the weak measurement language.

In the interaction frame of the photons, Eq. 6.14 can be written as

$$H = H_a + \frac{g^2}{\Delta}a^\dagger a \sigma_z, \quad (6.15)$$

where H_a is the intrinsic Hamiltonian for the atom. Under a measurement pulse that is in resonance with the cavity, the driving Hamiltonian can be written as

$$H_d = iE(a - a^\dagger), \quad (6.16)$$

⁴This effect is called the (AC) Stark shift

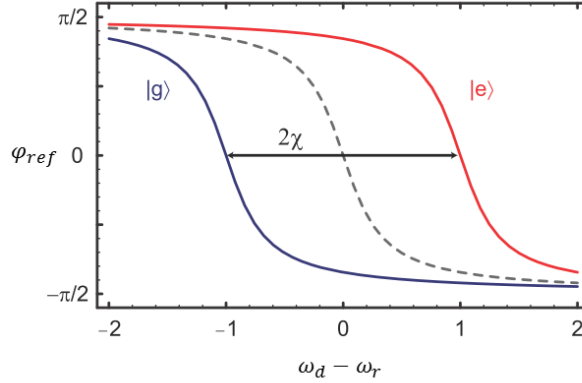


Figure 6.4: State dependent reflected phase of a resonator measurement pulse vs. its angular frequency ($\omega_d - \omega_r$) in the qubit ground (blue) and excited (red) states, as well as the bare resonator spectrum (dashed) [102].

where the amplitude E is related to the power of the pulse P by $\sqrt{\kappa P/\omega_r}$ [24].

Let us perform a homodyne detection of the phase quadrature of the reflected pulse. Then the SME describing the evolution of the atom plus cavity becomes

$$d\rho = -i[H + H_d, \rho] + \kappa \mathcal{D}[a]\rho dt + \sqrt{\eta\kappa} \mathcal{H}[-ia]\rho dW \quad (6.17)$$

This SME is basically the same as Eq. 2.60 in Chap. 2 and so is the derivation. Here, we introduced the measurement efficiency η , which represents the percentage of the photons that are detected by the homodyne apparatus.

In the bad-cavity limit ($\kappa \gg \sqrt{Eg^2/\Delta}$), we can adiabatically eliminate the photon modes and obtain a SME for the atom only (after some lengthy algebra). The adiabatic elimination exploits the fact that high damping makes the cavity dynamics much faster than the atom dynamics, and photons always reach steady states prescribed by the atom. The atomic SME after this treatment becomes [24]:

$$d\rho_a = -i[H_a + \frac{g^2}{\Delta}|\alpha|^2\sigma_z, \rho_a]dt + 2k\mathcal{D}[\sigma_z]\rho_a dt + \sqrt{2\eta k} \mathcal{H}[\sigma_z]\rho_a dW, \quad (6.18)$$

where the effective measurement efficiency $k = 2g^4|\alpha|^2/(\kappa\Delta^2)$, and $\alpha = -2E/\kappa$ gives the coherent state of the cavity, $|\alpha\rangle$, in the absence of the atom. This SME represents exactly a weak σ_z measurement of the qubit whose strength can be tuned by E .

For real systems, we also need to add qubit decoherence processes to the above dynamics. (We will briefly mention these noise channels when we study specific qubit designs in the next two sections.) Let γ be the decoherence rate of the qubit. Strong coupling regime is reached if $g > k$ and $g > \gamma$. It basically means the interaction strength is stronger than the decoherence rates so the characteristic interaction phenomena such as Rabi oscillations can be observed.

6.2 Superconducting Qubits

Superconducting quantum computing is a promising implementation of quantum information technology that involves nano-fabricated superconducting electrodes coupled through Josephson junctions. The amazing non-dissipative flow in superconductors gives macroscopic coherent states that can be used to store quantum information. Non-superconducting quantum states realized so far are all essentially microscopic, and can be much harder to control and measure. Superconducting qubits can be easily coupled to each other and to resonators via electric field [8, 79] or magnetic flux [32], and the DiVincenzo criteria [23] for quantum computing can potentially be satisfied with this implementation. The circuit model of quantum computation, quantum adiabatic computing, and quantum annealing are all being attempted with superconducting qubits. With the help of resonators, we can demonstrate coupling multiple qubits [21], continuous weak measurement [41], creation of flying qubits [48], initial state purification [78], and stabilization of the qubit Rabi state via quantum feedback [118].

Sec. 6.2.1 briefly reviews how superconductors and Josephson junctions work, and in the next few sections we are going to analyze different qubit designs.

6.2.1 Superconductors and Josephson Junctions

A superconducting phase is Bose-Einstein condensates of Cooper pairs. Cooper pairs are bosonic quasiparticles that are composed of two electrons with opposite spins and momenta bound together by phonon mediated electron-electron interaction. The presence of an energy gap Δ in quasiparticle excitations forbids dissipative current flow. According to Ginzburg-Landau theory, the macroscopic coherent state in a superconductor can be described by an order parameter $\psi(\mathbf{r}) = \sqrt{n(\mathbf{r})} \exp(i\phi(\mathbf{r}))$. The order parameter satisfies the Ginzburg-Landau equation, which leads to many correct predictions like the zero magnetic field and electric current inside (i.e., away from the surface of) a superconductor [34].

A Josephson junction consists of two pieces of superconductors separated by a weak tunnel barrier. It is usually represented in a circuit diagram by a crossed square as in Fig. 6.5. Let ϕ be the phase difference between the two superconductor order parameters; let V and I be the voltage and current across the tunnel barrier. The electric property of such a junction is described by the famous Josephson effect:

$$I = I_c \sin \phi, \quad (6.19a)$$

$$\dot{\phi} = \frac{2\pi V}{\Phi_0}. \quad (6.19b)$$

Here the constant I_c is called the critical current, which depends only on the property of the junction, and $\Phi_0 = h/2e$ is the magnetic flux quantum. One can immediately see that a Josephson junction behaves like a non-linear inductor ($V = L_J \dot{\phi}$) with inductance

$$L_J = \frac{\Phi_0}{2\pi I_c \cos \phi}. \quad (6.20)$$

The energy of the Josephson junction can be written as

$$E_J(\phi) = \int V I dt = -E_J \cos \phi, \quad (6.21)$$

where $E_J = I_c \Phi_0 / 2\pi$ is the Josephson energy.

The magnetic flux through a superconducting loop is only allowed to be an integer multiple of the flux quantum, i.e., $\Phi = n\Phi_0$. If the loop is intercepted by one or more Josephson junctions, the flux quantization condition becomes

$$\phi + 2\pi\Phi/\Phi_0 = 2\pi n, \quad (6.22)$$

where ϕ is the total phase drop across all Josephson junctions.

6.2.2 Charge qubits

Let us look at a simple superconducting qubit design called as a Cooper pair box, also known as a charge qubit [8, 79]. A Josephson junction E_J is connected to a capacitor C and biased with a voltage V_g , shown in Fig. 6.5. The Cooper pair box refers to the island indicated by the dotted line.

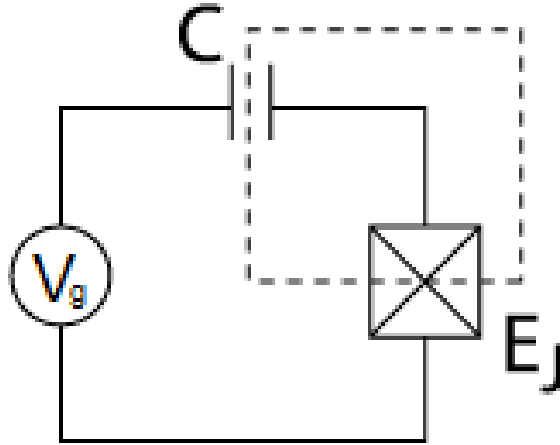


Figure 6.5: Circuit diagram for a charge qubit.

The Lagrangian of the system can be written as

$$\mathcal{L} = E_c(\dot{\phi}) - E_J(\phi) = \frac{1}{2}C(V - \frac{\hbar}{2e}\dot{\phi})^2 + E_J \cos \phi. \quad (6.23)$$

The conjugate momentum for ϕ is

$$p = \frac{\partial \mathcal{L}}{\partial \dot{\phi}} = -\frac{\hbar C}{2e}(V - \frac{\hbar}{2e}\dot{\phi}) = \hbar n, \quad (6.24)$$

where n is the number of Cooper pairs that have tunneled across the junction. Therefore, we enforce the canonical quantization condition

$$[\phi, n] = i \quad (6.25)$$

and write the Hamiltonian for the system as

$$H = p\dot{\phi} - \mathcal{L} = E_C(n - n_g)^2 - E_J \cos \phi, \quad (6.26)$$

where $E_C = 4e^2/2C$ and n_g is the number of Cooper pairs due to the voltage bias.

We note that

$$e^{\pm i\phi} |n\rangle = |n \pm 1\rangle, \quad (6.27)$$

which is a direct consequence of the commutation relation [96]. We can then rewrite the Hamiltonian in the charge basis as

$$H = \sum_n \left[E_C(n - n_g)^2 |n\rangle \langle n| - \frac{E_J}{2} (|n\rangle \langle n+1| + |n+1\rangle \langle n|) \right]. \quad (6.28)$$

We require $E_C \gg E_J$ for a charge qubit. We typically bias the system at the charge degeneracy point $n_g = 1/2$, where the lowest two states $|n=0\rangle$ and $|n=1\rangle$ have the same energy in the absence of the E_J term. Near such a degeneracy point, we can employ the two-level approximation and simplify the Hamiltonian to

$$H \approx -\frac{1}{2}E_C(1 - 2n_g)\sigma_z - \frac{1}{2}E_J\sigma_x. \quad (6.29)$$

At exactly the sweet spot ($n_g = 1/2$), the energy levels are insensitive to n_g to the first order. Therefore charge noise, which means any noise that affects the charge n_g across the capacitor, is suppressed. However, dephasing due to second order charge noise may still be strong [61].

We can couple the charge qubit to a resonator via an additional capacitor C_g , where the charge n_g is determined by the voltage across the resonator electrodes. The total Hamiltonian for the entire system can be found in Ref. [6].

6.2.3 Phase qubits and Flux qubits

The circuit diagram for a phase qubit is shown in Fig. 6.6a, and we require $E_C \ll E_J$. (Typically $E_J/E_C \sim 10^4$.) R models the dissipation of the system and is ignored for now. The circuit is biased with an external current I . The Hamiltonian of the system can be written as

$$H = -E_C \partial_\phi^2 - E_J \left(\cos \phi + \frac{I}{I_c} \phi \right) \quad (6.30)$$

in the phase space [136]. This represents the Hamiltonian of a quantum particle in a tilted washboard potential shown in Fig. 6.6b. We will bias I at a little bit below the critical current

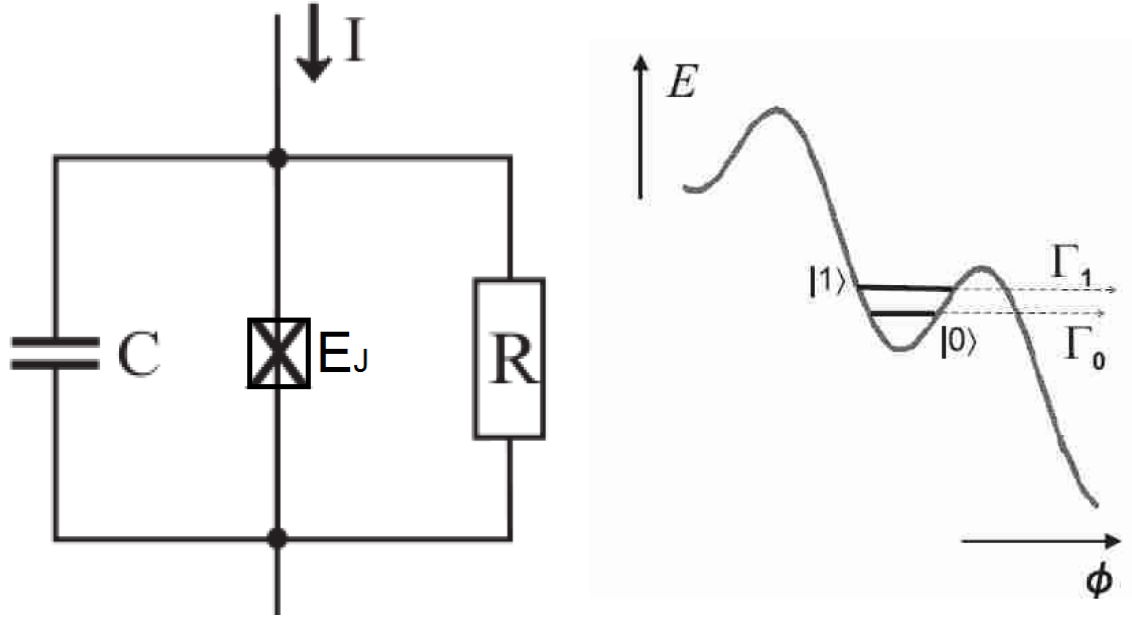


Figure 6.6: (a) Circuit diagram and (b) washboard potential for a phase qubit [136].

I_c (typically $0.95I_c$ - $0.98I_c$) so there remain only a few quantized energy levels around each local minimum [136]. This choice of bias makes sure the potential is very anharmonic and the energy levels are non-equidistant. The tunneling out of the first two levels in a given potential through the barrier is still small enough that they can be taken as qubit states [136]. The qubit can be controlled by adding an oscillatory component to the bias current. A phase qubit has weak sensitivity to charge and flux noise by design.

The circuit diagram for a typical flux qubit is very similar to the charge qubit except that we remove the voltage bias and add a flux Φ_x through the loop, taking into account the self-inductance L of this (Fig. 6.7a) [32]. A flux qubit also works in the $E_C \ll E_J$ regime. The Hamiltonian can be written in the phase basis as [136]

$$H = -E_C \partial_\phi^2 - E_J \cos \phi + E_L (\phi - \phi_x)^2 / 2. \quad (6.31)$$

Here $\phi_x = 2\pi\Phi_x/\Phi_0$ is the reduced flux through the loop and $E_L = \Phi_0^2/4\pi L$ is the inductive energy scale. If $\phi_x = \pi$, the potential energy exhibits a symmetric double well shape and has two degenerate local minima (Fig. 6.7b). These two minima correspond to persistent circulating currents in opposite directions. They form a qubit space well-separated from higher energy levels. At the exact $\phi_x = \pi$ sweet point, true energy eigenstates are equal superpositions of the states with oppositely circulating currents and are insensitive to magnetic field fluctuations. A flux qubit has low sensitivity to charge noise and medium sensitivity to critical current noise by design.

There is also an alternative design for a flux qubit that involves a superconducting loop with negligible inductance but three Josephson junctions, shown in Ref. [119].

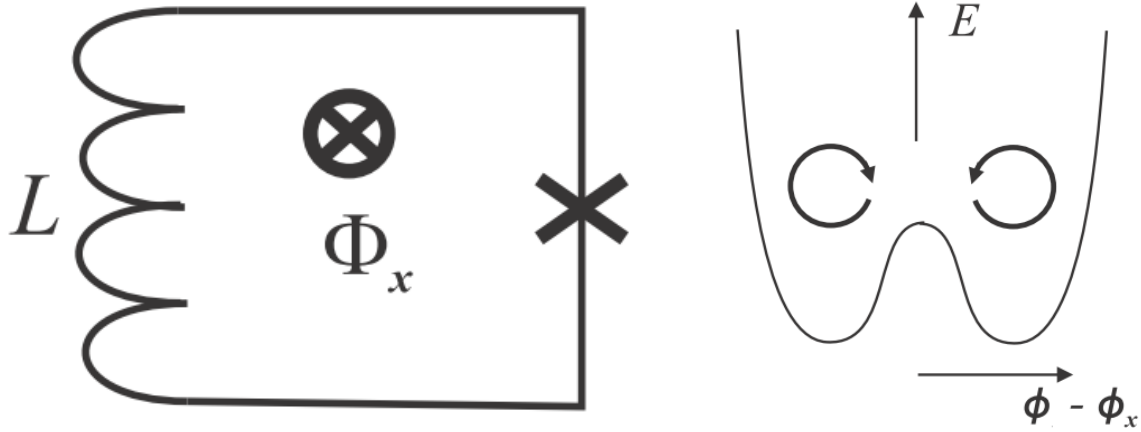


Figure 6.7: (a)Circuit diagram and (b)double well potential for a flux qubit [136].

6.2.4 Transmon qubit

The circuit diagram for a transmon qubit is the same as that for the charge qubit but with $E_C \ll E_J$. The Hamiltonian for the system is again described by Eq. 6.26. Its spectrum as a function of n_g is shown in Fig. 6.8. We pick the sweet spot $n_g = 1/2$ to operate the qubit around as usual.

Although small charge noise is suppressed near the sweet spot, large charge fluctuation is always present and is directly related to the energy dispersion relation [61]. In particular,

$$\epsilon_m \equiv E_m(n_g = 1/2) - E_m(n_g = 0) \quad (6.32)$$

gives the peak-to-peak value for the charge dispersion of the m th energy level [61]. In the large E_J/E_C limit, it can be approximated by [61]

$$\epsilon_m \simeq (-1)^m E_C \frac{2^{4m+5}}{m!} \sqrt{\frac{2}{\pi}} \left(\frac{E_J}{2E_C} \right)^{\frac{m}{2} + \frac{3}{4}} e^{-\sqrt{8E_J/E_C}}, \quad (6.33)$$

which decreases exponentially with $\sqrt{E_J/E_C}$.

In order to operate the transmon as a qubit, we need a reasonably large anharmonicity. The relative anharmonicity is defined as [61]

$$\alpha_r = \frac{E_{12} - E_{01}}{E_{01}} \quad (6.34)$$

evaluated at $n_g = 1/2$. In the large E_J/E_C limit, it can be approximated by [61]

$$\alpha_r \approx -(8E_J/E_C)^{-1/2}. \quad (6.35)$$

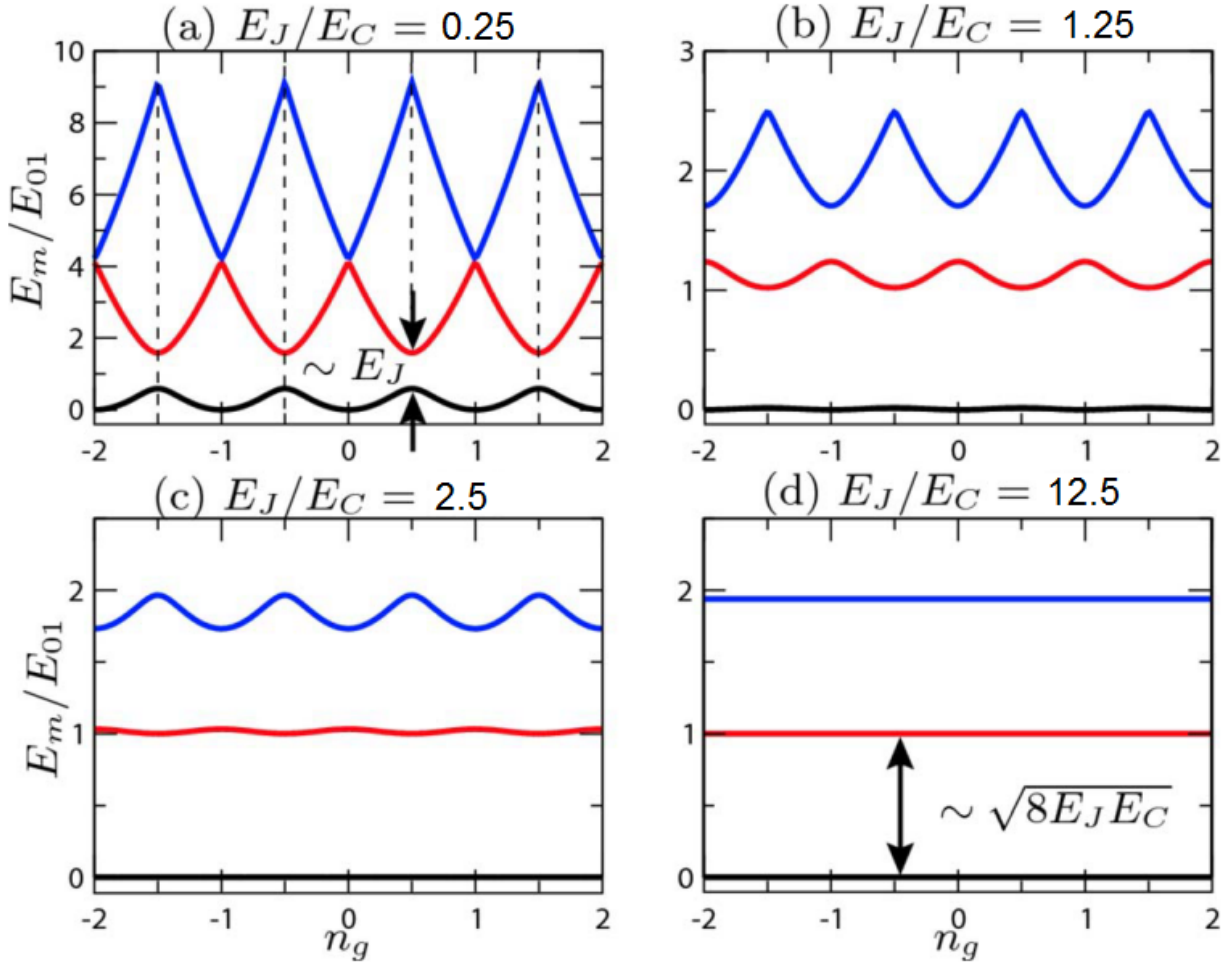


Figure 6.8: Eigenenergies E_m (first three levels, $m=0,1,2$) of the qubit Hamiltonian Eq. 6.26 as a function of the effective offset charge n_g for different ratios E_J/E_C [61].

Now we come to the central idea behind a transmon qubit design. The exponential decrease of charge fluctuation and power law decrease of anharmonicity with E_J/E_C allows us to achieve a relatively small charge sensitivity and relatively large anharmonicity with a medium large E_J/E_C (typically around 10^2). Also, when the transmon qubit is charge coupled to a resonator, the coupling strength goes like $(E_J/E_C)^{1/4}$ [61], which can be tuned strong enough for control and measurement.

Ref. [61] showed that the circuit QED system with a transmon qubit can be approximated by Eq. 6.14 in the dispersive limit.

6.2.5 Summary

Transmon qubits have excellent performance. Upto 2012, transmons in 3D cavities have been fabricated with coherence times approaching $100\mu s$, which could fit in $10^3 - 10^4$ quantum operations (assuming $10 - 100ns$ single-qubit and two-qubit gate time.) [103, 95]. There are a number of other innovative qubit designs like quantronium, fluxonium, and hybrid qubits that are also very promising. For superconducting qubits, we are in a stage where simple QND measurements and error correction can be performed and we are aiming at implementing logical memory with longer lifetime than physical qubits [20]. Although much advancement in science and technology is still needed, there seems to be no physical principle that may bound the scalability of superconducting qubits.

6.3 Quantum Dot Qubits

The ability to trap individual electrons in semiconductor quantum dots has lead to great progress towards enabling full quantum manipulation of their charge and spin in nanoscale solid state devices [125, 40, 137]. In particular there has been much interest in realizing charge [42, 105, 123] and spin qubits [40, 137, 87, 73] in lateral double quantum dots due to the ability to tune the qubit energy splitting via an electrostatic gate controlling the tunnel coupling between the individual quantum dots [125, 42]. Readout of quantum dots has traditionally been performed by direct current transport measurements, either through the double quantum dots [125], or by using an auxiliary current-biased quantum point contact (QPC) to monitor the charge state [40, 137]. More recently, embedding the QPC in a LC tank circuit with a resonant frequency of $\sim 100-400$ MHz has enabled faster, single-shot readout by non-dispersively monitoring the loss on resonance [137, 94]. In this section, I will briefly describe the theory behind charge and spin qubits.

6.3.1 Charge qubits

A lateral quantum dot utilizes semiconductor heterostructures and lithographically patterned gate electrodes to create a electron confinement potential in 3D. Fig. 7.2 shows the layout of a lateral double quantum dot designed in UC Berkeley. A typical double well potential is shown in Fig. 6.9.

For computational purpose, charge states can be labeled by (n_L, n_R) , where n_L and n_R denotes the number of electrons in the left and right dots. The charge states are electric dipole coupled to the resonator. For both experimental and theoretical simplicity, we choose a qubit space spanned by $(0, 1)$ and $(1, 0)$ states of a single electron. The energy eigenstates of qubit, $|\psi_-\rangle$ and $|\psi_+\rangle$, are superpositions of $(0, 1)$ and $(1, 0)$.

Physically, the Hamiltonian for a single electron confined by a static potential $V_0(\mathbf{r})$ can be written as

$$\hat{H}'_0 = \frac{p^2}{2m} - eV_0(\mathbf{r}). \quad (6.36)$$

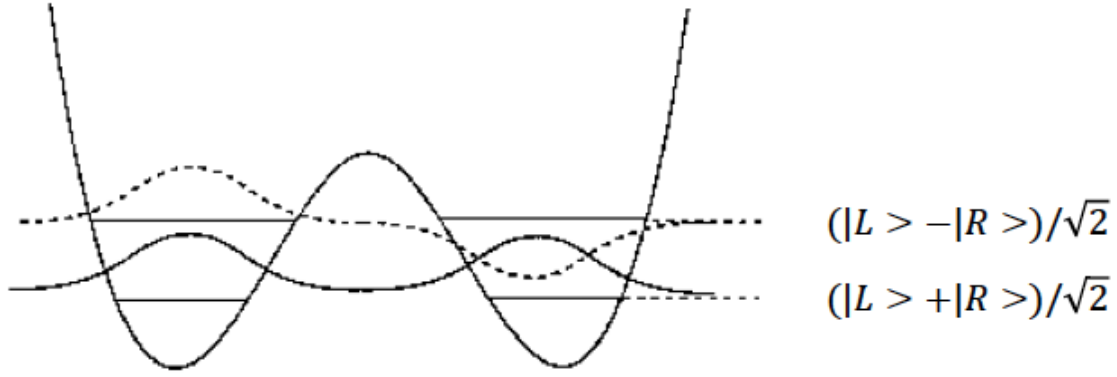


Figure 6.9: A double well potential and its lowest energy states.

$|\psi_-\rangle$ and $|\psi_+\rangle$ are in fact the lowest two eigenstates of this Hamiltonian (see the next chapter for a numerical example). Let $\hbar\omega$ be the energy splitting between them.

Let $V_r(t)$ be the AC voltage across the two resonator electrodes as usual. $V_r(t)$ sets an electric potential $V(\mathbf{r}, t)$ across the dot region, and the electron feels the perturbation $\hat{H}' = -eV(\mathbf{r}, t)$. If we project the full Hamiltonian, $\hat{H}_0 + \hat{H}'$, onto the qubit subspace, we obtain Eq. 6.4 with

$$q_0 = \frac{1}{2V_r(t)} \left(\langle \psi_+ | \hat{H}'(t) | \psi_+ \rangle + \langle \psi_- | \hat{H}'(t) | \psi_- \rangle \right), \quad (6.37a)$$

$$q_x = \frac{1}{V_r(t)} \langle \psi_+ | \hat{H}'(t) | \psi_- \rangle, \quad (6.37b)$$

$$q_z = \frac{1}{2V_r(t)} \left(\langle \psi_+ | \hat{H}'(t) | \psi_+ \rangle - \langle \psi_- | \hat{H}'(t) | \psi_- \rangle \right). \quad (6.37c)$$

Because we can always choose real wavefunctions for the electrons, there is no σ_y component, and q_0 , q_x , and q_z are taken to be real. It is clear that $\hat{H}'(t) \propto V_r(t)$, so these q coefficients only depend on the geometry and the material, but not on time.

The coupling strength and the resonator frequency shift can then be calculated with the method described in Sec. 6.1. The maximal coupling strength g achievable from this electric dipole interaction is on the order of tens of MHz for a typical circuit-QED setup. Please refer to Sec. 7.3 for detailed calculation in a specific case.

Charge states are subject to strong decoherence due to the electron-phonon coupling. The decoherence rates are estimated to be tens to hundreds of MHz [86, 42], which makes it very difficult to protect quantum information. The coupling between charge states and resonators have been demonstrated with GaAs/AlGaAs quantum dots, but there is no conclusive evidence that the strong coupling regime is achieved in this system [30, 114, 120].

6.3.2 Spin qubits

Spin states generally enjoy much longer coherence time than charge states and they are a very promising candidate for quantum information processing. Two most popular implementations are single electron spin qubits and singlet-triplet qubits. We will follow Nori's analysis [50] and see how a single electron spin in a quantum dot can be coupled to photons in a resonator.

We would like to have the spin to be electrically instead of magnetically coupled to the resonator because the direct magnetic dipole coupling strength is very weak ($\sim 100\text{Hz}$ at best [100], and much weaker than the electric coupling estimated in the previous section). However, the electric field is naturally decoupled from the spin degree of freedom, and we need to somehow mix spin and spatial degrees of freedom before we can achieve this coupling.

To use a single spin qubit in a double quantum dot, an external in-plane strong magnetic field is used to split the spin degeneracy. In addition, we either apply a non-uniform local magnetic field or utilize the spin-orbit coupling in GaAs/InAs to achieve the mixing. The former scheme can be realized by integrating a micro-meter size ferromagnet on top of the double quantum dot device, resulting in a stray magnetic field that has a position dependent out-of-plane component (Fig. 6.10) [88, 89].

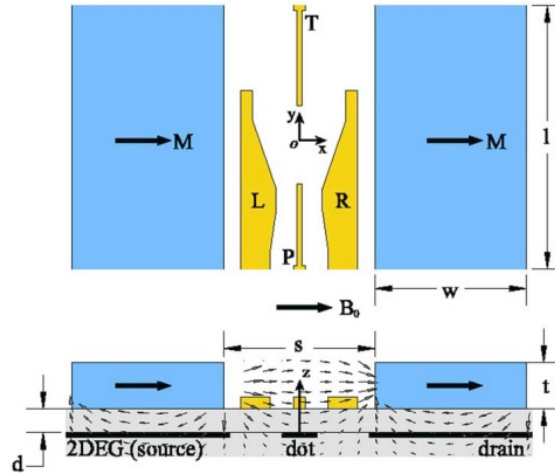


Figure 6.10: Top and cross-sectional views of a lateral quantum dot device consisting of four metallic gates (yellow, labeled L, P, R and T) and two ferromagnetic strips (blue) patterned at the surface of a semiconductor heterostructure developed at Tarucha's group. The thick arrows indicate the direction of the external magnetic field B_0 and magnetization M . The origin is fixed to the quantum dot position. [88]

The Hamiltonian describing the electron in the absence of the resonator coupling can be written as [50]

$$H_0 = H_{DQD} + H_Z + H_{SO}, \quad (6.38)$$

where H_{DQD} is due to the dot confinement potential, $H_Z = \frac{1}{2}g\mu_B\mathbf{B} \cdot \boldsymbol{\sigma}$ is the Zeeman energy, and H_{SO} is the spin orbit mixing Hamiltonian. Also, $\hat{H}' = -eV(\mathbf{r}, t)$ describes the Hamiltonian due to the AC voltage across the resonator electrodes as usual.

Let xy -plane be the heterostructure interface and x axis be the direction where the quantum dot is elongated. The mixing Hamiltonian can be expressed as [50]

$$H_{SO} = \frac{\alpha_{BR}}{\hbar}(\sigma_x P_y - \sigma_y P_x) + \alpha_I \sigma_z x \quad (6.39)$$

where the first term represents the Rashba spin-orbit coupling [93] and the second term presents the effect of the inhomogeneous magnetic field whose gradient is roughly uniform [89].

Let us assume the energy scale of H_Z is smaller than H_{DQD} . The two lowest energy eigenstates of H_0 in the absence of H_{SO} can be written as $|g, \downarrow\rangle$ and $|g, \uparrow\rangle$. The presence of H_{SO} perturbed the true eigenstates states, $|\psi_-\rangle$ and $|\psi_+\rangle$, from $|g, \downarrow\rangle$ and $|g, \uparrow\rangle$. As a result of the spin-orbit mixing in $|\psi_-\rangle$ and $|\psi_+\rangle$, q_x in Eq. 6.37, which is responsible for the spin-photon coupling, is non-zero.

Nori calculated the coupling strength employing the four-state approximation [50]. Let L be the interdot distance, a be the radius of the single dot ground state wave function, and S be the wavefunction overlap between the left and right dot. The spin-orbit coupling parameter is defined as

$$\lambda_x = \frac{\alpha_{BR}LS}{a^2\sqrt{1-S^2}} \quad (6.40)$$

and the spin-resonator coupling strength works out to be [50]

$$g \approx -2eEL\left(\frac{i\alpha_I L}{\epsilon_0} + \frac{\lambda_x \epsilon_Z}{\epsilon_0^2}\right), \quad (6.41)$$

where E is the vacuum electric field in the dot regime, and ϵ_Z is the Zeeman energy.

With the above formula, the spin-resonator coupling strength due to the inhomogeneous field is estimated to be around 0.5MHz for both Si and GaAs/InAs quantum dots, while the strength due to Rashba coupling is around 50kHz for GaAs and 1MHz for InAs [50]. However, the environmental nuclear spins generally cause significant inhomogeneous broadening in III-V quantum dots and strong coupling is hard to achieve. In isotopically enriched Si, however, electron spin decoherence rates on the order of 1Hz have been experimentally observed [116]. Although the spin-orbit coupling results in additional decoherence due to phonons, it is estimated to be much smaller than the coupling strength 0.5MHz [50, 88]. Therefore, a Si quantum dot with an inhomogeneous magnetic field can potentially achieve the strong coupling regime and appears to be a feasible way to go forward [50].

Chapter 7

A Prototype Circuit QED with Double Quantum Dot

7.1 Introduction

¹This chapter describes a unique design for a microwave resonator coupled double quantum dot in Si, with the goal of integrating the cQED architecture with semiconducting qubits. The design and fabrication of the quantum dot was performed by Cheuk Chi Lo and Steven Wang under the supervision of Eli Yablonovich and Jeffrey Bokor at UC Berkeley. The resonator and measurement circuit was developed by Andrew Schmidt and Edward Henry under the supervision of Irfan Siddiqi. I performed the numerical simulation of the physical system, presented in Sec. 7.3.

The coupling is very similar to that reported in previous resonator-coupled GaAs/AlGaAs double quantum dots [30, 114], with the resonator conductors connected to the double dot plunger gates so that the microwave voltage directly couples to the Fermi levels, and hence the charge states, of the dots. Our quantum dot is an electrostatically gate defined, silicon metal-oxide-semiconductor (MOS) structure utilizing accumulation mode field effect to create a two-dimensional electron gas (2DEG). This allows for lithographically fabricated accumulation gates to determine where the 2DEG will exist in the substrate and keep it spatially decoupled from the microwave resonator, limiting high frequency loading from the 2DEG conductivity and capacitance. In contrast, the chemically defined 2DEG in GaAs/AlGaAs heterostructures must be etched away before fabricating the resonator. Using Si also eliminates piezoelectric acoustic phonon coupling [135] which has been implicated in loss and limiting coherence times in GaAs/AlGaAs devices [42, 114, 120]. Finally, Si has the potential for long spin coherence due to small spin-orbit coupling [137, 135] and the possibility to eliminate the nuclear spin bath by isotopic purification [117]; singlet-triplet spin qubits in Si/SiGe [73] without purification have T_2^* an order of magnitude longer than in the typical GaAs [87] devices.

¹The bulk of this chapter is adapted from Ref. [99].

While the double-dot/resonator coupling is via the qubit electric dipole moment, the ultimate goal is to couple the semiconductor electron spin degrees of freedom to the resonator. In ^{28}Si , electron spins have lifetimes approaching $\sim 1\text{s}$ [137, 132, 117, 75]. At an estimated coupling rate of $\sim 100\text{ Hz}$ [100], directly coupling the electron spin magnetic field to the resonator is nearly impossible for cQED. Instead, our design would employ electric dipole spin resonance (EDSR) [97, 81, 89], using a strong magnetic field gradient [89] to couple an electron spin to the resonator. Using EDSR in this manner to couple a spin in a semiconductor double quantum to a microwave resonator has been analyzed in ref. [50], where the authors found that isotopically purified silicon is the only material capable of achieving the strong coupling limit of cQED. The precise technique to add the field gradient is itself not a trivial fabrication process and is left for future work. The first steps towards using EDSR to couple the spin to a microwave resonator have recently been demonstrated by using the microwave resonator to readout the spin state of a double quantum dot in InAs nanowires via strong spin-orbit EDSR [85].

The layout of this chapter is as follows. In Section 7.2 describes the device geometry and fabrication details. In Section 7.3 discusses the numerical simulations that were used to guide device design. Section 7.4 contains the results of experimental characterization of device functionality and Section 7.5 contains a brief summary and conclusions.

7.2 Device Layout and Fabrication Process

Fig. 7.1 is an optical image of our resonator-coupled double quantum dot at the largest length scales of the device. The short dashed blue box outlines the microwave resonator, which is a shorted, 6 GHz quarter-wavelength section of coplanar stripline (CPS). The long dashed green box outlines the shorting termination. This is actually a $\sim 50\text{ pF}$ capacitor which is a short at 6 GHz, but is an open at low frequencies allowing us to individually DC bias each resonator conductor. This is distinct from refs [30, 114], which do not use the resonator conductors to apply DC biases. At the electric field antinode, the resonator conductors become the left and right plunger gates of each quantum dot, which are within the solid red box. The ‘X’ shaped structure within this box are the two metal-oxide accumulation gates beneath which the 2DEG is located at the semiconductor-oxide interface. These gates are labeled T_R and T_L in Fig. 7.2a. This is a standard MOS geometry with mobile electrons for the 2DEG coming from the n -type degenerately doped ohmic contacts. A positive bias on these gates accumulates the 2DEG. The ohmic contacts are labeled 1-4 in Fig. 7.1. RF_1 and RF_2 are the wire bond pads for the microwave carrier, which is coupled to the resonator via finger capacitors and differentially excited with a 180° microstrip ring hybrid. This differential excitation puts the full resonator voltage drop across the two plunger gates, so that the Fermi level in one dot oscillates in the direction opposite to the Fermi level in the other dot. These bond pads are large to minimize inductance. Also visible in the figure are several aluminum wire bonds. They are attached to a much smaller set of bond pads for the DC biases. The thin size of the leads from these pads to the rest of the device is to increase

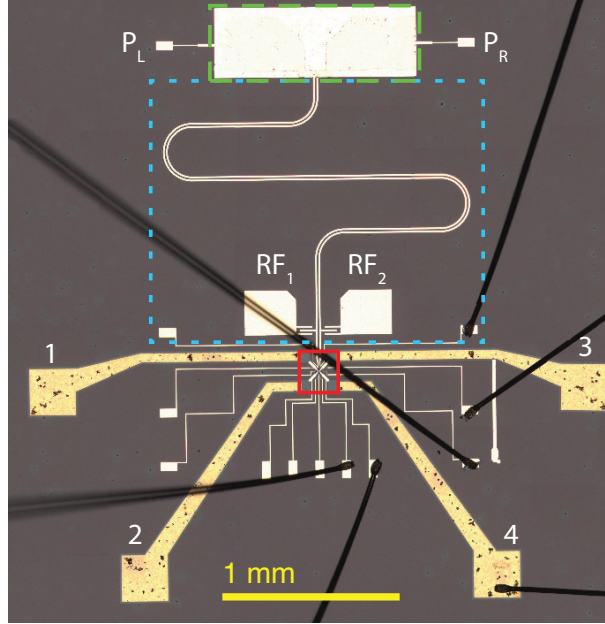


Figure 7.1: (color online) Large scale view of the device. The electron confinement gates are located within the red solid box and are not visible on this scale. The ‘X’ within this box are the two accumulation gates creating the 2DEG. Inside the short dashed blue box lies the CPS resonator and the coupling capacitors for the microwave wire bond feed. Within the long dashed green box lies the $\sim 50\text{pF}$ shunting capacitor that is the bias tee combining the DC P_L and P_R bias voltage with the microwave carrier.

the series inductance and choke out any residual high frequency noise.

Fig. 7.2a shows a SEM micrograph image of the accumulation metal-oxide gates, false-colored in red and labeled T_R and T_L , that determine the location of the 2DEG in the vicinity of the quantum dot electron confinement gates. The resonator conductors are false colored-blue and are also the plunger gates for the two dots, P_L and P_R . The resonator conductors are well decoupled from the 2DEG as shown by the spatial separation in this figure. The inset focuses on these confinement gates, with a length scale very similar to that successfully used in previous Si quantum dots [105, 115, 49].

The confinement gates are a mostly standard set of quantum dot confinement gates; however, the plunger gates controlling the dot charge states are unique in that they are operated in accumulation mode at positive bias. Their vertical orientation should reduce the capacitive division of the applied bias, as observed in another Si MOS double quantum dot with accumulation mode plunger gates [63]. This should help maximize the coupling of the ground state quantum voltage fluctuations of the resonator differential mode into the double dot. The depletion side gates are labeled $L_{T,B}$ and $R_{T,B}$, and the U gate controls the tunnel coupling between the left and right dots. The QPC gates are $Q_{L,R}$.

Other than Ref. [63], the plunger gates in Si MOS and Si/SiGe double quantum dots that

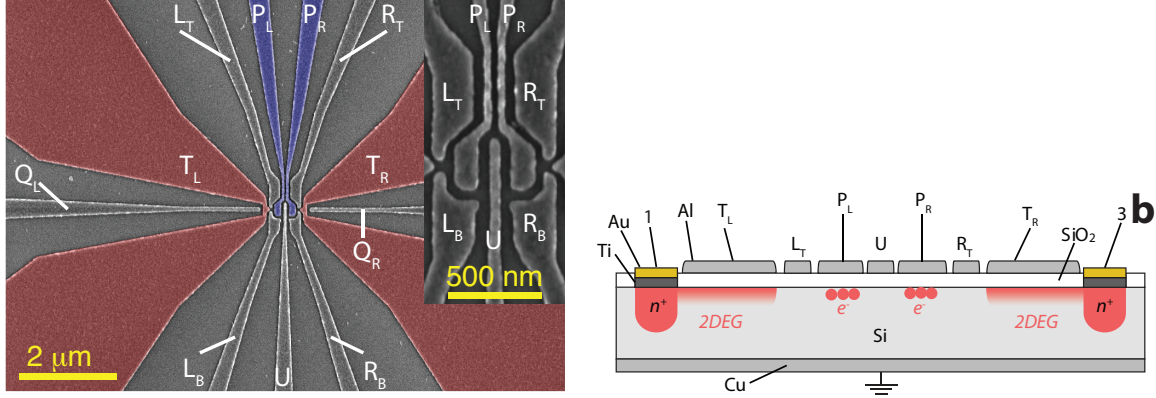


Figure 7.2: (color online) **(a)** SEM of the electron confinement gates and the 2DEG accumulation gates, which are false colored red. The plunger gates P_R and P_L are false colored blue, and emphasize the spatial decoupling of the microwave resonator from the 2DEG. The inset SEM details the electron confinement gates. **(b)** A schematic cross section of the MOS accumulation structure in this device. (not to scale)

we are aware of operate in depletion mode. We do not use a global top gate to accumulate the 2DEG like other existing Si device designs [137, 123, 73, 132, 115, 49, 133], because we cannot have this top gate overlap with the plunger gates, or the quantum dots. The plunger gates are also the microwave resonator conductors, and if the plunger and top gates overlapped this would not only lead to resistive loss by the reservoir electrons, but also create an additional capacitive load, both severely degrading resonator performance. A global top gate that is deposited to be non-overlapping would first require depositing an insulating oxide layer followed by an additional metal layer that is aligned with nanometer scale precision above the quantum dot gates, resulting in additional fabrication complexity.

The devices are fabricated from commercially available Si wafers from Topsil that are float-zone grown in the $\langle 100 \rangle$ orientation, n -type with room temperature resistivity in excess of 10 k Ω -cm. Fabrication begins with ion-implantation of the phosphorous donors in the ohmic contact regions. These must be degenerately doped beyond the metal-insulator transition to ensure device operation below liquid He temperatures. This is followed by creation of the 100nm thick SiO_2 gate oxide barrier by dry thermal oxidation at 1000°C. Next, this oxide on the ohmic contacts is etched away with hydrofluoric acid (HF) and metal contacts are deposited consisting of 5nm Ti on the bare Si surface and 40nm Au on top for the wire bond pads. After this is the electron-beam write for the metal lithography, defining the gates, resonator conductors, metal leads and wire bond pads. With the exception of the ohmic contacts, all other metal is 20nm thick Al deposited in a custom built electron-beam evaporator designed for fabrication of superconducting qubits [78, 118]. Finally the shunting capacitor is finished with 200nm thick plasma enhanced chemical vapor deposited (PECVD) SiO_2 dielectric and a 50nm thick Al upper capacitor plate. A schematic cross section of the device, showing the metal-oxide structures but excluding the shorting capacitor is shown in

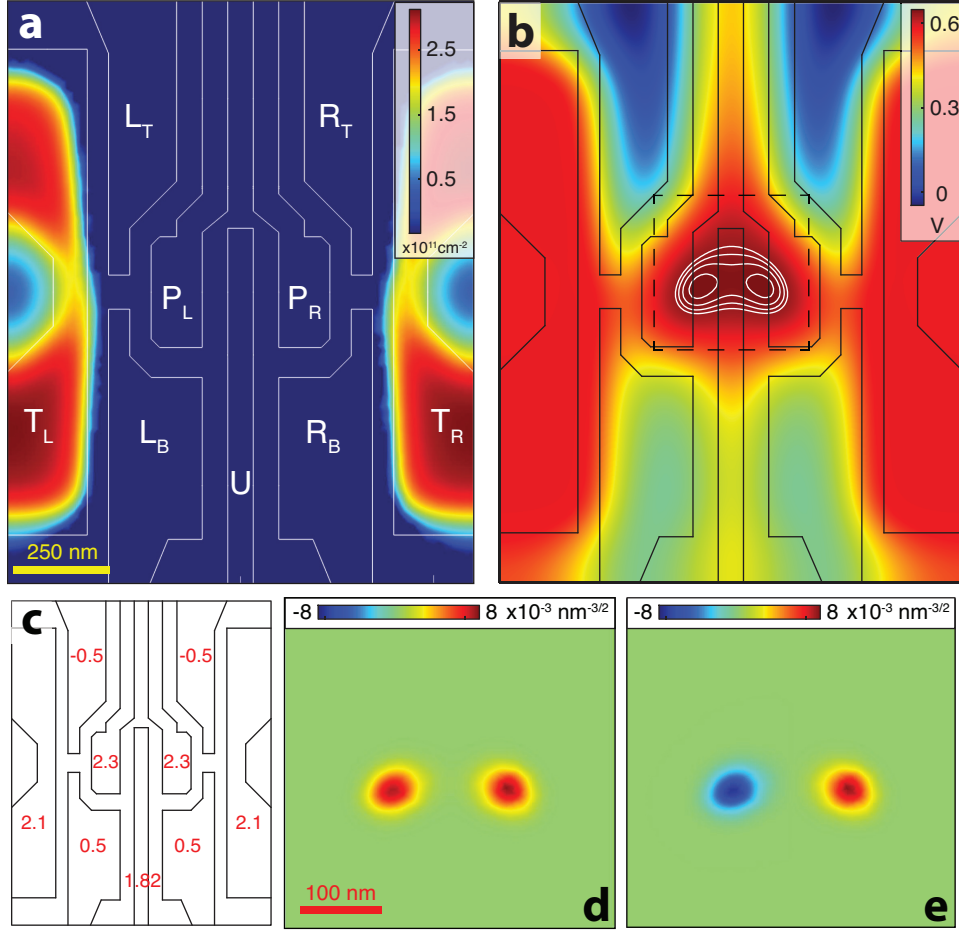


Figure 7.3: (color online) Numerical simulations (see text for details) **(a)** 2DEG induced at the Si-SiO₂ interface **(b)** Interface electrostatic potential. **(c)** Applied gate bias voltages setting boundary conditions. **(d)** Ground state wave function envelope for the region in the black dashed box in (b). **(e)** First excited state wave function envelope.

Fig. 7.2b, emphasizing that all the confinement and accumulation gates are defined in a single metal layer. The final step is a forming gas anneal to reduce the interface trap density.

Similar MOS devices built using these fabrication techniques are measured to have a mobility of 10,000 -15,000 cm²/V s at 4.2K [65]. This is comparable to previous Si MOS quantum dots [132, 137].

7.3 Numerical Simulations

To simulate the device we first find the electrostatic confinement potential for an electron by numerically and self consistently solving Poisson's equation with the accumulated 2DEG charge density given in the semiclassical Thomas-Fermi approximation [2, 51]:

$$\begin{aligned}\nabla \cdot (\kappa \nabla \phi(\mathbf{r})) &= -4\pi \rho_{2DEG}(\mathbf{r}) \\ \rho_{2DEG}(\mathbf{r}) &= -e \frac{m_t^*}{\pi \hbar^2} (E_F - E_0) \delta(z) & E_F > E_0 \\ \rho_{2DEG}(\mathbf{r}) &= 0 & E_F < E_0\end{aligned}$$

Here κ is the material-dependent dielectric constant, $\phi(\mathbf{r})$ is the electrostatic potential, ρ_{2DEG} is the 2DEG charge density, m_t^* is the Si transverse electron effective mass, E_F is the Fermi energy, and E_0 is the energy of the bottom of the lowest 2DEG subband. The Si-SiO₂ interface is at $z = 0$ and perpendicular to the z direction, and by using $\delta(z)$ we are ignoring the spatial extent of the wave function in the direction of confinement. Since field-effect 2DEGs in Si-SiO₂ are typically within ~ 5 nm of the interface and are of the same order in extent [2], this is a very good approximation. The space, oxide, and interface charges are ignored, as are issues of valley physics. The final valley degeneracy is lifted by the electric field and the interface, but the magnitude of the splitting depends very sensitively on the atomic-level interface details [2, 137, 133]. Thus we are using a free electron envelope function description of the electron wavefunction. E_0 implicitly depends on $\phi(\mathbf{r})$, essentially because the gate bias must bend the conduction band below E_F before the 2DEG can form. The result is that a threshold bias V_T [2, 111] must be applied before the 2DEG forms; this was measured to be 1.2-1.4 V before transport occurs in our devices. The commercial program COMSOL Multiphysics was used [77] for the numerical solution. The resulting 2DEG density is shown in Fig. 7.3(a) for the applied gate bias boundary conditions shown in Fig 7.3(c).

The resulting electrostatic potential at the Si-SiO₂ interface is shown in Fig. 7.3(b). The thin white lines in this figure are equipotential lines with 5 mV spacing, and we find electrostatic potential maxima below the two plunger gates P_{L,R}. Multiplying by the electron charge $-e$, these become potential energy minima of ~ 20 meV for confining electrons in the quantum dots. The double quantum dot ground and first excited state energies and wave function envelopes are found within the effective mass approximation [2, 51] by subsequently using COMSOL to numerically solve Schrödinger's equation with this electrostatic potential energy, again using the anisotropic effective mass of silicon. The ground state wave function envelope is shown in Fig. 7.3(d) for the region within the black dashed line in Fig. 7.3(b), and shows the bonding symmetry. The first excited state envelope for the same region is shown in Fig. 7.3(e). This clearly shows the anti-bonding symmetry. The energy difference between ground and first excited state is 3 GHz. This number is a rough order of magnitude estimate, and we anticipate that fine tuning of the U gate will be required to set the desired operating point.

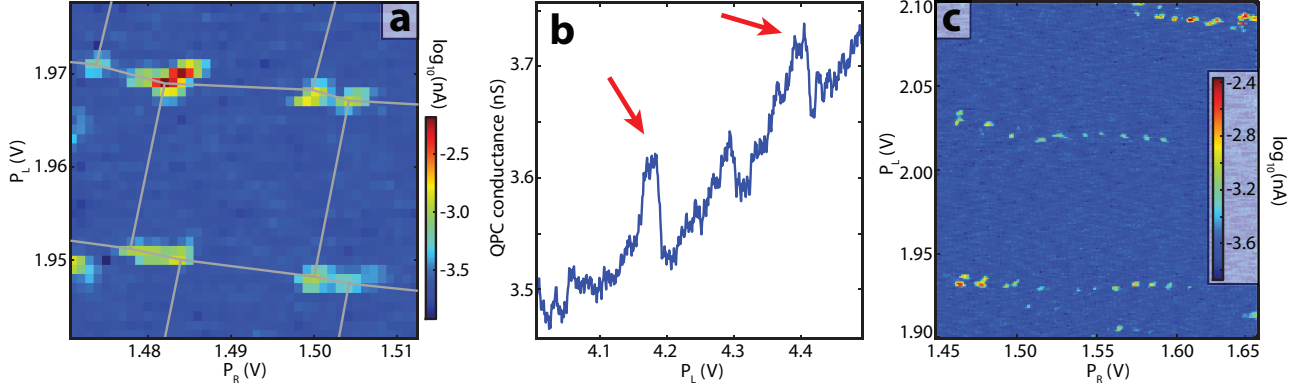


Figure 7.4: (color online) Transport characterization of electron confinement. **(a)** Current resonances as function of plunger gate bias forming honeycomb charge stability regions. **(b)** QPC conductance as a function of left plunger gate bias showing single electron charging events (arrows). **(c)** Inconsistent honeycombs over large plunger gate bias ranges.

At the charge degeneracy point, the Jaynes-Cummings Hamiltonian with qubit frequency ω_a , resonator frequency ω_r , and qubit-resonator coupling g is

$$H_{JC} = \frac{1}{2}\hbar\omega_a + \frac{1}{2}\hbar\omega_r a^\dagger a + \hbar g(a^\dagger \sigma_- + a \sigma_+).$$

Here, a^\dagger creates a resonator photon, and $\sigma_{+/-}$ are the qubit Pauli operators. g is given by Eq. 6.13, reproduced below:

$$g = q_x \sqrt{\frac{\omega_r}{2\hbar C_r}}. \quad (7.1)$$

Aforementioned simulation with the confining potential and electron wavefunction produces $q_x \approx 10^{-21} - 10^{-20}[C]$. Our resonator can be modeled with $L_r = 1.7\text{nH}$ and $C_r = 0.42\text{pF}$, which gives maximally achievable coupling strength $g/\hbar \approx 10\text{MHz}$ for a single electron in the dot. Also, at charge degeneracy, this coupling term g is the roughly same for both charge double quantum dot and Cooper pair box qubits [6, 12] with similar geometry. A g/\hbar value of 10-50 MHz is observed for charge coupling in III-V double quantum dots [30, 114, 85], the same order of magnitude as observed for Cooper pair boxes [121, 48]. Because both III-V and Si double quantum dots have similar $\alpha = q_x/e$ [115, 49, 63, 7, 31, 114, 101] and similar C_r and ω_r owing to similar planar transmission line structures, we expect the charge coupling in our Si device to have the same order of magnitude.

7.4 Experimental Characterization

All experiments were performed in an Oxford Instruments Triton cryogen-free dilution refrigerator at temperatures below 15 mK. All low frequency measurement wiring is filtered at

the mixing chamber, first through a lossy Eccosorb CR124 100 MHz low pass filter, which has been demonstrated to attenuate frequencies up to 40GHz [108]. This is followed by a surface mount RC π low pass filter with a 1kHz cutoff.

To test the ability to confine charge, we made a series of DC electronic transport measurements in a device similar to the one in Figs 7.1-7.2a. Figure 7.4(a) shows a plot of current through the device on a log scale as a function of bias voltage on the left and right plunger gates $P_{L,R}$. Ohmic contacts 1 and 4 form the source and drain with bias voltage of 100 μ V in a standard AC lock-in technique at 13Hz using a Stanford Research Systems SR810. Overlaid on top of this is the a honeycomb charge stability diagram expected for transport through a double quantum dot in Coulomb blockade [125, 137] and analysis of this yields plunger gate capacitances of 7-8 aF.

The left QPC is biased by applying a 1 nA current bias to ohmics 1-2, while a bias voltage on Q_L brings this channel close to pinch-off. The QPC conductance measured with the same lock-in technique above is shown in Figure 7.4(b) as a function of left plunger P_L voltage. Red arrows mark peaks due to charging events in the left dot, which are repeatable. Figures 7.4(a)-(b) indicate that our double quantum dot is indeed exhibiting single electron charging.

However, when we try to measure the charge stability from transport through the dots over a wider range of gate bias, we find the current resonances shown in Fig 7.4(c). We cannot get consistent honeycomb patterns over a large bias range. A qualitative explanation for this is given in the Summary, Sec. 7.5.

In Fig 7.4(a), gates $T_{R,L}$, $Q_{R,L}$ were biased at 4 V, while $L_{T,B}$, $R_{T,B}$, and U were at 1 V. In Fig 7.4(c), $T_{R,L}$, $Q_{R,L}$ were at 4 V, $L_{T,B}$, $R_{T,B}$ at 1.2V, and U was at 0.95 V. For Fig 7.4(b), these gates were in a different bias regime. T_L was 4.5 V, and Q_L was 401.5mV below T_L to put the QPC near pinch-off. The side gates $L_{T,B}$, $R_{T,B}$ were at -1.5V to shut off transport from the quantum dot to the 2DEG, and U was also at -1.5V to isolate the two dots. The negative biases on these confinement gates required the larger compensating plunger gate voltages in Fig 7.4(b).

Microwave measurements of the resonator were made in reflection using a vector network analyzer (VNA). The incoming microwaves are thermalized by attenuators with values of 20 dB at 4K, 20dB at the still, and 20 dB at base temperature on the mixing chamber. From there they are sent though a circulator to reflect off the device and on return pass through an additional isolator to a NbTi superconducting coaxial line. This line sends the signal to a Low Noise Factory LNF-LNC4.8A HEMT amplifier at 4K. Fig. 7.5(a) shows measurements of the reflected amplitude at -150 dBm input power, including the overall system gain, and Fig. 7.5(b) shows the phase. The bond pads were connected to a 180° hybrid for differential excitation via 1 cm wire bonds connected to $RF_{1,2}$ in Fig. 7.1. This adds series inductance, modifying the complex impedance away from the Lorentzian approximation for a resonator. Assuming the wire bond impedance is purely reactive, we fit the real part of the reflection, removing the time delay so that the reflection data is measured with respect to resonator. The resulting fit to a Lorentzian is very good, as shown in Fig. 7.5(c) for -150 dBm. From the fit we extract a resonant frequency f_0 of 5.511 GHz, which is down from the 6 GHz set by the

transmission line length due to the reactive loading of the wire bonds and coupling capacitors. The resonator Q of 307 breaks down to an external Q_{ext} of 411 and an internal Q_{int} of 1210, so that the resonator is over-coupled. This Q translates to a half-power bandwidth of 18 MHz, which would allow measurement of fast charge dynamics.

The power dependence of Q_{int} is plotted in Fig. 7.5(d) from -150 dBm to -70 dBm. Using $\bar{n} = 4P_{\text{in}}Q^2/(Q_{\text{ext}}\hbar\omega_0)$, where P_{in} is the steady state input power, this corresponds to an average photon number \bar{n} of order 0.01 to 10^6 . Over this range Q_{int} is observed to climb from 1210 to 1530. To demonstrate that this loss is due to the PECVD SiO_2 dielectric in the shorting capacitor, we have fabricated a device with this capacitor replaced by an Al shorting stub and measure Q_{int} to be above 10,000 at -150 dBm for a Q_{ext} of 2000. This PECVD SiO_2 internal loss and internal loss power dependence is far less than previously reported for LC resonator capacitors [72] or for coplanar waveguide (CPW) transmission line resonators [82]. This may be due to the fact that for our devices the shorting capacitor is at a voltage node where the resonator voltage is minimal, but more comprehensive work is required to demonstrate this.

7.5 Summary

We have designed and developed a fabrication process for a Si double quantum dot coupled to a microwave resonator. We have performed simple numerical simulations to verify dot charge confinement, and estimate the double dot - resonator vacuum coupling strength. We have fabricated test devices and characterized the quantum dot charge confinement through DC transport measurements and the microwave resonator spectrum with a VNA. The resonant frequency is 5.511GHz with $Q_{\text{int}}/Q_{\text{ext}} = 3$ in the overcoupled regime, while the total $Q = 307$ gives a line width of 18 MHz. The over-coupling allows for pulsed time-domain detection of dispersive resonant frequency shifts in the phase of a homodyne measurement. The fastest resolvable phase change is ~ 60 ns, set by the inverse line width, which is well within the charge relaxation T_1 seen in Si charge qubits [123].

The DC transport measurements demonstrate charge confinement for the device, but Fig. 7.4(c) shows that the charge stability honeycombs are not found over a wide enough gate bias range. One explanation for this is that the 2DEG accumulation gates $T_{\text{L,R}}$ become too narrow where they come near the confinement gates $L_{\text{T,B}}$ and $R_{\text{T,B}}$, as shown between the arrows in Fig 7.6(d), so that the 2DEG in fact becomes sub two-dimensional in this region. Then our double quantum dot, with honeycomb current resonances shown schematically in Fig. 7.6(a) is in series with short, sub 2D channels with regions of allowed and forbidden conductance, shown schematically in Fig. 7.6(c), and the resulting total series conductance is shown schematically in Fig. 7.6(c). This is a very qualitative representation of the data in Fig. 7.4(c). A detailed experimental study of sub 2D reservoir behavior is given in Ref. [76] and its analysis the context of other quantum dot transport phenomena is given in [27].

In hindsight, this problem can be identified in the 2DEG density simulation shown in Fig. 7.3(a) by noting that the 2DEG density drops and becomes non-uniform over very

short lengths where $T_{L,R}$ narrow at the gap between the confinement gates $L_{T,B}$ and $R_{T,B}$. However, due to the use of the semi-classical Thomas-Fermi approximation the lowering of dimensionality is not properly captured. The solution to this is to make the narrow part of the gates, shown between the Fig. 7.6(d) arrows, wider to $\sim 300\text{nm}$, or ~ 30 times the Si transverse effective mass Thomas-Fermi screening length [2, 51].

After this, there is more non-trivial testing to be done. One test is to demonstrate that the double dot can be completely depleted of electrons, so that the few-electron regime can be reached, followed by showing that the splitting of the lowest two valleys is large, similar to the $100\text{-}750\mu\text{V}$ measured in previous Si MOS quantum dots [137, 2, 133]. Both of these are necessary for spin manipulation of Si double dot devices. Simultaneously with this is demonstration of dispersive readout of the honeycomb charge stability diagrams with the microwave resonator, as done previously in III-V devices [30, 114, 85]. Attempts will be made to make a simple charge qubit and use the resonator for dispersive readout in pulsed time-domain experiments.

The primary distinguishing feature about our prototype, is that at the time of submission of this manuscript, it is the first resonator coupled double quantum dot using silicon as the semiconductor host material, in a geometry suitable for dispersive, quantum non-demolition cQED measurements [6, 13, 21, 41, 48, 78, 118] and an attempt to reach the resonator-qubit strong coupling regime of cQED [121, 6, 50, 12] . While we do not prescribe a path for adding the magnetic field gradient to achieve EDSR [89] enabled spin-resonator cQED [50] coupling, the single metal layer defining the double quantum dot is an excellent starting point on top of which to fabricate additional magnetic nanostructures.

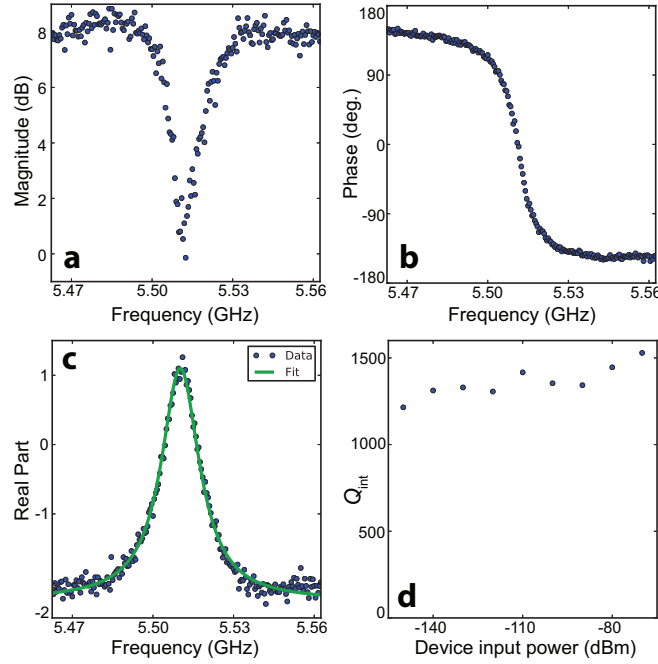


Figure 7.5: (color online) Microwave resonator reflection coefficient data **(a)** Magnitude, including overall gain of the measurement chain. **(b)** Phase **(c)** Real part, with time delay adjusted to adjust reference to input plane of resonator. The fit is to a Lorentzian. **(d)** Power dependence of the internal quality factor, characterizing resonator internal losses.

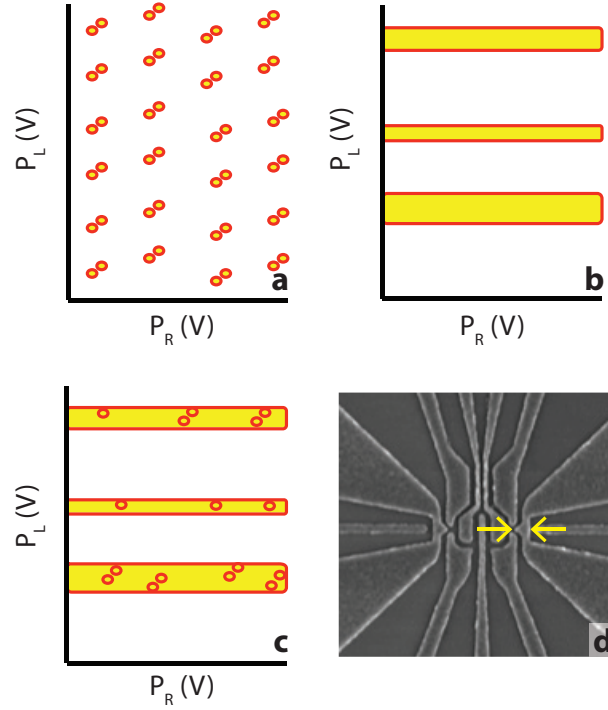


Figure 7.6: (color online) Schematic representation for the failure to achieve consistent long range honey combs with sweeps of plunger gate bias. **(a)** Cartoon of the double quantum dot honeycomb current peaks as a function of gate bias. **(b)** Cartoon of the sub two-dimensional conductance in the region marked by arrows in (d), giving regions of allowed conductance, marked in yellow, surrounded by regions of forbidden conductance. **(c)** Cartoon of what transport measurements of (a) and (b) in series would look like. **(d)** The region of the accumulation gate marked with the yellow arrows is where the 2DEG becomes sub two-dimensional.

Chapter 8

Conclusions

Research in quantum information science has made many breakthroughs as well as exposed many challenges over the past two decades or so. In this thesis, we explored three important topics in this field: open quantum systems, quantum feedback control, and circuit-QED.

The theory of open quantum systems helps us understand and fight against the quantum dissipation channels. We discussed both the Lindblad master equation approach to Markovian systems and the HEoM approach to non-Markovian systems. We used controlled relaxation for a qubit as an example to demonstrate the potential of the HEoM approach for controlling non-Markovian systems. Armed with HEoM, we may also be able to answer many other reachability and controllability questions for open quantum systems. In addition, we illustrated ways to unravel HEoM, which might be a valuable step towards making simulations more efficient. More generally, effectively solving an open quantum system with a non-Gaussian bath is still a very challenging problem.

Motivated by recent advances in realization of real-time feedback control in circuit quantum electrodynamics systems [118], we formulated the theory of PI control which can be more effective than direct feedback control but is still feasible to implement experimentally. We demonstrated its application in two-qubit entanglement generation under ideal conditions and harmonic oscillator state stabilization. Further investigation taking into account experimental imperfections like non-zero temperature and various decoherence channels for the two-qubit entanglement generation problem is desired. In addition to PI control, we also demonstrated ways to come up with and to verify optimal control strategies, which are theoretically illuminating and also important. We studied qubit purification with a Markovian bath as an example, but we also would like to know the optimal control strategies for many other systems and for different types of baths as well.

We reviewed the circuit-QED scheme for a quantum information processor in the last part of this thesis. Circuit-QED with superconducting qubits has been the most fruitful experimentally so far. However, we also see that the scheme with quantum dot electron spins in isotopically purified silicon coupled to resonator photons via an inhomogeneous magnetic field can potentially reach the strong coupling regime and is very promising as well. Adding micro-magnets on top of our silicon quantum dot to create an inhomogeneous

magnetic field needs many more engineering efforts and is worthy of future research. On the theory side, more complete analysis of the spin decoherence rate in the presence of field gradient is desired. Research on circuit-QED based architecture of quantum information processor remains to be of great importance. In particular, combining spin qubits that have long coherence with superconducting qubits that have fast gates in a hybrid quantum circuit seems to be a great solution [62].

Bibliography

- [1] WA Al-Saidi and D Stroud. “Eigenstates of a small Josephson junction coupled to a resonant cavity”. In: *Physical Review B* 65.1 (2001), p. 014512.
- [2] Tsuneya Ando, Alan B Fowler, and Frank Stern. “Electronic properties of two-dimensional systems”. In: *Reviews of Modern Physics* 54.2 (1982), p. 437.
- [3] Giuliano Benenti. *Principles of quantum computation and information*. Vol. 1. World scientific, 2007.
- [4] Giuliano Benenti. *Principles of quantum computation and information*. Vol. 2. World scientific, 2007.
- [5] Charles H Bennett, Gilles Brassard, et al. “Quantum cryptography: Public key distribution and coin tossing”. In: *Proceedings of IEEE International Conference on Computers, Systems and Signal Processing*. Vol. 175. 0. New York. 1984.
- [6] Alexandre Blais et al. “Cavity quantum electrodynamics for superconducting electrical circuits: An architecture for quantum computation”. In: *Phys. Rev. A* 69 (6 2004), p. 062320. DOI: 10.1103/PhysRevA.69.062320. URL: <http://link.aps.org/doi/10.1103/PhysRevA.69.062320>.
- [7] Matthew G Borselli et al. “Pauli spin blockade in undoped Si/SiGe two-electron double quantum dots”. In: *Applied Physics Letters* 99.6 (2011), p. 063109.
- [8] Vincent Bouchiat et al. “Quantum coherence with a single Cooper pair”. In: *Physica Scripta* 1998.T76 (1998), p. 165.
- [9] Heinz-Peter Breuer and Francesco Petruccione. *The theory of open quantum systems*. Oxford university press, 2002.
- [10] Todd A Brun. “A simple model of quantum trajectories”. In: *American Journal of Physics* 70.7 (2002), pp. 719–737.
- [11] H. F. Chau. “Practical scheme to share a secret key through a quantum channel with a 27.6% bit error rate”. In: *Phys. Rev. A* 66 (6 2002), p. 060302. DOI: 10.1103/PhysRevA.66.060302. URL: <http://link.aps.org/doi/10.1103/PhysRevA.66.060302>.
- [12] L Childress, AS Sørensen, and MD Lukin. “Mesoscopic cavity quantum electrodynamics with quantum dots”. In: *Physical Review A* 69.4 (2004), p. 042302.

- [13] AA Clerk et al. “Introduction to quantum noise, measurement, and amplification”. In: *Reviews of Modern Physics* 82.2 (2010), p. 1155.
- [14] J. Combes and H. M. Wiseman. “Quantum feedback for rapid state preparation in the presence of control imperfections”. In: *J. Phys. B: At. Mol. Opt. Phys.* 44 (2011), p. 154008.
- [15] Joshua Combes and Kurt Jacobs. “Rapid State Reduction of Quantum Systems Using Feedback Control”. In: *Phys. Rev. Lett.* 96.1 (Jan. 2006), p. 010504.
- [16] Joshua Combes et al. “Rapid purification of quantum systems by measuring in a feedback-controlled unbiased basis”. In: *Phys. Rev. A* 82.2 (Aug. 2010), p. 022307.
- [17] James W Cooley and John W Tukey. “An algorithm for the machine calculation of complex Fourier series”. In: *Mathematics of computation* 19.90 (1965), pp. 297–301.
- [18] Don Coppersmith. “Modifications to the number field sieve”. In: *Journal of Cryptology* 6.3 (1993), pp. 169–180.
- [19] I. Csiszar and J. Korner. “Broadcast channels with confidential messages”. In: *Information Theory, IEEE Transactions on* 24.3 (1978), pp. 339–348. ISSN: 0018-9448. DOI: 10.1109/TIT.1978.1055892.
- [20] MH Devoret and RJ Schoelkopf. “Superconducting circuits for quantum information: an outlook”. In: *Science* 339.6124 (2013), pp. 1169–1174.
- [21] L DiCarlo et al. “Preparation and measurement of three-qubit entanglement in a superconducting circuit”. In: *Nature* 467.7315 (2010), pp. 574–578.
- [22] Lajos Diósi, Nicolas Gisin, and Walter T. Strunz. “Quantum approach to coupling classical and quantum dynamics”. In: *Phys. Rev. A* 61 (2 2000), p. 022108. DOI: 10.1103/PhysRevA.61.022108. URL: <http://link.aps.org/doi/10.1103/PhysRevA.61.022108>.
- [23] David P DiVincenzo. “Topics in quantum computers”. In: *Mesoscopic electron transport*. Springer, 1997, pp. 657–677.
- [24] A. C. Doherty and K. Jacobs. “Feedback control of quantum systems using continuous state estimation”. In: *Phys. Rev. A* 60 (4 1999), pp. 2700–2711. DOI: 10.1103/PhysRevA.60.2700. URL: <http://link.aps.org/doi/10.1103/PhysRevA.60.2700>.
- [25] Andrew C Doherty et al. “The quantum trajectory approach to quantum feedback control of an oscillator revisited”. In: *Philosophical Transactions of the Royal Society A: Mathematical, Physical and Engineering Sciences* 370.1979 (2012), pp. 5338–5353.
- [26] Artur K. Ekert. “Quantum cryptography based on Bell’s theorem”. In: *Phys. Rev. Lett.* 67 (6 1991), pp. 661–663. DOI: 10.1103/PhysRevLett.67.661. URL: <http://link.aps.org/doi/10.1103/PhysRevLett.67.661>.
- [27] CC Escott, FA Zwanenburg, and A Morello. “Resonant tunnelling features in quantum dots”. In: *Nanotechnology* 21.27 (2010), p. 274018.

- [28] Richard P Feynman. “Simulating physics with computers”. In: *International journal of theoretical physics* 21.6 (1982), pp. 467–488.
- [29] Richard Phillips Feynman and FL Vernon Jr. “The theory of a general quantum system interacting with a linear dissipative system”. In: *Annals of physics* 24 (1963), pp. 118–173.
- [30] T. Frey et al. “Dipole Coupling of a Double Quantum Dot to a Microwave Resonator”. In: *Phys. Rev. Lett.* 108 (4 2012), p. 046807. DOI: 10.1103/PhysRevLett.108.046807. URL: <http://link.aps.org/doi/10.1103/PhysRevLett.108.046807>.
- [31] T Frey et al. “Quantum dot admittance probed at microwave frequencies with an on-chip resonator”. In: *Physical Review B* 86.11 (2012), p. 115303.
- [32] Jonathan R Friedman et al. “Quantum superposition of distinct macroscopic states”. In: *nature* 406.6791 (2000), pp. 43–46.
- [33] Gian Carlo Ghirardi, Philip Pearle, and Alberto Rimini. “Markov processes in Hilbert space and continuous spontaneous localization of systems of identical particles”. In: *Phys. Rev. A* 42 (1 1990), pp. 78–89. DOI: 10.1103/PhysRevA.42.78. URL: <http://link.aps.org/doi/10.1103/PhysRevA.42.78>.
- [34] Vitaly L Ginzburg. “Nobel Lecture: On superconductivity and superfluidity (what I have and have not managed to do) as well as on the physical minimum at the beginning of the XXI century”. In: *Reviews of modern physics* 76.3 (2004), p. 981.
- [35] Vittorio Giovannetti, Seth Lloyd, and Lorenzo Maccone. “Quantum Random Access Memory”. In: *Phys. Rev. Lett.* 100 (16 2008), p. 160501. DOI: 10.1103/PhysRevLett.100.160501. URL: <http://link.aps.org/doi/10.1103/PhysRevLett.100.160501>.
- [36] Nicolas Gisin et al. “Quantum cryptography”. In: *Rev. Mod. Phys.* 74 (1 2002), pp. 145–195. DOI: 10.1103/RevModPhys.74.145. URL: <http://link.aps.org/doi/10.1103/RevModPhys.74.145>.
- [37] H.-S. Goan et al. “Continuous quantum measurement of two coupled quantum dots using a point contact: A quantum trajectory approach”. In: *Phys. Rev. B* 63.12 (2001), p. 125326.
- [38] D. Gottesman and Hoi-Kwong Lo. “Proof of security of quantum key distribution with two-way classical communications”. In: *Information Theory, IEEE Transactions on* 49.2 (2003), pp. 457–475. ISSN: 0018-9448. DOI: 10.1109/TIT.2002.807289.
- [39] E Griffith et al. “Rapid-state purification protocols for a Cooper pair box”. In: *Phys. Rev. B* 75.1 (Jan. 2007), p. 014511.
- [40] R Hanson et al. “Spins in few-electron quantum dots”. In: *Reviews of Modern Physics* 79.4 (2007), p. 1217.
- [41] M Hatridge et al. “Quantum back-action of an individual variable-strength measurement”. In: *Science* 339.6116 (2013), pp. 178–181.

- [42] Toshiki Hayashi et al. “Coherent manipulation of electronic states in a double quantum dot”. In: *Physical review letters* 91.22 (2003), p. 226804.
- [43] Scott Hill and William K. Wootters. “Entanglement of a Pair of Quantum Bits”. In: *Phys. Rev. Lett.* 78 (26 1997), pp. 5022–5025. DOI: 10.1103/PhysRevLett.78.5022. URL: <http://link.aps.org/doi/10.1103/PhysRevLett.78.5022>.
- [44] Philip A Hiskett et al. “Long-distance quantum key distribution in optical fibre”. In: *New Journal of Physics* 8.9 (2006), p. 193.
- [45] C J Hood et al. “The atom-cavity microscope: Single atoms bound in orbit by single photons”. In: *Science* 287 (2000), p. 1447.
- [46] C. J. Hood et al. “The Atom-Cavity Microscope: Single Atoms Bound in Orbit by Single Photons”. In: *Science* 287.5457 (2000), pp. 1447–1453. DOI: 10.1126/science.287.5457.1447. eprint: <http://www.sciencemag.org/content/287/5457/1447.full.pdf>. URL: <http://www.sciencemag.org/content/287/5457/1447.abstract>.
- [47] Asa Hopkins et al. “Feedback cooling of a nanomechanical resonator”. In: *Phys. Rev. B* 68 (23 2003), p. 235328. DOI: 10.1103/PhysRevB.68.235328. URL: <http://link.aps.org/doi/10.1103/PhysRevB.68.235328>.
- [48] AA Houck et al. “Generating single microwave photons in a circuit”. In: *Nature* 449.7160 (2007), pp. 328–331.
- [49] MG House et al. “Non-equilibrium charge stability diagrams of a silicon double quantum dot”. In: *Applied Physics Letters* 99.11 (2011), p. 112116.
- [50] Xuedong Hu, Yu-xi Liu, and Franco Nori. “Strong coupling of a spin qubit to a superconducting stripline cavity”. In: *Physical Review B* 86.3 (2012), p. 035314.
- [51] Thomas Ihn. *Semiconductor nanostructures*. Oxford University Press New York, 2010.
- [52] Akihito Ishizaki and Graham R Fleming. “Unified treatment of quantum coherent and incoherent hopping dynamics in electronic energy transfer: Reduced hierarchy equation approach”. In: *The Journal of chemical physics* 130.23 (2009), p. 234111.
- [53] K. Jacobs and P. L. Knight. “Linear quantum trajectories: Applications to continuous projection measurements”. In: *Phys. Rev. A* 57 (4 1998), pp. 2301–2310. DOI: 10.1103/PhysRevA.57.2301. URL: <http://link.aps.org/doi/10.1103/PhysRevA.57.2301>.
- [54] K. Jacobs and A. Shabani. “Quantum feedback control: how to use verification theorems and viscosity solutions to find optimal protocols”. In: *Contemp. Phys* 49 (2008), p. 435.
- [55] K. Jacobs and D. A. Steck. “A straightforward introduction to continuous quantum measurement”. In: *Contemp. Phys* 47 (2006), p. 279.
- [56] Kurt Jacobs. “How to project qubits faster using quantum feedback”. In: *Phys. Rev. A* 67.3 (Mar. 2003), 030301(R).

- [57] Kurt Jacobs. “Optimal feedback control for the rapid preparation of a single qubit”. In: *Proc. SPIE Fluct. Noise Photonics and Quant. Optics III* 5468 (2004), p. 355.
- [58] Kurt Jacobs and Daniel A Steck. “A straightforward introduction to continuous quantum measurement”. In: *Contemporary Physics* 47.5 (2006), pp. 279–303.
- [59] P. E. Kloeden and E. Platen. *Numerical solution of stochastic differential equations*. Springer, 1992.
- [60] PL Knight. *Fundamental Systems in Quantum Optics*. Taylor & Francis, 1993.
- [61] Jens Koch et al. “Charge-insensitive qubit design derived from the Cooper pair box”. In: *Phys. Rev. A* 76 (4 2007), p. 042319. DOI: 10.1103/PhysRevA.76.042319. URL: <http://link.aps.org/doi/10.1103/PhysRevA.76.042319>.
- [62] Y. Kubo et al. “Hybrid Quantum Circuit with a Superconducting Qubit Coupled to a Spin Ensemble”. In: *Phys. Rev. Lett.* 107 (22 2011), p. 220501. DOI: 10.1103/PhysRevLett.107.220501. URL: <http://link.aps.org/doi/10.1103/PhysRevLett.107.220501>.
- [63] NS Lai et al. “Pauli spin blockade in a highly tunable silicon double quantum dot”. In: *Scientific reports* 1 (2011).
- [64] Hanhan Li et al. “Optimality of qubit purification protocols in the presence of imperfections”. In: *Phys. Rev. A* 87 (3 2013), p. 032334. DOI: 10.1103/PhysRevA.87.032334. URL: <http://link.aps.org/doi/10.1103/PhysRevA.87.032334>.
- [65] CC Lo et al. “All-electrical nuclear spin polarization of donors in silicon”. In: *Physical review letters* 110.5 (2013), p. 057601.
- [66] Hoi-Kwong Lo and H. F. Chau. “Unconditional Security of Quantum Key Distribution over Arbitrarily Long Distances”. In: *Science* 283.5410 (1999), pp. 2050–2056. DOI: 10.1126/science.283.5410.2050. eprint: <http://www.sciencemag.org/content/283/5410/2050.full.pdf>. URL: <http://www.sciencemag.org/content/283/5410/2050.abstract>.
- [67] Daniel Loss and David P DiVincenzo. “Quantum computation with quantum dots”. In: *Physical Review A* 57.1 (1998), p. 120.
- [68] Jian Ma et al. “Entanglement dynamics of two qubits in a common bath”. In: *Physical Review A* 85.6 (2012), p. 062323.
- [69] Yuriy Makhlin, Gerd Schön, and Alexander Shnirman. “Quantum-state engineering with Josephson-junction devices”. In: *Reviews of modern physics* 73.2 (2001), p. 357.
- [70] Yuri Manin. “Computable and Uncomputable (in Russian)”. In: *Sovetskoye Radio* (1980).
- [71] Florian Marquardt and C Bruder. “Superposition of two mesoscopically distinct quantum states: Coupling a Cooper-pair box to a large superconducting island”. In: *Physical Review B* 63.5 (2001), p. 054514.

- [72] John M Martinis et al. “Decoherence in Josephson qubits from dielectric loss”. In: *Physical review letters* 95.21 (2005), p. 210503.
- [73] BM Maune et al. “Coherent singlet-triplet oscillations in a silicon-based double quantum dot”. In: *Nature* 481.7381 (2012), pp. 344–347.
- [74] Alfred J Menezes, Paul C Van Oorschot, and Scott A Vanstone. *Handbook of applied cryptography*. CRC press, 2010.
- [75] Andrea Morello et al. “Single-shot readout of an electron spin in silicon”. In: *Nature* 467.7316 (2010), pp. 687–691.
- [76] M Möttönen et al. “Probe and control of the reservoir density of states in single-electron devices”. In: *Physical Review B* 81.16 (2010), p. 161304.
- [77] COMSOL Multiphysics. “version 4.2”. In: *Heat Transfer Module* (2011).
- [78] K. W. Murch et al. “Cavity-Assisted Quantum Bath Engineering”. In: *Phys. Rev. Lett.* 109 (18 2012), p. 183602. DOI: 10.1103/PhysRevLett.109.183602. URL: <http://link.aps.org/doi/10.1103/PhysRevLett.109.183602>.
- [79] Yu Nakamura, Yu A Pashkin, and JS Tsai. “Coherent control of macroscopic quantum states in a single-Cooper-pair box”. In: *Nature* 398.6730 (1999), pp. 786–788.
- [80] Michael A Nielsen and Isaac L Chuang. *Quantum computation and quantum information*. Cambridge university press, 2010.
- [81] KC Nowack et al. “Coherent control of a single electron spin with electric fields”. In: *Science* 318.5855 (2007), pp. 1430–1433.
- [82] Aaron D O’Connell et al. “Microwave dielectric loss at single photon energies and millikelvin temperatures”. In: *Applied Physics Letters* 92.11 (2008), p. 112903.
- [83] Ognian Oreshkov and Todd A. Brun. “Weak Measurements Are Universal”. In: *Phys. Rev. Lett.* 95 (11 2005), p. 110409. DOI: 10.1103/PhysRevLett.95.110409. URL: <http://link.aps.org/doi/10.1103/PhysRevLett.95.110409>.
- [84] A Peres. *Quantum theory: Concepts and methods, 1993*. Kluwer, Dordrecht.
- [85] KD Petersson et al. “Circuit quantum electrodynamics with a spin qubit”. In: *Nature* 490.7420 (2012), pp. 380–383.
- [86] J. R. Petta et al. “Manipulation of a Single Charge in a Double Quantum Dot”. In: *Phys. Rev. Lett.* 93 (18 2004), p. 186802. DOI: 10.1103/PhysRevLett.93.186802. URL: <http://link.aps.org/doi/10.1103/PhysRevLett.93.186802>.
- [87] JR Petta et al. “Coherent manipulation of coupled electron spins in semiconductor quantum dots”. In: *Science* 309.5744 (2005), pp. 2180–2184.
- [88] M Pioro-Ladriere et al. “Micromagnets for coherent control of spin-charge qubit in lateral quantum dots”. In: *Applied physics letters* 90.2 (2007), p. 024105.
- [89] Michel Pioro-Ladrière et al. “Selective manipulation of electron spins with electric fields”. In: *Progress of Theoretical Physics Supplement* 176 (2008), pp. 322–340.

- [90] David M Pozar. *Microwave engineering*. John Wiley & Sons, 2009.
- [91] J. M. Raimond, M. Brune, and S. Haroche. “Manipulating quantum entanglement with atoms and photons in a cavity”. In: *Rev. Mod. Phys.* 73 (3 2001), pp. 565–582. DOI: 10.1103/RevModPhys.73.565. URL: <http://link.aps.org/doi/10.1103/RevModPhys.73.565>.
- [92] Jørgen Rammer. *Quantum field theory of non-equilibrium states*. Cambridge University Press, 2007.
- [93] Emmanuel I. Rashba. “Theory of electric dipole spin resonance in quantum dots: Mean field theory with Gaussian fluctuations and beyond”. In: *Phys. Rev. B* 78 (19 2008), p. 195302. DOI: 10.1103/PhysRevB.78.195302. URL: <http://link.aps.org/doi/10.1103/PhysRevB.78.195302>.
- [94] DJ Reilly et al. “Fast single-charge sensing with a rf quantum point contact”. In: *Applied Physics Letters* 91.16 (2007), p. 162101.
- [95] Chad Rigetti et al. “Superconducting qubit in a waveguide cavity with a coherence time approaching 0.1 ms”. In: *Physical Review B* 86.10 (2012), p. 100506.
- [96] Jun John Sakurai and San Fu Tuan. *Modern quantum mechanics*. Vol. 1. Addison-Wesley Reading, Massachusetts, 1985.
- [97] Gian Salis et al. “Electrical control of spin coherence in semiconductor nanostructures”. In: *Nature* 414.6864 (2001), pp. 619–622.
- [98] Mohan Sarovar et al. “High-fidelity measurement and quantum feedback control in circuit QED”. In: *Physical Review A* 72.6 (2005), p. 062327.
- [99] A. R. Schmidt et al. “A prototype silicon double quantum dot with dispersive microwave readout”. In: *Journal of Applied Physics* 116.4, 044503 (2014), pp. –. DOI: <http://dx.doi.org/10.1063/1.4890835>. URL: <http://scitation.aip.org/content/aip/journal/jap/116/4/10.1063/1.4890835>.
- [100] RJ Schoelkopf and SM Girvin. “Wiring up quantum systems”. In: *Nature* 451.7179 (2008), pp. 664–669.
- [101] MD Schroer et al. “Radio Frequency Charge Parity Meter”. In: *Physical review letters* 109.16 (2012), p. 166804.
- [102] David Isaac Schuster. *Circuit quantum electrodynamics*. 2007.
- [103] AP Sears et al. “Photon shot noise dephasing in the strong-dispersive limit of circuit QED”. In: *Physical Review B* 86.18 (2012), p. 180504.
- [104] A. Shabani and K. Jacobs. “Locally Optimal Control of Quantum Systems with Strong Feedback”. In: *Phys. Rev. Lett.* 101 (2008), p. 230403.
- [105] Zhan Shi et al. “Coherent quantum oscillations and echo measurements of a Si charge qubit”. In: *Physical Review B* 88.7 (2013), p. 075416.

- [106] P. Shor. “Polynomial-Time Algorithms for Prime Factorization and Discrete Logarithms on a Quantum Computer”. In: *SIAM Review* 41.2 (1999), pp. 303–332. DOI: 10.1137/S0036144598347011. eprint: <http://dx.doi.org/10.1137/S0036144598347011>. URL: <http://dx.doi.org/10.1137/S0036144598347011>.
- [107] Peter W. Shor and John Preskill. “Simple Proof of Security of the BB84 Quantum Key Distribution Protocol”. In: *Phys. Rev. Lett.* 85 (2 2000), pp. 441–444. DOI: 10.1103/PhysRevLett.85.441. URL: <http://link.aps.org/doi/10.1103/PhysRevLett.85.441>.
- [108] DH Slichter, Ofer Naaman, and Irfan Siddiqi. “Millikelvin thermal and electrical performance of lossy transmission line filters”. In: *Applied Physics Letters* 94.19 (2009), p. 192508.
- [109] Karl J ström and Tore Hägglund. “PID controllers: theory, design, and tuning”. In: *Instrument Society of America, Research Triangle Park, NC* (1995).
- [110] Johan Strümpfer and Klaus Schulten. “Light harvesting complex II B850 excitation dynamics”. In: *The Journal of chemical physics* 131.22 (2009), p. 225101.
- [111] Simon M Sze and Kwok K Ng. *Physics of semiconductor devices*. John Wiley & Sons, 2006.
- [112] Yoshitaka Tanimura and Ryogo Kubo. “Two-Time Correlation Functions of a System Coupled to a Heat Bath with a Gaussian-Markoffian Interaction”. In: *Journal of the Physical Society of Japan* 58.4 (1989), pp. 1199–1206. DOI: 10.1143/JPSJ.58.1199. eprint: <http://dx.doi.org/10.1143/JPSJ.58.1199>. URL: <http://dx.doi.org/10.1143/JPSJ.58.1199>.
- [113] Caroline H Thompson. “Homodyne detection and optical parametric amplification: a classical approach applied to proposed” loophole-free” Bell tests”. In: *arXiv preprint quant-ph/0512141* (2005).
- [114] H Toida, T Nakajima, and S Komiyama. “Vacuum Rabi splitting in a semiconductor circuit QED system”. In: *Physical review letters* 110.6 (2013), p. 066802.
- [115] LA Tracy et al. “Double quantum dot with tunable coupling in an enhancement-mode silicon metal-oxide semiconductor device with lateral geometry”. In: *Applied Physics Letters* 97.19 (2010), p. 192110.
- [116] Alexei M Tyryshkin et al. “Electron spin coherence exceeding seconds in high-purity silicon”. In: *Nature materials* 11.2 (2012), pp. 143–147.
- [117] Alexei M Tyryshkin et al. “Electron spin coherence exceeding seconds in high-purity silicon”. In: *Nature materials* 11.2 (2012), pp. 143–147.
- [118] R Vijay et al. “Stabilizing Rabi oscillations in a superconducting qubit using quantum feedback”. In: *Nature* 490.7418 (2012), pp. 77–80.
- [119] Caspar H Van der Wal et al. “Quantum superposition of macroscopic persistent-current states”. In: *Science* 290.5492 (2000), pp. 773–777.

- [120] A. Wallraff et al. “Comment on “Vacuum Rabi Splitting in a Semiconductor Circuit QED System””. In: *Phys. Rev. Lett.* 111 (24 2013), p. 249701. DOI: 10.1103/PhysRevLett.111.249701. URL: <http://link.aps.org/doi/10.1103/PhysRevLett.111.249701>.
- [121] Andreas Wallraff et al. “Strong coupling of a single photon to a superconducting qubit using circuit quantum electrodynamics”. In: *Nature* 431.7005 (2004), pp. 162–167.
- [122] Daniel F Walls and Gerard J Milburn. *Quantum optics*. Springer, 2007.
- [123] K Wang et al. “Charge relaxation in a single-electron Si/SiGe double quantum dot”. In: *Physical review letters* 111.4 (2013), p. 046801.
- [124] Ulrich Weiss. *Quantum dissipative systems*. Vol. 10. World Scientific, 1999.
- [125] Wilfred G van der Wiel et al. “Electron transport through double quantum dots”. In: *Reviews of Modern Physics* 75.1 (2002), p. 1.
- [126] H. M. Wiseman and G. J. Milburn. *Quantum measurement and control*. Cambridge University Press, 2009.
- [127] H. M. Wiseman and G. J. Milburn. “Quantum theory of optical feedback via homodyne detection”. In: *Phys. Rev. Lett.* 70 (5 1993), pp. 548–551. DOI: 10.1103/PhysRevLett.70.548. URL: <http://link.aps.org/doi/10.1103/PhysRevLett.70.548>.
- [128] H. M. Wiseman and J. F. Ralph. “Reconsidering rapid qubit purification by feedback”. In: *New J. Phys.* 8 (2006), p. 90.
- [129] Howard M Wiseman and Luc Bouten. “Optimality of Feedback Control Strategies for Qubit Purification”. In: *Quantum Information Processing* 7.2-3 (Apr. 2008), pp. 71–83.
- [130] Howard M Wiseman and Gerard J Milburn. *Quantum measurement and control*. Cambridge University Press, 2010.
- [131] William K. Wootters. “Entanglement of Formation of an Arbitrary State of Two Qubits”. In: *Phys. Rev. Lett.* 80 (10 1998), pp. 2245–2248. DOI: 10.1103/PhysRevLett.80.2245. URL: <http://link.aps.org/doi/10.1103/PhysRevLett.80.2245>.
- [132] M Xiao, MG House, and HW Jiang. “Measurement of the spin relaxation time of single electrons in a silicon metal-oxide-semiconductor-based quantum dot”. In: *Physical review letters* 104.9 (2010), p. 096801.
- [133] M Xiao, MG House, and HW Jiang. “Parallel spin filling and energy spectroscopy in few-electron Si metal-on-semiconductor-based quantum dots”. In: *Applied Physics Letters* 97.3 (2010), p. 032103.
- [134] Masahiro Yanagisawa. “Quantum smoothing”. In: *arXiv preprint arXiv:0711.3885* (2007).
- [135] Peter Y Yu and Manuel Cardona. *Fundamentals of semiconductors*. Springer, 1996.

- [136] Alexandre Zagoskin and Alexandre Blais. “Superconducting qubits”. In: *arXiv preprint arXiv:0805.0164* (2008).
- [137] Floris A Zwanenburg et al. “Silicon quantum electronics”. In: *Reviews of Modern Physics* 85.3 (2013), p. 961.